New Cardiovascular Applications of the Turbo Spin

Echo Sequence in Magnetic Resonance Imaging

A Dissertation

Presented to

The Faculty of the School of Engineering and Applied Science

University of Virginia

In Partial Fulfillment

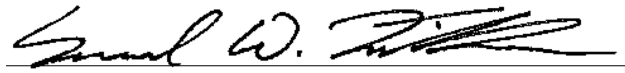Of the Requirements for the Degree of

Doctor of Philosophy in Biomedical Engineering

Samuel W. Fielden

May 2013

APPROVAL SHEET

The dissertation

is submitted in partial fulfillment of the requirements

for the degree of

Doctor of Philosophy

AUTHOR

The dissertation has been read and approved by the examining committee:

Craig Meyer
Dissertation Advisor

John Hossack

Christopher Kramer

John Mugler, III

Scott Acton

Accepted for the School of Engineering and Applied Science:

Dean of School of Engineering and Applied Science

May 2013

Abstract

The advent of fast sequences based on the Rapid Acquisition with Relaxation Enhancement (RARE) sequence allowed T_2-weighted imaging to be performed in clinically feasible scan times and these sequences have become the workhorse for spin-echo imaging in Magnetic Resonance Imaging (MRI). In this work, we propose several variants and applications of the 3D Turbo Spin Echo (TSE) sequence designed to efficiently image endogenous and exogenous long-T_2 species in the body.

There has been renewed interest in developing and utilizing non-contrast MRA methods because of the risk of nephrogenic systemic fibrosis (NSF) in patients with kidney dysfunction. TSE sequences are capable of generating excellent contrast between blood and surrounding tissue based on T_2 differences, but conventional TSE sequences are susceptible to flow-related artifacts and signal loss.

Here, a new, hybrid pulse sequence that shares characteristics with the TSE and balanced Steady State Free Precession (bSSFP) sequence is introduced. Desirable T_2 contrast is provided by the TSE-like pulse sequence design and the improved flow-performance characteristics of bSSFP imaging are gained through fully-refocused gradients and refocusing

pulse phase alternation of RF pulses. The principles of flow-independent angiography in the context of this new TSE sequence, including a description of tissue contrast properties, are described. Additionally, a method for fat/water separation based on phase detection is presented for this application which relies on catalyzation of the TSE echo train. This sequence is capable of performing non-contrast enhanced angiography of the peripheral arterial tree by exploiting the T_2 differences between blood and surrounding tissue.

In order to take advantage of some of the unique properties afforded by non-Cartesian imaging, a 3D TSE sequence which utilizes spiral readouts was developed. For peripheral angiography, spoiler gradients placed in the through-plane direction remove spurious fat signal, and longer echo spacings are available due to spiral sampling, leading to improved venous suppression. To most efficiently acquire the data, partial k-space coverage along with variable density spirals are used to undersample k-space in a controlled and well-understood manner. Additional techniques to prevent spiral artifacts (blurring) from concomitant and B_0 fields as well as corrections to spiral trajectories are applied.

The major focus of MRI research has been on improving resolution, contrast, and shortening acquisition times of standard anatomical images; however, patient outcomes may also be improved by acquiring secondary, functional information about the patient. Yet functionalizing MRI is still in early stages, and much work needs to be done before it is ready to enter the clinic in an impactful way. In a departure from angiography, the TSE sequence is used as an efficient method to generate and utilize signal from fluorine, a secondary nucleus which is of interest for cellular and molecular imaging. Here, the TSE sequence will be used to efficiently sample the persistent signal arising from the relatively long T_2 of fluorine. An SNR efficiency comparison between common ^{19}F MRI sequences is presented along with an ap-

plication of model-based iterative reconstruction techniques designed to improve the quality of low-SNR ^{19}F images by incorporating boundary information derived from accompanying proton images.

The contributions described in this work extend the utility of TSE-type sequences in non-traditional imaging situations by exploiting some of the unique capabilities and attributes of the sequence. Furthermore, the applications described here are directly applicable to unmet clinical and pre-clinical needs.

Acknowledgments

I think science is too commonly viewed as a solitary activity, even by those of us who know better. In this light, I have some people to thank for helping me get to where I am today:

Of course, I first have to thank Dr. Craig Meyer, my advisor. Someone once told me that your relationship with your advisor in grad school progresses through the same stages as your relationship with your parents: First, you're a child and everything your advisor says is the absolute truth. Next, you're a teenager and your advisor is *just* so out of touch and doesn't know anything. If only he could remember what it's like to be a grad student! Finally, you realize your advisor is just a person like everyone else, and only then can you build a real, working relationship with them. Well, I don't know about that second stage, but Craig's depth of knowledge, experience, and enthusiasm have always been an inspiration to me, and as I've progressed through my time at UVA, I've come to find his insights regarding everything from research direction, to career development, to personal life to have been invaluable in their wisdom and wit.

Next, I'd like to thank Dr. John Oshinski, who introduced me to the MRI community when I was an undergrad by having me manually segment what seemed like a billion left

atria from some old data he had laying around. It's a wonder I stuck with it after that, but I'm glad I did.

I forget who it was that modified John von Neumann's quote about mathematics for an MRI audience: "In MRI you don't understand things. You just get used to them." I'd like to thank Drs. Fred Epstein, Wilson Miller, and especially John Mugler for truly understanding the principles of MRI and helping me to understand them, too ... or at least to get used to them. In particular, Dr. Mugler's vast experience with the TSE sequence has certainly been an excellent resource for me as I've wrestled with it over the years.

I'd like to thank Drs. Chris Kramer, Patrick Norton, and Klaus Hagspiel for their help in guiding the clinical portions of this work. Part of what drew me to MR research was its immediate translatability to the clinic, and it's impossible to achieve this without the help and support of MDs in the hospital.

I must thank Drs. John Hossack and Scott Acton for their service on my committee and their valuable insights over the years. I would also like to thank Dr. Sasha Klibanov for his patience in teaching an MR guy how to work in a biochemical synthesis laboratory to make fluorinated nanoparticles. Many thanks go to Dr. Fred Epstein and Dr. Brent French for their truly indispensable advice and help (both with time and resources) regarding the use of mouse models in cardiovascular MR research. I'd like to thank Dr. Yaquin Xu for doing the myocardial infarct surgeries described in Chapter 5, and Dr. Zhongmin Du for his help with the histology also described in that chapter.

I must thank the previous bolus of Craig's students, Drs. Chris Sica, Weitian Chen, and Hao Tan, for all of their patience and help getting me up and running with code and in programming and using the scanners here. Of course I have to thank my labmates: Dr. Xue

Feng, Meihan Wang, Li Zhao, and Dr. Ken Johnson. We've learned a lot from each other over the years; I can't count the number to times one of us turned to another and said, "Hey, can you explain something to me," or "Do you want to work through this with me?"

Christy, my incredible wife (and likely the only one reading this section), I can't imagine having done this without you. Your never-ending love, support, and understanding have kept me level throughout our time in Virginia. Thank you for being you. Finally, I have to thank all of my family who have supported me from afar and pushed me along with the six words every grad student least wants to hear, "When are you going to graduate?" Sorry I'm not "real" doctor, Mom. Special thanks go to my dad for making me work in his welding shop that awful summer when I was 15 and for telling me to find a career indoors. This dissertation is dedicated to him.

Contents

List of Figures

Chapter 1

Introduction

The overarching theme of this dissertation is the development and application of new Magnetic Resonance Imaging (MRI) techniques to the diagnosis and study of cardiovascular disease. Chapters 2 and 3 specifically address the development of new techniques for the diagnosis of clinically relevant (i.e. late-stage) atherosclerosis in the peripheral vasculature. Chapter 4 presents a more thorough technical description of one of the techniques used in Chapter 3. Chapter 5 focuses on developing new methods for imaging inflammation and early-stage atherosclerosis in mouse models and is therefore relevant for pre-clinical exploration of disease progression.

1.1 Atherosclerosis

Atherosclerosis is a wide-spread, progressive disease of the vasculature. Initial lesions form early in life and generally remain asymptomatic as they grow in size throughout adulthood. Once the lesion has reached a size such that it significantly impedes blood flow in the vessel in which it is located, symptoms arise and, depending on which vessel is stenotic, range from

discomfort to death [1, 2]. Furthermore, some lesions are "unstable", meaning the thin, fibrous cap which contains the lipid-rich atherosclerotic core is at risk of rupture. When these so-called vulnerable plaques rupture, thrombi form in the blood vessel and may travel elsewhere in the body to occlude downstream vessels, the result of which may be heart attack or stroke.

Atherosclerosis is now known to be a chronic inflammatory disease, incorporating a wide range of immune cells in a complex chemical micro-environment [3, 4]. Briefly, the disease is believed to begin with oxidized low-density lipoprotein (oxLDL) molecules somehow becoming entrapped in the vessel wall, either through direct recruitment via the LOX-1 receptor, or via oxidation of LDL molecules within the vessel wall itself. There, oxLDL initiates an immune response, recruiting macrophages and other immune cells to the site. These immune cells phagocytose the offending oxLDL, forming foam cells. However, the oxLDL is not degraded by these foam cells, and is released to the extracellular environment in greater concentration when the cells die. This, in turn, triggers further recruitment of immune cells and the cycle continues, eventually forming an atherosclerotic plaque which may grow in size until it causes a narrowing of the vessel lumen.

1.2   Magnetic Resonance Imaging

As a noninvasive imaging modality, MRI has experienced rapid growth over the past several decades due to some of its advantages over other major medical imaging modalities such as computed tomography (CT) and ultrasound. These advantages include no ionizing radiation, excellent soft-tissue contrast, and flexibility in controlling image content by selecting imaging

parameters for different applications. Some of MRI's disadvantages are its comparative slowness, low sensitivity, and cost [5].

1.3   Magnetic Resonance Angiography (MRA)

Peripheral arterial disease (PAD) is defined as atherosclerosis in the arteries of the pelvis and legs and is associated with symptoms ranging from cramping and pain during exercise to rest pain and tissue loss. PAD affects approximately 8 million Americans [6] and if left untreated, can lead to gangrene and amputation. For diagnosis of luminal obstruction, digital subtraction angiography (DSA) is the current gold standard for peripheral vascular imaging, with duplex ultrasonography possibly used focally to assess stenoses or track stents over time [7]. Computed tomography angiographies (CTAs) and MRAs can quickly provide global assessment of the peripheral vasculature and may provide extra-luminal information. Thus, they offer a potential alternative first-line of investigation for PAD. The advantages of MRAs are that they do not expose the patient to ionizing radiation, are noninvasive, and thus have been considered safe. Contrast-enhanced MRA is currently the preferred MRA technique in this setting [8, 9]; however, the established link between gadolinium-based contrast agents and nephrogenic systemic fibrosis (NSF) [10, 11] in patients with Stage IV/V chronic kidney disease has led to tighter contrast dose limits and a great interest in developing MR methods by which accurate, high-resolution images of the arteries may be obtained without the use of contrast agents.

1.4 Non-contrast-enhanced MRA

Several types of non-contrast MRA methods have been investigated for the peripheral arterial system. Time-of-flight [12] and phase contrast angiography [13] rely on the fact that blood is moving relative to surrounding, stationary background signal in order to generate contrast; however, these methods may fail in the lower extremities where a wide range of blood velocities and vessel orientations exist. Flow-spoiled fresh-blood imaging techniques utilize systolic- and diastolic-phase acquisitions and a subsequent image subtraction to generate contrast between arteries and surrounding tissues [14, 15]. These methods must be tailored to each patient and each station, as the amount of flow-spoiling must be adjusted depending on arterial flow rate.

Flow-independent angiography (FIA) was first investigated as a method by which the intrinsic tissue properties of blood could be used to generate contrast, rather than its flow properties. As such, regions of slow, in-plane, and retrograde flow often found in patients may be imaged. FIA was first implemented using a spin-echo sequence with a projection readout [16], with later iterations of the technique utilizing magnetization prepared methods [17, 18] and most recently a balanced SSFP (bSSFP) sequence [19, 20]. Blood has a long T_1 and a variable T_2, depending on its oxygenation status [21]; blood-muscle and arterial-venous contrast is therefore obtained via T_2-weighting of the images.

1.4.1 TSE Sequences

The turbo spin echo (TSE) sequence has become the clinical workhorse for rapid T_2-weighted imaging [22]. TSE-type sequences are capable of efficient T_2-weighted imaging, but conven-

tional TSE sequences have a non-zero first moment at the RF pulses and at odd echoes, and are therefore susceptible to flow-related artifacts and signal loss [23].

1.4.2   Spiral Imaging

The most common k-space traversal trajectories used in MRI are Cartesian based. Cartesian scanning is desirable due to the ease of image reconstruction, but requires a greater number of readout events to fully sample k-space for a given field of view than other trajectories. Additionally, rectilinear imaging requires the application of gradient pulses prior to data acquisition that necessitate more advanced moment nulling techniques to avoid flow artifacts.

In contrast to Cartesian trajectories, spiral trajectories much more efficiently cover k-space for data acquisition [24]. Additionally, the gradient moments associated with spiral imaging are small and are easily nulled with careful rewinder design. This, along with speedy acquisition times, makes spiral imaging resistant to flow-related artifacts [25].

1.5   Fluorine Imaging

MRI offers the possibility to combine anatomical and functional scans using the same equipment, lowering scan times, cost, and complexity of data interpretation. However, functionalizing MRI is still in early stages, and much work needs to be done before it is ready to enter the clinic in an impactful way.

1.5.1   Inflammation, imaging, and cardiovascular disease

Chronic inflammation has been associated with a host of diseases, including cancer [26], diabetes [27], bowel disease [28], arthritis [29], and cardiovascular disease [3, 30]. Current

methods for non-invasive inflammation detection are FDG-PET/CT [31] and T_2-weighted MRI [32]; however, both methods are indirect. The ability to directly quantify inflammatory responses non-invasively might allow more accurate risk stratification, better monitoring of therapy response, and better evaluation of novel drugs through serial imaging studies. In particular, understanding the inflammatory response to myocardial infarction (MI) may aid in the diagnosis and treatment of patients presenting with MI. Additionally, the identification of atherosclerosis as an inflammatory disease, characterized by lipid and inflammatory cell accumulation in the arterial intima, provides context to the complex physical and chemical environment focally present at atherosclerotic lesions [3, 4]. These environments provide rich opportunities for cellular and molecular targeting strategies for non-invasive imaging of inflammation [33].

1.5.2   Second-color MRI

Traditional contrast agents used for MRI work by altering the relaxation properties of nearby water protons via iron particles or gadolinium chelates [34]. Iron particle imaging suffers from partial volume effects, nonspecific origin of signal voids, and difficulty in quantification of void volume. Gadolinium liposomes, for the most part, must be large (on the order of several hundred nm), restricting their use to targets exposed to the blood stream. Additionally, there is some concern with toxicity for gadolinium-based agents, limiting their use in cell-labeling experiments. For all agent classes, the concentration of agent that resides in the region of interest can be extremely small, requiring pre- and post-contrast images to detect the small proton signal change amongst the large background signal. This necessity increases the overall study time as well as the chance of artifacts due to between-scan motion.

For these reasons, second-color (also called "hot-spot" or "PET-like") MRI has generated significant interest. Instead of attempting to detect a small change in the proton signal, a secondary nucleus is introduced which is also detectable by MRI. Fluorine-19 (^{19}F), in particular, is an attractive nucleus for this application as it has a 100% natural abundance, has a sensitivity that is 83% that of proton's, resonates closely to proton (requiring minimal hardware modification to image fluorine), and has no detectable background signal [35]. Fluorine has been studied as an MR-active nucleus since the 1970s [36] and perfluorocarbons (PFCs), which are the predominant molecular structure by which fluorine has been imaged, have been seriously studied as blood substitutes and MR contrast agents [37, 38] since the 1980s. Since then, ^{19}F imaging has also been utilized for cell-tracking [39, 40], tumor imaging [41], and especially in imaging of inflammation [42–47]. The C-F bond in perfluorocarbons is amongst the strongest chemical bonds known to man; consequently, PFCs are some of the most stable and inert molecules available for any application. Since the C-F bond does not naturally occur in biologic systems, there are no enzymes that can break it; thus PFCs are not metabolized and may remain in the body indefinitely with no adverse effects (expanded PTFE, known as Gore-Tex$^{\circledR}$, has been used in implant devices for many years). The extreme hydrophobicity of PFCs necessitates emulsifications of nano- and micron-sized PFC-containing particles for imaging applications. Depending on the PFC used and field strength, ^{19}F in this form often has T_1 relaxation times of 1-4 seconds, and T_2 relaxation times on the order of several hundred ms. The organ-retention half-life for these particles ranges from days to months [48], and they are typically excreted via exhalation from the lungs.

Another area in which ^{19}F MRI has generated significant interest is in functional lung

imaging where, despite generating much less SNR than hyperpolarized helium or xenon, ^{19}F gases offer several advantages in that they are easy to manage, can be mixed with oxygen, do not require a polarizing apparatus, and are cheap. Direct measurement of several parameters related to lung function, including airspace size, regional oxygen partial pressure, ventilation distribution, ventilation/perfusion ratios, and gas exchange has been accomplished with ^{19}F gases [35]. In comparison with liquid PFCs, gaseous ^{19}F compounds often have drastically reduced T_1 and T_2 relaxation times, ranging from around 2 ms for sulfur hexafluoride (SF_6) to around 10 or 20 ms for fluoroethane and fluoropropane gases.

1.5.3 Fluorine MRI Acquisitions

For the most part, standard pulse-sequence strategies are employed to image fluorine, with slight modifications to excite only particular fluorine resonant frequencies (for molecules with multiple resonant frequencies) [49], or with sequence timing altered to accommodate relaxation rates of perfluorocarbons. In order to obtain reasonable voxel sizes during an *in vivo* imaging session, dozens or hundreds of averaging scans are often used, resulting in lengthy examination times. Due to the low sensitivity of MR, there is a need for better-optimized acquisition approaches for fluorine imaging.

1.5.4 Model-based medical imaging reconstruction

For all cellular and molecular contrast agents, the concentration of agent that actually accumulates at the region of interest is limited by dose volume, particle size, receptor and ligand concentrations, and ligand specificity to desired receptors. Fluorine is advantageous since it has no tissue background signal and thus, subtraction techniques are not required for signal

detection. However, the received signal is still extremely small due to the inherently low concentrations of agent delivered to the tissue, and may easily reside at or near the noise in a typical experiment. Constrained reconstruction techniques, which incorporate boundary information regarding predetermined image properties, have been shown to improve noisy images by forcing smoothness across the image, or across parts of the image. ^{19}F imaging with MRI offers the possibility to incorporate anatomical knowledge of the problem derived from standard proton images acquired concurrently with fluorine images. For examples from closely related fields, Haldar et al. [50] incorporated anatomical information into constrained reconstructions of low-SNR MR diffusion data, and Dewaraja et al. [51] showed that incorporating boundary information from CT images into iterative SPECT reconstructions can improve the resultant images.

1.6   Dissertation Overview

The remainder of this dissertation is organized as follows:

Chapter 2 introduces a new, hybrid pulse sequence that shares characteristics with TSE and bSSFP sequences. The principles of FIA in the context of this new TSE sequence, including a description of tissue contrast properties, are described. Additionally, a method for fat/water separation based on phase detection is presented for this application which makes use of the bSSFP properties of the rTSE echo train.

The sequence developed in Chapter 2 suffers from insufficient fat suppression and venous contamination of resultant MRAs. In Chapter 3, the Cartesian sequence is modified to utilize spiral readouts in order to take advantage of some of the unique properties afforded

by non-Cartesian imaging.

During sequence development, a particular resistance to off-resonance blurring of so-called redundant spiral in/out gradients was discovered. Chapter 4 describes this finding in detail.

In Chapter 5, our focus shifts to the development of second-color MRI methods for imaging inflammation in myocardial infarction and early-stage atherosclerosis. An SNR efficiency comparison between common ^{19}F MRI sequences is presented along with applications of model-based iterative reconstruction techniques designed to improve the quality of low-SNR ^{19}F images by incorporating boundary information derived from accompanying proton images.

Finally, Chapter 6 summarizes the contributions of the author and collaborators in this dissertation, and provides an outlook for future research in this field.

Chapter 2

Refocused TSE

2.1 Introduction

As mentioned in Chapter 1, several types of non-contrast MRA methods have been investigated for the peripheral arterial system. Time-of-flight [12] and phase contrast angiography [13] rely on the fact that blood is moving relative to surrounding, stationary background signal in order to generate contrast; however, these methods may fail in the lower extremities where a wide range of blood velocities and vessel orientations exist. Despite relying on arterial inflow, the recent quiescent-interval single-shot (QISS) technique is a promising new method that utilizes an inversion preparation in order to improve background suppression and obtain good arterial contrast [52]. Flow-spoiled fresh-blood imaging techniques utilize systolic- and diastolic-phase acquisitions and subsequent image subtraction to generate contrast between arteries and surrounding tissues [14, 15]. These methods must be tailored to each patient and each station, as the amount of flow-spoiling must be adjusted depending on arterial flow rate.

Flow-independent angiography (FIA) was first investigated as a method by which the

intrinsic tissue properties of blood could be used to generate contrast, rather than its flow properties [16–20]. As such, regions of slow, in-plane, and retrograde flow often found in patients may be imaged. Blood has a long T_1 and a variable T_2, depending on its oxygenation status [21]; blood-muscle and arterial-venous contrast is therefore obtained primarily via T_2-weighting of the images.

By sorting later echoes into the center of k-space, TSE sequences are capable of rapid T_2-weighted imaging without the need for complex preparatory pulses; however, conventional TSE sequences have a non-zero first moment at the RF pulses and at odd echoes, and are therefore susceptible to flow-related artifacts and signal loss. This sensitivity to motion makes these sequences unsuitable for applications involving flowing spins. Conversely, balanced Steady State Free Precession (bSSFP) sequences have been shown to have good motion insensitivity [53] and have been used for FIA. Conceptually, a bSSFP sequence run with 180° RF pulses is identical to a TSE sequence with balanced inter-pulse gradients and phase alternation of the refocusing pulses. In this chapter, we therefore propose a modification of the traditional TSE sequence to reduce its vulnerability to flow-related signal modulation by incorporating zeroth-order rewinding of the readout gradient and phase alternation of the RF pulses analogous to common implementations of bSSFP sequences. We hypothesize that such a hybrid sequence will be capable of rapidly acquiring angiographic data. A similar version of this hybrid sequence has been applied for T_2-weighted imaging of edema, but not for MRA [54].

The purpose of this work, therefore, was to develop a 3D refocused TSE (rTSE) sequence for generating peripheral angiograms and to explore the signal behavior generated by such a sequence. Additionally, patients with PAD were studied in order to preliminarily assess the
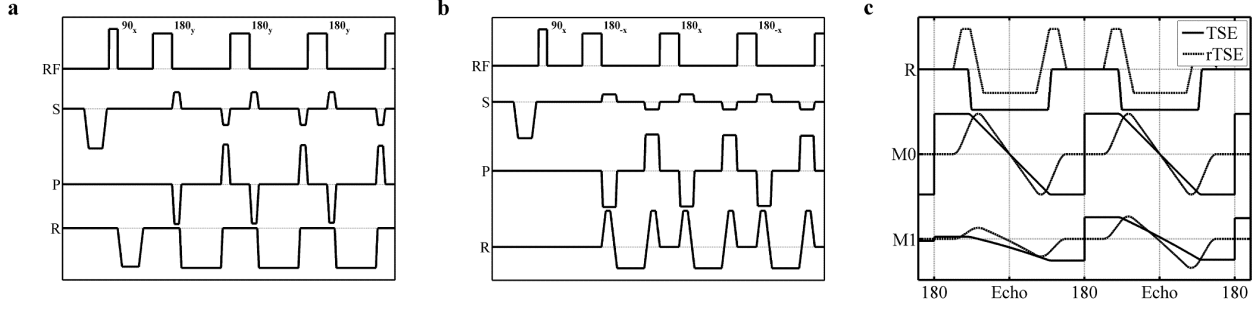
Figure 2.1: Pulse sequence diagrams. (a) The traditional TSE pulse sequence utilizes a CPMG echo train and an unbalanced readout gradient. (b) The rTSE sequence's RF pulses are phase alternated in the same manner as in bSSFP sequences, and the readout gradient is zeroth-order rewound during each echo spacing. (c) Comparison of the zeroth and first moments of the TSE and rTSE readout gradients shows the offsets generated by the TSE sequence's gradients at the RF pulses and at odd echoes. (S, slice-select gradient; P, phase-encoding gradient; R, readout gradient; M0, zeroth moment; M1, first moment.)

efficacy of the rTSE sequence in a clinical setting.

2.2   Sequence Design

The proposed sequence is shown in Figure 2.1, which compares a traditional TSE sequence to the rTSE sequence. The standard TSE sequence's RF pulses follow a 90°_x-$(180^\circ_y$-180°_y-$)$ phase condition while the rTSE sequence utilizes phase cycled pulses: 90°_x-$(180^\circ_{-x}$-180°_x-$)$, to be discussed in the next subsection. Within each echo spacing, the readout gradient of the rTSE sequence is modified such that the first moment returns to zero prior to the application of the next RF pulse. While further moment nulling techniques are available to ensure the first moment is also zero at the center of the echo, prior studies have shown good flow insensitivity using only zeroth-order moment nulling [55].

2.2.1 Rationale for RF Phase Alternation

Because the rTSE sequence is conceptually equivalent to a 180°-α-pulse-bSSFP sequence, we hypothesized that a phase-alternated RF approach would perform better in the presence of inhomogeneity than the CPMG phase condition. To asses this, Bloch equation simulations were performed to explore three TSE sequence variants' performance in the presence of B_1 and B_0 non-idealities. Simulations were performed with a traditional TSE sequence with CPMG RF phases, an rTSE sequence with CPMG RF phases, and an rTSE sequence with bSSFP-style RF phases. B_1 inhomogeneity was simulated by a 64-echo spin-echo train with 120°, 140°, 160°, and 180° refocusing RF pulses (with no off-resonance). B_0 inhomogeneity was simulated with a 64-echo spin-echo train with 0°, 60°, 120°, and 180° phase accrual during each echo-spacing with RF flip angle 160° (without B_1 inhomogeneity, B_0 inhomogeneity has no effect on the signal). For all simulations, echo spacing = 5 ms, T_1 = 2000 ms, T_2 = 200 ms; a rough approximation of blood signal and a reasonable value for echo spacing.

Figure 2.2 demonstrates the improved performance of the rTSE sequence when bSSFP-style phase alternation of the RF pulses is used. The standard TSE sequence displays the expected resistance to B_1 and B_0 inhomogeneities due largely to the presence of crusher gradients which select the spin-echo and suppress Free Induction Decay (FID) and stimulated echo components from the acquired signal by dephasing incidental signal excited by imperfect refocusing pulses [22]. Without these crusher gradients, the sequence strongly resembles a bSSFP sequence, and bSSFP-style phase alternation of the RF pulses results in better resistance to inhomogeneities than traditional CPMG-style phases, demonstrated by the smoother signal decay curves in Figure 2.2. These smoother decay curves result in less
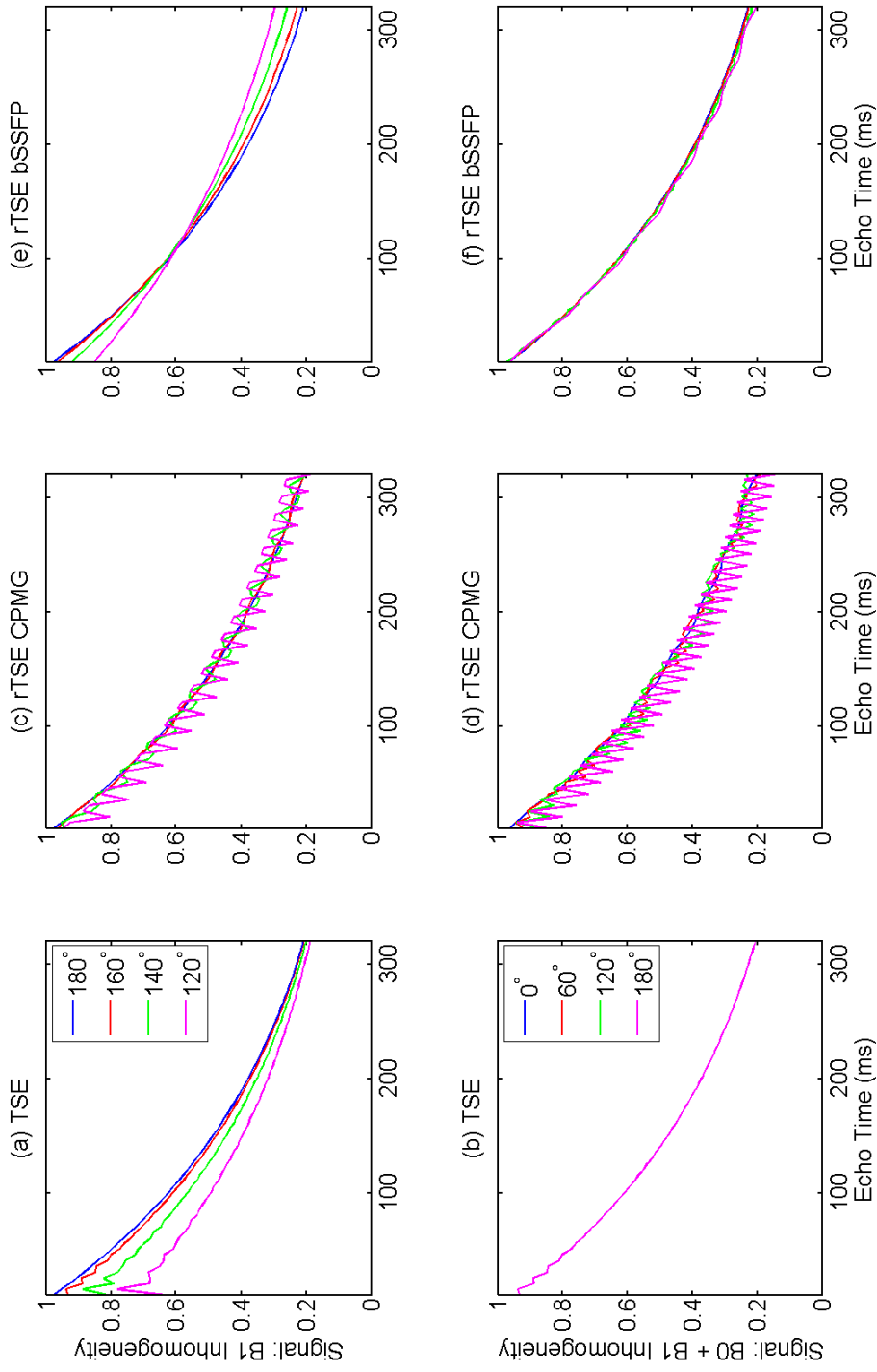
Figure 2.2: Bloch equation simulations for the standard TSE sequence (a,b), a refocused-gradient TSE sequence with CPMG-style RF phase prescription (c,d), and a refocused-gradient TSE sequence with bSSFP-style RF phase prescription (e,f). Top row shows the sequence variants' response to B_1 inhomogeneity; Bottom row shows response to combined B_0 and B_1 inhomogeneity.

partition-to-partition magnitude differences in 3D k-space, which translates to fewer artifacts in the resulting images.

2.2.2   Background Tissue Description and Suppression

In angiography, positive contrast is required between arterial blood and all other tissues, which – in the leg – can broadly be classified as either muscle or fat .(Extravascular fluid may be ignored in some cases, or may be easily suppressed by a long-TI inversion pulse.) In FIA, we must also be concerned with generating contrast between arterial and venous blood, since there is no spatiotemporal dependence of blood contrast as in contrast-enhanced angiography or time-of-flight methods.

To identify optimal sequence timing parameters for background suppression, Bloch equation simulations were again performed to assess signal evolutions for arterial blood, venous blood, muscle, and fat during an rTSE echo train. Muscle has a short T_2 (around 30 ms at 3.0 T), so any choice of TE longer than about 80 ms yields good muscle suppression (Fig. 2.3). Venous T_2 is dependent on oxygen status and echo spacing [21] (to be discussed more fully in Chapter 3); Figure 2.3 also shows artery-vein contrast for venous blood across a range of oxygenation states. As venous oxygenation increases, the difference between arterial and venous oxygenation becomes smaller, and less contrast is observable between the two; however, choosing a long TE (180-230 ms) with typical echo spacings of 3-5 ms generally results in discernible contrast between arteries and veins. For these simulations, arterial and venous effective T_2 was estimated using the model described in Section 3.2.

As has been mentioned previously, the rTSE sequence is conceptually identical to a bSSFP sequence run with 180° α pulses. A consequence of this is that any spins that experience a

less-than-perfect refocusing pulse due to B_1 inhomogeneity will approach a non-zero steady-state value as if they were in the transition period of a high-flip-angle bSSFP sequence. (For spins that experience a true 180° pulse, while they are technically also exhibiting bSSFP-style signal evolution, their steady-state value is zero and the signal decay curve is smooth.) Fat, in particular is susceptible to this effect due to its short T_1 , as imperfect refocusing pulses will have a relatively large amount of regrown longitudinal magnetization to act upon. Bloch equation simulations are shown in Figure 2.4 for fat that has been nearly completely suppressed prior to the 90° excitation pulse with a chemically selective saturation pulse. As B_1 inhomogeneity increases, fat signal rises as it approaches a steady state value. Figure 2.5 further demonstrates this effect and contrasts the behavior of fat in a crushed versus non-crushed TSE sequence. For these simulations, an imperfect fat saturation pulse was simulated, as might occur due to B_1 inhomogeneity. The fat saturation pulse had a simulated flip angle of 110°, resulting in a negative M_z and the resulting "bounce" point in Figure 2.5 as the magnetization crosses zero. This figure also shows the results of an experiment in which a bottle of vegetable oil was placed in the scanner and the rTSE sequence run without phase encoding gradients. The magnitude of the resulting echoes shows the same behavior as that predicted by simulations.

2.3   *In vivo* imaging experiments

Nine healthy volunteers (5 male, mean age 24.0 +/- 1.7) with no symptoms of cardiovascular disease were examined. Additionally, 4 patients (2 male, age 65.5 +/- 9.0) who were sched-uled for peripheral runoff examinations were scanned to assess the viability of the sequence
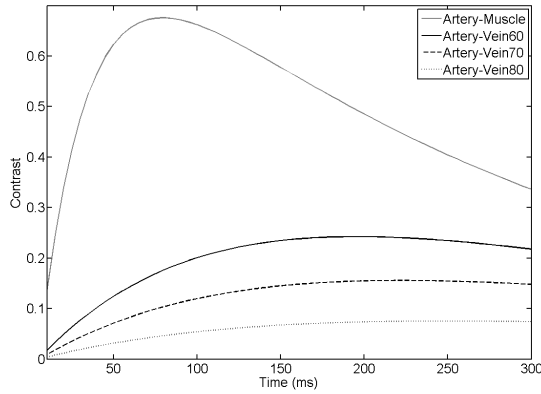
Figure 2.3: Artery-Muscle and Artery-Vein contrast as a function of echo time in a spin-echo sequence. Artery signal was simulated using an oxygenation value of 95% (See Section 3.2); venous oxygenation is indicated in the figure legend (e.g. Vein70 indicates 70% venous oxygenation). As venous oxygenation increases, maximum contrast decreases and moves to later echo times.
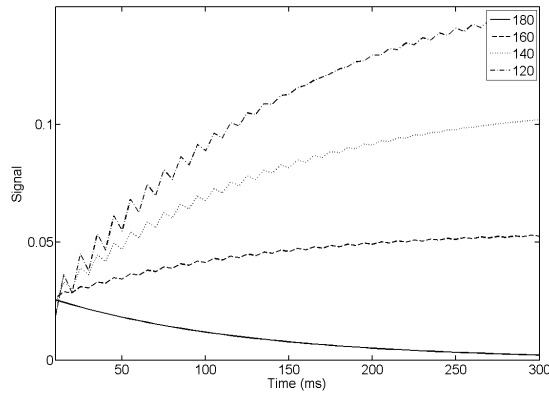
Figure 2.4: Fat signal as a function of echo time in the rTSE sequence. As B_1 inhomogeneity increases, fat signal rises from an initially suppressed state towards its steady-state value, determined from the particular flip angle it experiences and its specific off-resonance. Numbers in figure legend indicate the refocusing flip angle simulated (i.e. degree of B_1 inhomogeneity).
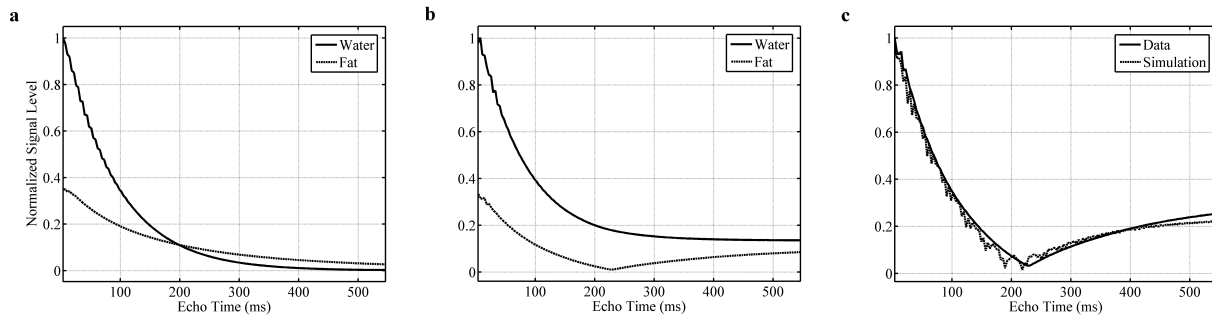
Figure 2.5: Relaxation behavior of fat and water in a spin-echo train. (a) Simulated signal levels of fat and water in a crushed TSE sequence with 150° refocusing pulses. (b) Simulated signal levels of fat and water in a non-crushed, or totally refocused, sequence for 150° refocusing pulses. Note the approach to a steady-state value for both fat and water signals. (c) Comparison of simulated fat signal from (b) with data from vegetable oil bottle phantom, showing similar behavior.

in a clinical setting (2 patients received contrast-enhanced MRA; 2 received 2D time-of-flight imaging). The protocol was approved by the Institutional Review Board at the University of Virginia Health System and all participants gave written informed consent.

2.3.1   Scan Parameters

In order to compare the rTSE and TSE sequences, the scan protocol consisted of the acquisition of a 3D dataset with a standard TSE sequence, followed immediately by a dataset using the rTSE sequence. In two volunteers, a three-station protocol was implemented covering arterial tree from the pelvis to the ankle. In one volunteer, only the thigh and calf stations were obtained, and in all other volunteers, only the thigh station was acquired. Scans were conducted on a Siemens 3.0-T Trio scanner (Siemens Medical Solutions) with a TR = 3000 and TE = 230. Echo spacing = 3.44 ms, resolution 1.4 x 1.4 x 1.5 mm^3, refocusing flip-angle 180°, acquisition time 5.38 +/- 0.5 minutes per station and a chemical fat saturation pulse was applied prior to each excitation pulse. Peripheral MRA coils placed anteriorly and laterally and a spine coil placed posteriorly were used for imaging. In one volunteer, four datasets were acquired with echo times of 150, 200, 230, and 275 ms for comparison with the vessel contrast simulation discussed previously. Three regions of interest (ROIs) per echo time were drawn in the upper, middle, and lower portions of the imaging volume, as will be discussed shortly.

In patient scans, prior to a standard ceMRA or 2D TOF scan, three stations were acquired in each patient using the rTSE pulse sequence in the same manner described above, covering the vasculature from the aortic bifurcation to the ankle. One patient was unable to tolerate the procedure and was excluded from analysis. The conventional TSE sequence was not

included in the patient protocol due to time constraints.

Image quality was compared based on signal-to-noise ratio (SNR), vessel contrast reso-lution, and arterial vessel sharpness of transverse images across the 3D volume. All analyses were performed using axial images from the 3D volumetric data. Arterial SNR is defined as,

$$\text{SNR} = \frac{A}{\sigma_N} \tag{2.1}$$

where A is the mean arterial signal and σ_N is the standard deviation of the noise, measured in a region of the image containing only air. Vessel contrast resolution is defined as,

$$\text{Contrast Resolution} = \frac{A - V}{A + V} \tag{2.2}$$

where V is the mean venous signal. That is, contrast resolution is the difference in signal intensity values between the femoral artery and vein divided by the sum of these intensity values.

Arterial sharpness was quantified by calculating the two-dimensional magnitude of the image gradient and recording the maximum gradient across the femoral artery at three locations and orientations. The average maximum gradient value from these measurements was taken as an overall measure of vessel sharpness in the image.

Differences between groups were assessed with a two-tailed paired (for TSE versus rTSE data from volunteers) or unpaired (for patient versus volunteer rTSE data) t-test with a p-value of 0.05 considered to be significant.

2.3.2 Results

Figure 2.6 demonstrates that the incorporation of the changes outlined above into a traditional, Cartesian TSE scan results in angiograms with good artery/vein delineation and good muscle suppression. Figure 2.7 shows simulation results across a range of echo times for arterial and venous signal using the Luz-Meiboom model. Overlaid on the solid line of simulation data are data points taken from axial ROIs in the femoral artery and vein from a normal, female volunteer at different echo times, showing good agreement with simulated data. Although SNR was similar compared to the traditional, spoiled TSE technique, the contrast and vessel sharpness were both improved using the rTSE sequence (Fig. 2.8). However, as expected from simulations, fat signal is less uniform in the rTSE image compared to TSE; it appears brighter in some areas and darker in others as the robustness of fat suppression and B_1 homogeneity vary over the imaging volume.

Figure 2.9 demonstrates use of the rTSE sequence in the calf station of a normal volunteer. Excellent artery-background contrast is obtained in most areas.

Figure 2.10 demonstrates the effectiveness of the Cartesian rTSE scan in detecting a lesion in the left leg of a 76 year old female patient. The rTSE sequence (left) was able to successfully image the stenosis visible in a 2D time-of-flight scan (right). Although arterial-venous contrast in patients was less than that in normal volunteers (Fig. 2.11), the stenosis in the mid-thigh is clearly visible in both images. The SNR and vessel sharpness in the patient images were similar to those in the volunteers.

In both patients with obstruction of the femoral artery in the thigh (as determined from 2D time-of-flight images), the rTSE successfully imaged the stenosis. Abdominal-station
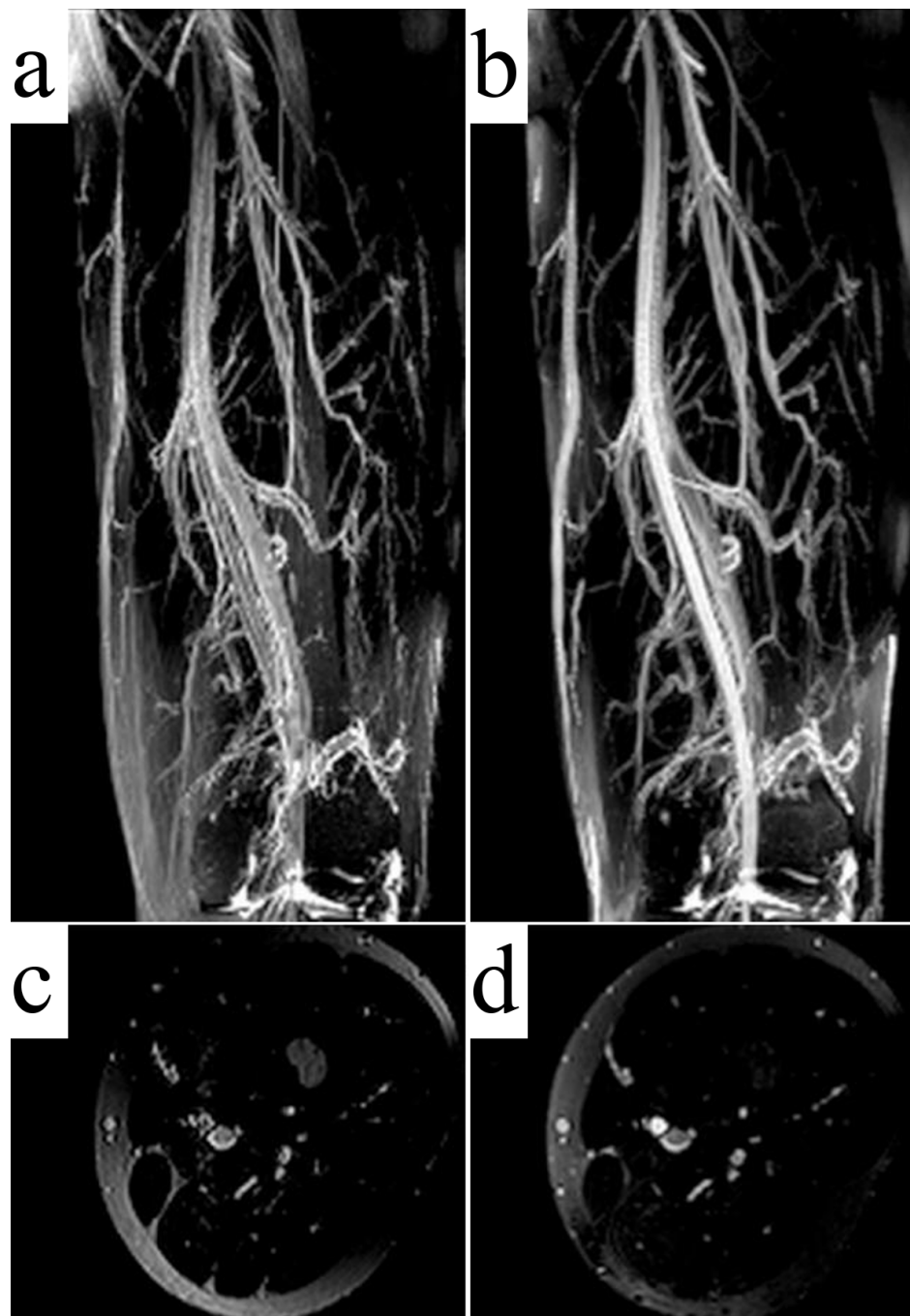
Figure 2.6: Coronal MIPs of the thigh station of a normal volunteer TSE (a), and rTSE (b) scans. Axial reformats of the imaging volume are shown in (c) and (d) for the TSE and rTSE scans, respectively.
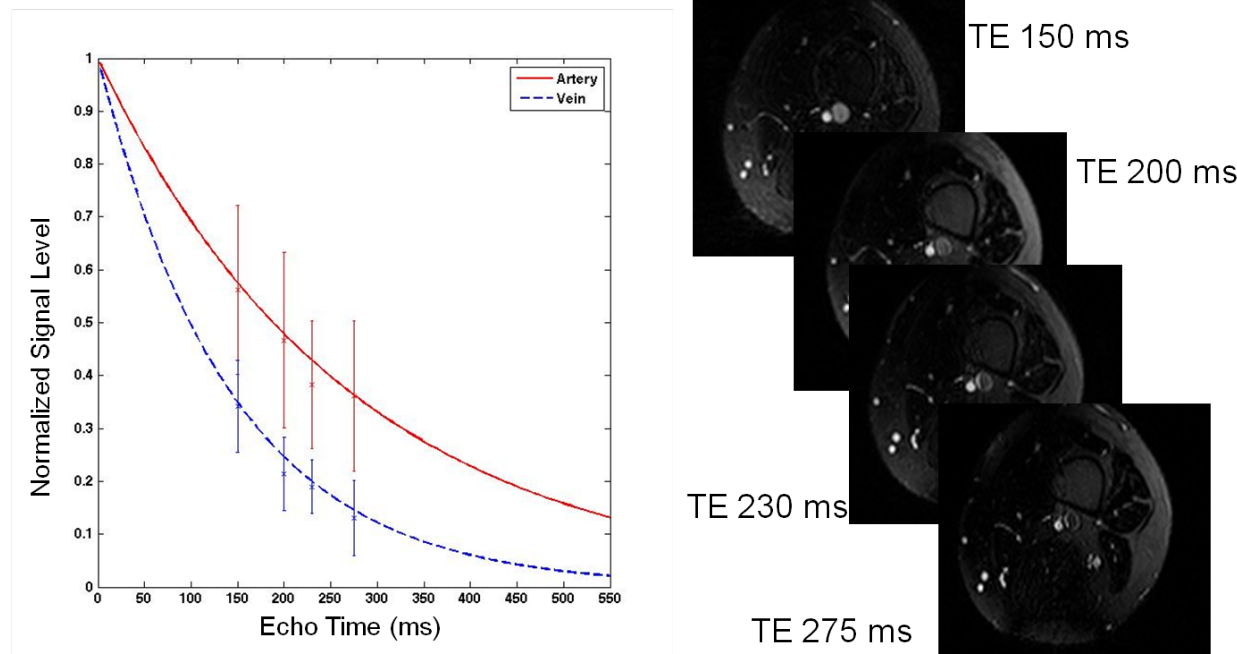
Figure 2.7: Simulated arterial and venous signals as a function of echo time. Experimental data from a female volunteer closely matches the simulated signals. Maximum contrast between arteries and veins is developed at 230 ms for the echo spacings used in this experiment.
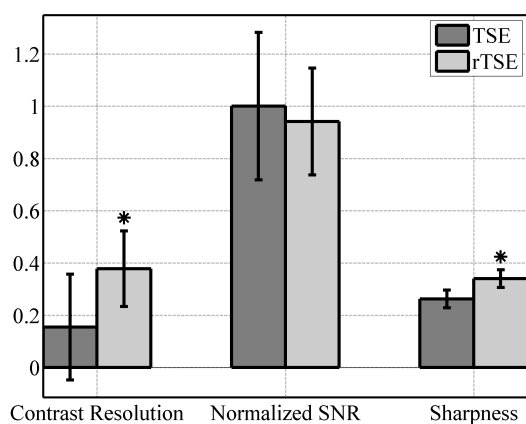
Figure 2.8: Contrast resolution, SNR, and vessel sharpness comparisons between TSE and rTSE pulse sequences. SNR was similar between sequences, but rTSE had significantly better contrast resolution and vessel sharpness. Normalized contrast resolution 0.155 ± 0.202 for TSE vs. 0.378 ± 0.145 for rTSE - $p < 0.01$; sharpness 0.263 ± 0.034 for TSE vs. 0.340 ± 0.034 for rTSE - $p < 0.005$.
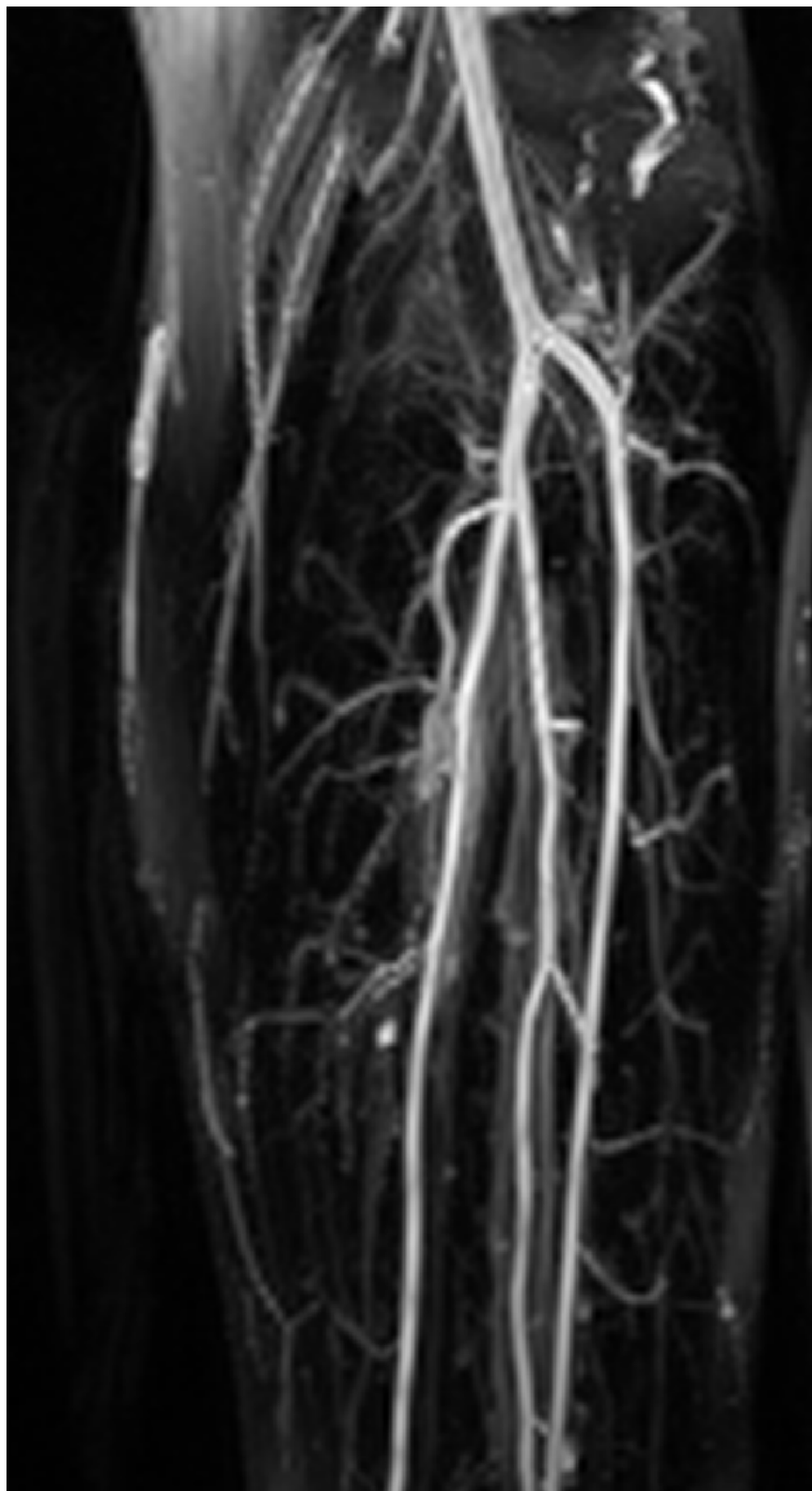
Figure 2.9: Coronal MIP of the left-calf station of a normal volunteer rTSE scan.
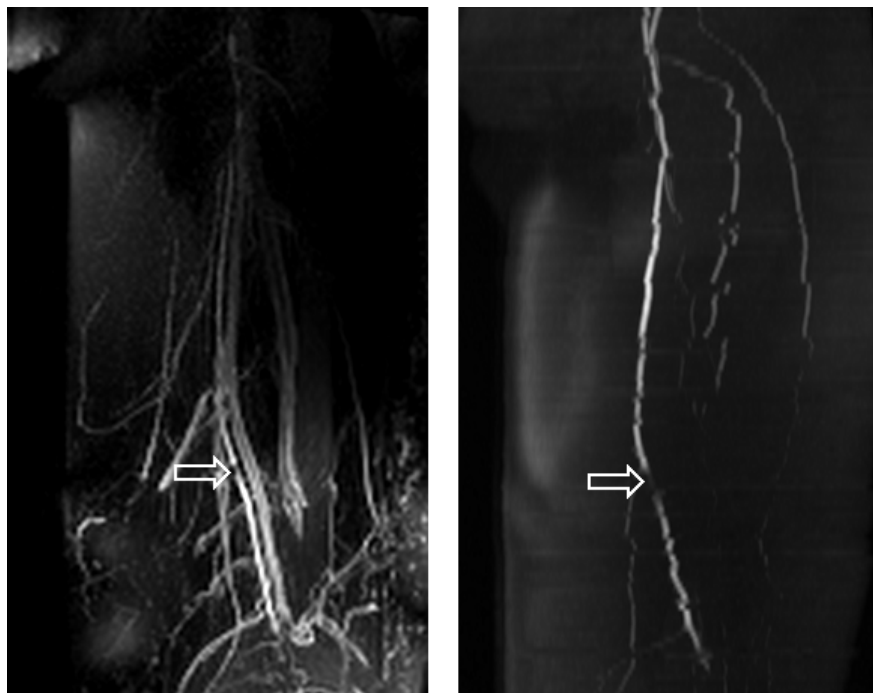
Figure 2.10: Coronal MIP of the left-thigh station of a patient rTSE scan (left), and 2D TOF (right). Open arrow indicates position of a focal stenosis in the distal superficial femoral artery.

obstructions were more difficult to identify due to wrap-around artifacts caused by large patient size.

2.3.3   Discussion

Patient SNR and vessel sharpness values were similar to those obtained in normal volunteers; however, a statistically significant reduction in contrast resolution was observed. This may
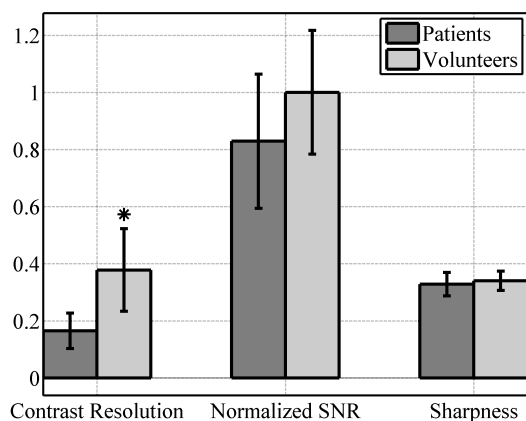
Figure 2.11: Comparison of contrast resolution, SNR, and vessel sharpness between volunteers and patients. Artery-vein contrast was significantly lower in patients as compared to volunteers. SNR and vessel sharpness were comparable between the two groups. Normalized contrast resolution 0.165 ± 0.062 for patients vs. 0.378 ± 0.145 for volunteers - $p < 0.01$.

be attributed to decreased arterial oxygenation in patients, or to increased venous T_2 due to decreased oxygen consumption by the associated tissue in PAD. In either case, the TE of 230 ms was determined from a set of healthy data (along with a model) and may not be the optimal choice for the reduced oxygenation difference between arteries and veins found in patients. The Luz-Meiboom model indicates that higher field-strength is desirable to decrease venous T_2. In our experience, a 30% improvement in arterial-venous contrast is achieved by performing these studies at 3.0 T, rather than at 1.5 T, but comes at a cost of increased inhomogeneity and safety concerns due to the power deposition of multiple, lengthy echo trains in a 3D sequence. However, adaptation of the protocol to satisfy SAR limits by increasing the TR was only necessary in 2 volunteers.

The Luz-Meiboom model (Section 3.2) is helpful in examining other ways to improve the artery-vein contrast and indicates that, in addition to allowing for higher resolution images, longer echo spacings are desirable to increase contrast in the final images [20, 21, 56]. However, lengthening the echo spacing in our current Cartesian rTSE sequence has a negative impact on scan time due to acquisition segmentation which is necessary in order to restrict echo train lengths to reasonable durations. In order to achieve extended echo spacings while maintaining reasonable scan times, spiral readout gradients could be used to more efficiently sample k-space, as they can acquire a similar amount of data in far fewer readout periods. Furthermore, spiral gradients are naturally resistant to artifacts due to flow and motion, making them excellent candidates for a sequence wherein blood motion must be neglected. The modification of the 3D TSE sequence to utilize spiral readout gradients is explored fully in Chapter 3.

Bright fat in TSE images is a well-documented phenomenon and is due to T_2 lengthening

via the removal of J-coupling-induced dephasing by rapidly-applied refocusing pulses [57]. In addition to this, fat appears less uniform, and in some areas brighter, in rTSE images compared to TSE images despite the use of fat saturation prepulses. This is due to FID and subsequent stimulated-echo components from imperfect refocusing pulses entering the echo train, and a more robust (or at least less variable) suppression of this signal by the traditional, unbalanced TSE gradient scheme. Dephasing this signal (which occurs naturally in a traditional TSE pulse sequence due to non-zero gradient moments) attenuates it by the time the center of k-space is sampled. The rTSE sequence, by nature of its balanced gradients, does not suppress this incidental fat signal, which will have a variable strength when the $k = 0$ line is acquired dependent on its particular precessional frequency and the refocusing flip angle it experiences. It should be noted that while we have discussed the effects of B_0 and B_1 inhomogeneity only in terms of fat in this section, any variations in field strength and/or RF strength will lead to stimulated echo effects, by which we mean artifacts caused by oscillatory behavior of echo magnitude at the beginning of the echo train and an approach to a non-zero steady-state value.

Wrap-around artifacts caused by large patient size (relative to slab-thickness) can be addressed by reducing anterior-posterior resolution, increasing scan time, or utilizing slab-selective RF pulses.

As in all T_2-weighted FIA imaging, synovial fluid appears bright in images generated by the rTSE sequence. Inversion preparation pulses can be used to reduce the signal from synovial fluid as well as the long-T_2 edematous fluid often seen in patients, at the cost of reduced overall signal.

2.4   Separating fat and water

As described, the rTSE sequence achieves flow-independent, non-contrast angiograms by blending the advantages of the TSE sequence with the bSSFP sequence. So far, the TSE-like nature of the sequence has been highlighted due to its ease in generating T_2-weighted images. In this section, we will briefly describe one method by which the bSSFP nature of the sequence can be harnessed in order to separate fat and water in rTSE angiograms.

Unlike standard TSE sequences, the rTSE sequence suffers from spurious echo artifacts which enter the latter parts of the echo train. In particular, fat suppression remains an issue with this sequence due to fat's short T_1, which causes any fat that experiences an imperfect refocusing pulse (due to B_1 inhomogeneity) to display a bright signal by the time the center echo is acquired. This fat signal <u>cannot</u> be removed by chemical suppression pulses or water-only excitation pulses since the origin of the signal is within the echo train itself.

An alternative approach to fat suppression is fat/water separation. Due to its hybrid nature, the phase detection technique proposed by Hargreaves et al. [58] for bSSFP fat/water separation is also applicable to rTSE, provided the phase transition region at the beginning of the echo train is bypassed.

2.4.1   Theory

The fat separation technique proposed in [58] for bSSFP sequences utilizes the predictable difference in phase between fat and water that arises in steady-state to separate water and fat (Fig. 2.12a).

In the rTSE sequence, data acquisition is performed during what would be called the ap-

proach to steady-state in a bSSFP sequence (Fig. 2.12b-e). However, while the magnitude of the signal approaches steady state slowly, signal phase reaches equilibrium relatively quickly.

Therefore, we can skip acquisition of the first few echoes in the standard rTSE sequence and be reasonably certain the phase behavior of the spins has settled into their final state, allowing for phase detection and fat-water separation.

Another approach is to treat the rTSE sequence even more like a bSSFP sequence and, instead of applying a single 90-degree excitation pulse, apply a series of pulses to catalyze the spin-echo-train (Fig. 2.13), forcing the phase behavior into the steady state more quickly (Fig. 2.12c,e).

2.4.2 Methods

2.4.2.1 Phantom experiment

Using a 1.5 T Siemens Avanto scanner, a doped water phantom was placed next to a fat phantom and imaged with echo spacing = 4.6 ms (to put the fat signal squarely in the middle of the negative phase plateau). For this application, the echo spacing is dictated by the resonance frequency difference between fat and water (see Fig. 2.12a). At 1.5 T, this echo spacing (4.6 ms) is easily achieved. Performing this experiment at 3.0 T would be better in terms of artery-vein contrast, but the required echo spacing of 2.3 ms is difficult to achieve with the gradient hardware available and additionally results in an unacceptable amount of SAR deposition to the patient.

A 15-pulse linear ramp from 0- to 180-degrees was used for signal catalyzation prior to data acquisition.
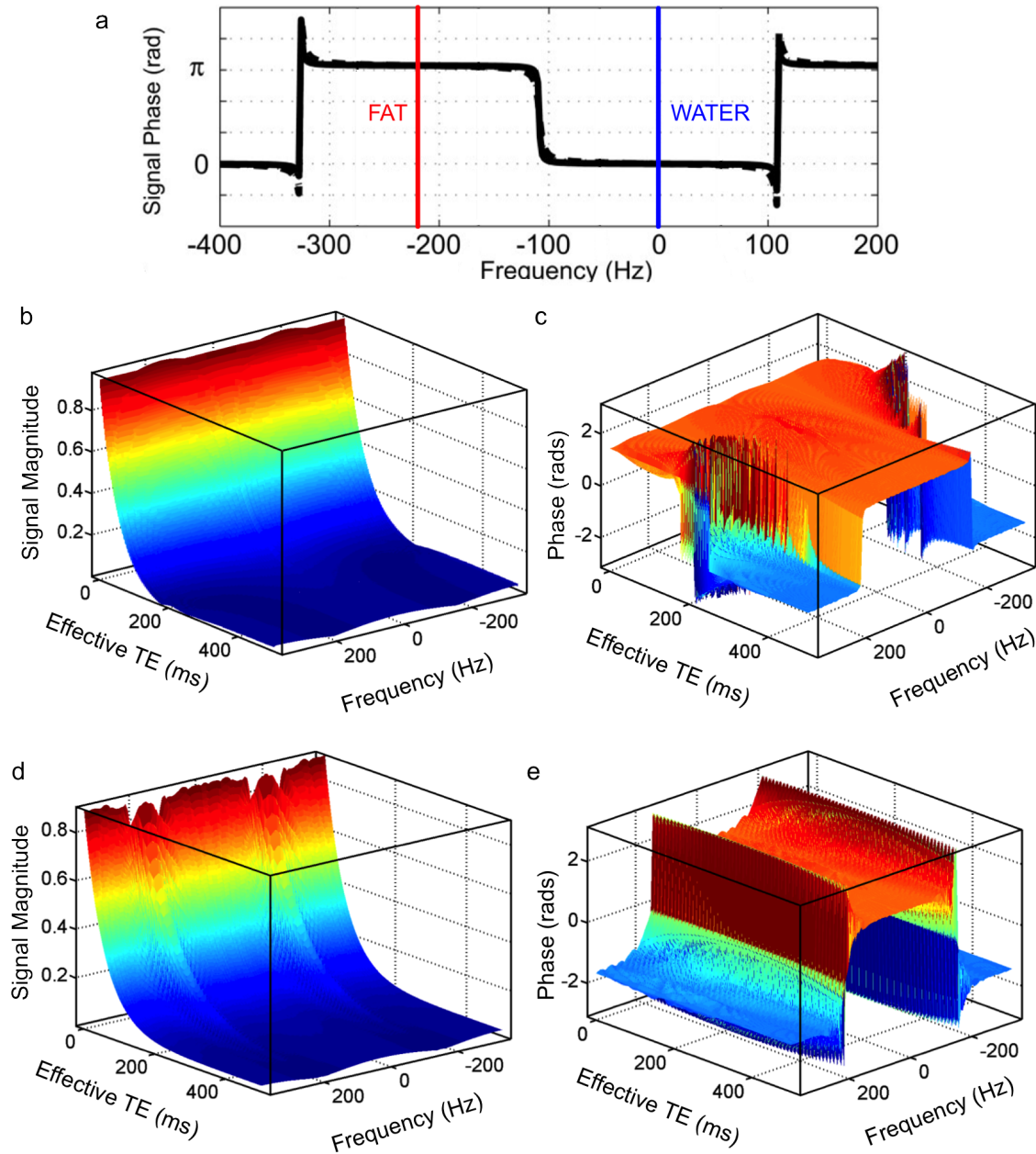
Figure 2.12: Simulated signals in fully balanced sequences. a) Signal phase across range of off-resonance values in the steady state of a bSSFP sequence (TR = 4.6 ms). With the appropriate choice of TR, the predictable difference in phase between fat and water supports simple tissue separation. b-c) Magnitude (b) and phase (c) evolution for spins experiencing an imperfect 160-degree pulse in a standard rTSE sequence. d-e) Magnitude (d) and phase (e) evolution for spins experiencing an imperfect 160-degree pulse in a linear-ramp catalyzed rTSE sequence.
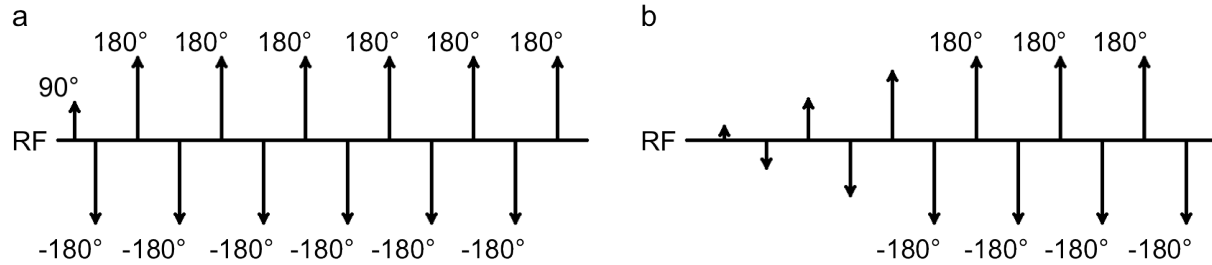
Figure 2.13: RF catalyzation schemes for rTSE sequence. a) Standard 90°_x-$(180^\circ_{-x}$-180°_x-) scheme. b) Catalyzation with 5-pulse linear ramp. Data acquisition starts after 180° pulses have begun.

Images were processed in the manner described by [58] in Matlab to separate water-only and fat-only images. Briefly, after system phase correction, the sign of the real part of each pixel value determines whether it belongs in the water-only or fat-only image.

2.4.2.2   *In vivo* experiment

One volunteer was scanned on a Siemens 1.5 T Avanto scanner with both the standard and catalyzed versions of the rTSE sequence with TR/TE 3000/150 ms, field of view 325x157x144 mm^3, using a single surface coil for reception, and chemical fat saturation prior to excitation to suppress fat in the initial portion of the echo train.

For fair comparison, both sequences skipped acquisition of the first 16 echoes. Water-only and fat-only images were calculated as before.

2.5   Results

Figure 2.14 shows images of the water and fat bottles and their ease by which they may be separated into different images with this method.

In Figure 2.15, one axial slice through the middle of the 3D volume is shown. Good
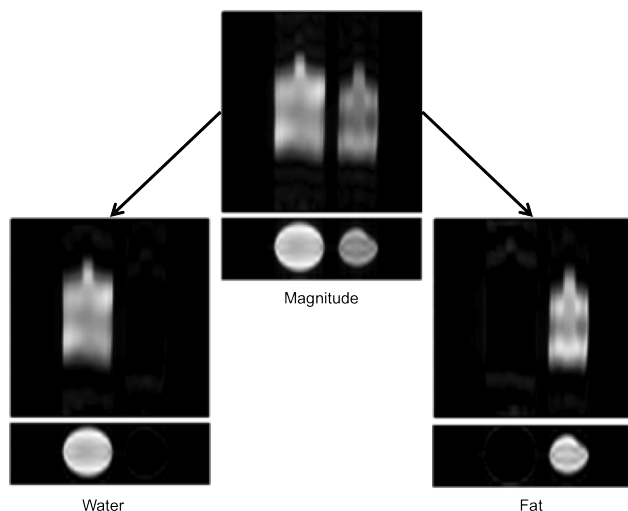
Figure 2.14: Separation of water and fat images using phase detection from a catalyzed rTSE sequence in bottle phantoms.
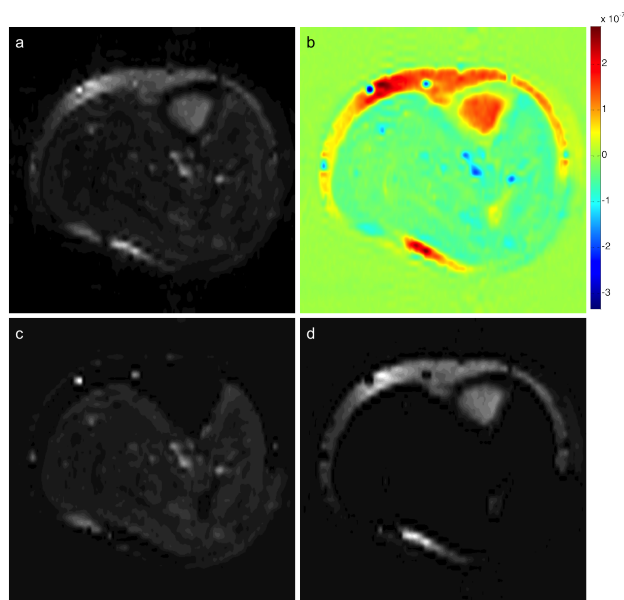
Figure 2.15: Water/fat separation in the calf of a normal volunteer. Mid-calf axial slice through the 3D volume shown in Figure 2.16. a) magnitude image. b) real part of the phase-corrected image. The sign of each pixel in this image determines whether it belongs in the water-only (c) or fat-only (d) image.

fat/water separation is obtained over nearly the entire image, with only a small portion of subcutaneous fat incorrectly identified as water.

In comparing the skipped-echo approach to the catalyzed echo train approach, it is clear that both methods facilitate phase detection for fat/water separation (Fig. 2.16), but that better background (muscle) suppression is obtained when using the skipped-echo approach. It is also clear in this image why the studies performed in Section 2.3 were performed at 3.0 T; as the artery-vein contrast in Figure 2.16 is rather poor.
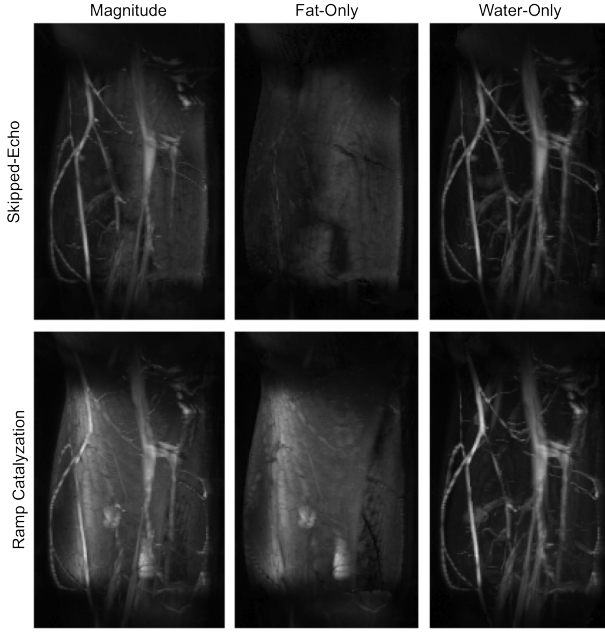
Figure 2.16: MIPs of the calf of a normal volunteer. Fat-only and water-only images are easily separated from the magnitude image in both cases, but the non-catalyzed skipped-echo sequence has better background suppression, likely due a stimulated echo effect arising from muscle in the early parts of the echo-train because of the ramped pulses.

2.5.1   Discussion

To apply phase sensitive fat/water separation in rTSE imaging, a simple skipped-echo or catalyzed-TSE approach is required to avoid the ill-defined phase transition region at the beginning of the echo train. Despite better background suppression when using the simple skipped-echo approach in this one case, the particular timing of the chaotic transition region we need to bypass is determined by a voxel's particular resonance frequency and thus inconsistent results are likely to be obtained. Due to off-resonance, we either must 1) skip more echoes than is strictly necessary to ensure all voxels have made the transition, or 2) risk data acquisition prior to all transitions having taken place. Because the catalyzed sequence forces a known and dictated phase behavior, it should provide more consistent results.

2.6 Discussion and Conclusions

The use of balanced gradients and RF-pulse phase alternation in a TSE sequence resulted in images with comparable SNR, but higher contrast resolution and vessel sharpness, than those generated without the use of balanced gradients. The rTSE sequence can be thought of as either a balanced-gradient TSE sequence, or equivalently as a high-flip-angle bSSFP sequence wherein data acquisition takes place prior to the formation of steady-state; both frames of thought can provide insight to the sequence. For example, by catalyzing the rTSE sequence with a ramped series of RF pulses, bSSFP-style phase detection can be used to separate water and fat images, albeit with poor artery-vein differentiation due to minimal echo spacings required in that instance.

That said, the rTSE sequence differs from bSSFP sequences in several important respects. First, 180° refocusing pulses provide a large echo signal level and allow T_2-weighting to be easily achieved for artery-muscle contrast similar to that of a traditional TSE sequence without additional T_2-preparation pulses. Second, because much of the imaging is carried out during the initial transient, the well-known bSSFP banding artifact is largely avoided for spins which receive approximately a 180° refocusing pulse (i.e., water). Furthermore, gating strategies necessary for other vascular beds can be more naturally applied in TSE imaging, though the transient nature of magnetization preparation already results in a necessary interruption of the signal in bSSFP FIA imaging [19], mitigating this issue somewhat.

In conclusion, the rTSE sequence is capable of rapidly generating noncontrast angiograms of the periphery without a subtraction operation by exploiting the rapid T_2-weighted imaging capability of the TSE sequence, while maintaining flow insensitivity provided by balanced-

gradient imaging. The peripheral MRA images obtained with rTSE are sharper and have better arterial-venous contrast than those obtained with a traditional TSE sequence; however, current limitations of the technique include limited artery-vein contrast, high signal of synovial and edematous fluid, and incomplete fat suppression. Despite these limitations and a reduction in arterial-venous contrast, results in patients are encouraging, as several stenotic sections identified using established MRA methods were clearly visible on rTSE images of the mid-thigh.

Chapter 3

Spiral TSE

3.1 Introduction

The sequences used for FIA have mostly been variations on magnetization-prepared bSSFP due to its efficiency in generating bright blood contrast. However, as discussed in the previous chapter, TSE sequences are capable of rapid, direct T_2-weighted imaging without the need for complex preparatory pulses. Conventional TSE sequences are susceptible to flow-related artifacts and signal loss, and this sensitivity to motion makes these sequences unsuitable for applications involving flowing spins without modifications to reduce flow sensitivity [59]. However, in cases where most of the of flow is in one known direction, the deleterious effects of net gradient moments on flow can be placed such that they do not effect the majority of flowing spins.

This chapter builds upon our previous experience with using TSE sequences for non-contrast angiography, described in Chapter 2, with two important modifications:

1. We move to spiral readouts here. Moving to spiral readouts has three main advantages

over Cartesian scanning in the case of peripheral MRA:

(a) The natural motion insensitivity of spiral gradients is attractive for a sequence wherein we wish to remove artifacts due to flow.

(b) Spiral gradients will allow for longer echo spacings, improving venous suppression according to the Luz-Meiboom model.

(c) More efficient coverage of k-space will lead to less power deposition to the patient.

Indeed, the rapid coverage of k-space by spiral scanning has been utilized for many years in applications such as in coronary imaging where scanning must be conducted quickly and with minimal motion and flow artifacts [25].

2. The sequence described in Chapter 2 was a fully-refocused TSE sequence that shares many characteristics with a bSSFP sequence. Here, we return to an unbalanced, traditional TSE sequence, but ensure flow-spoiling occurs in the least objectionable direction by placing crusher gradients in the through-plane (anterior-posterior) direction of our imaging volume.

3.2   Theory

In FIA, bright-blood contrast is obtained primarily via T_2 weighting of the images, either through a T_2-prep module [18, 19] or by acquiring late echoes in a spin-echo sequence [59, 60]. Blood has a longer T_2 than most of the tissues surrounding it in the periphery, but this T_2 is dependent on its oxygenation status and on how often refocusing pulses are applied in the spin-echo train.

Red blood cells constitute a separate compartment from the surrounding plasma, and the susceptibility of hemoglobin changes as it becomes more or less oxygenated. As water molecules are freely exchanged between the two blood compartments, protons are exposed to the variable magnetic microenvironment present within red blood cells, leading to variable amounts of dephasing. Blood's dependence on the rate at which refocusing pulses are applied is thus due to the varying amounts of time protons are resident in either compartment and the status of the local magnetic environment within the red blood cells. As refocusing pulses are applied more quickly, protons have less time to dephase and therefore, the apparent T_2 of blood becomes longer as refocusing pulses are applied more quickly. The Luz-Meiboom model of T_2 relaxation in the presence of two-site exchange and under rapid refocusing conditions, as occurs during a TSE echo train, is given by [21, 56],

$$\frac{1}{T2_b} = \frac{1}{T2_o} + (P_A)(1 - P_A)\tau_{ex}\left[\left(1 - \frac{\%HbO_2}{100\%}\right)\alpha\omega_0\right]^2\left(1 - \frac{2\tau_{ex}}{\tau_{180}}\tanh\frac{\tau_{180}}{2\tau_{ex}}\right) \qquad (3.1)$$

where $T2_b$ is the T_2 of blood, $T2_o$ is the T_2 of fully-oxygenated blood, P_A is the fraction of protons resident in one site, τ_{ex} is a measure of the average time required for a proton to move between the two sites, $\%HbO_2$ is the percent oxygenation of blood, α is a dimensionless value related to the susceptibility of deoxyhemoglobin and the geometry of the red blood cell, ω_0 is the resonant proton frequency, and τ_{180} is the echo spacing between refocusing pulses in the echo train. This equation states that as the percent oxygenation goes down or the echo spacing of the refocusing pulses increases, the T_2 of blood becomes shorter. This means that effective T_2 contrast can be generated between arteries and veins during a spin echo train with sufficiently long echo spacings between RF pulses. Figure 3.1 plots
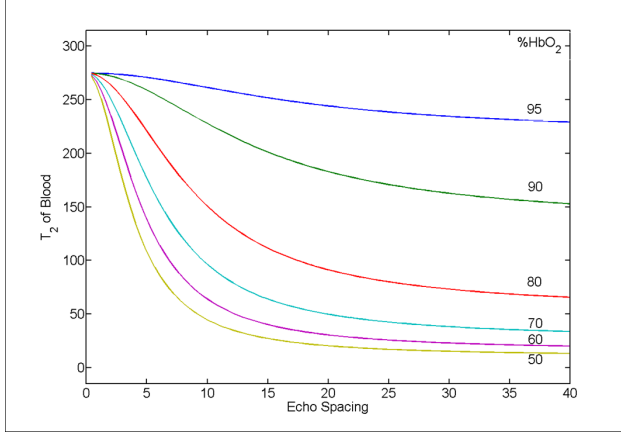
Figure 3.1: Effective blood T_2 as a function of oxygenation state and echo spacing in a rapidly refocused sequence. For typical venous oxygenation values, most of the change in effective T_2 occurs as the echo spacing is increased from 0 to 10 ms.

Equation 3.1 for various values of blood oxygenation and echo spacing.

To help identify optimal sequence timing parameters, Bloch equation simulations were performed to assess signal evolutions for arterial and venous blood during a TSE echo train with different echo spacings (Fig. 3.2). The variable relaxation rate of blood was modeled using the Luz-Meiboom model as described above to estimate blood T_2 during a spin echo train. Other simulation parameters were: $T_{1,\text{blood}} = 1900$ ms, $T_{2,\text{oxygenated blood}} = 275$ ms, $B_0 = 3.0$ T, echo train duration $= 600$ ms, arterial oxygenation $= 95\%$, venous oxygenation $= 60\%$, hematocrit $= 40\%$, P $= 36\%$, $\tau = 3$ ms, $\alpha = 0.7$ ppm, refocusing flip angle $= 180°$. The simulations show that as the spacing between refocusing pulses is increased, the maximum artery-vein contrast increases and furthermore, the maximum contrast occurs earlier in the echo train.

This work is performed at 3.0 T in order to maximize the amount of signal available. Additionally, higher field strength results in better venous suppression (see Eq. 3.1 and Fig. 3.3). The challenges of working at high field include increased B_0 inhomogeneity, susceptibility effects, and power deposition to the patient.

A volumetric TSE sequence with a long TE necessarily has an extremely long echo train
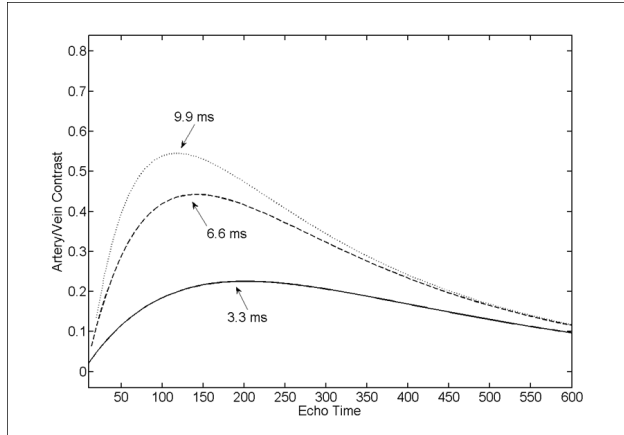
Figure 3.2: Artery-vein contrast as a function of echo time during a TSE sequence. Maximum contrast occurs earlier and peaks at a higher level when longer echo spacings are used between refocusing RF pulses. The echo spacing simulated by each curve is indicated by number and arrow.

duration (several hundred milliseconds). Simply increasing the echo spacing in this sequence would push the duration past the usable limit, as determined by arterial T_2, reducing image quality. A second option would be to adopt k-space segmentation methods, increasing scan times from around 5 minutes per volume to 10 minutes or more. Spiral readout gradients offer improved acquisition efficiency, and provide a path to achieving long echo spacings while maintaining reasonable scan times.

In Chapter 2, adequate fat suppression proved very difficult to achieve. Due to fat's rapid T_1 recovery and B_1 inhomogeneity, FIDs are generated off of each refocusing RF pulse no matter what fat suppression technique is performed at the beginning of the echo train. A crusher gradient dephases the signal from these FID components, allowing pure T_2 contrast to prevail in the sequence. For this reason – and in contrast to the work presented in Chapter 2 – the sequence used in this work includes crusher gradients in the through-plane (anterior-posterior) direction, which is justified since there is relatively little flow in that direction in the peripheral vasculature. This approach along with fat suppression prior to the excitation pulse yields very good fat suppression while maintaining insensitivity to flow in-plane (coronal). This is demonstrated in Fig. 3.4, with an early version of the spiral TSE
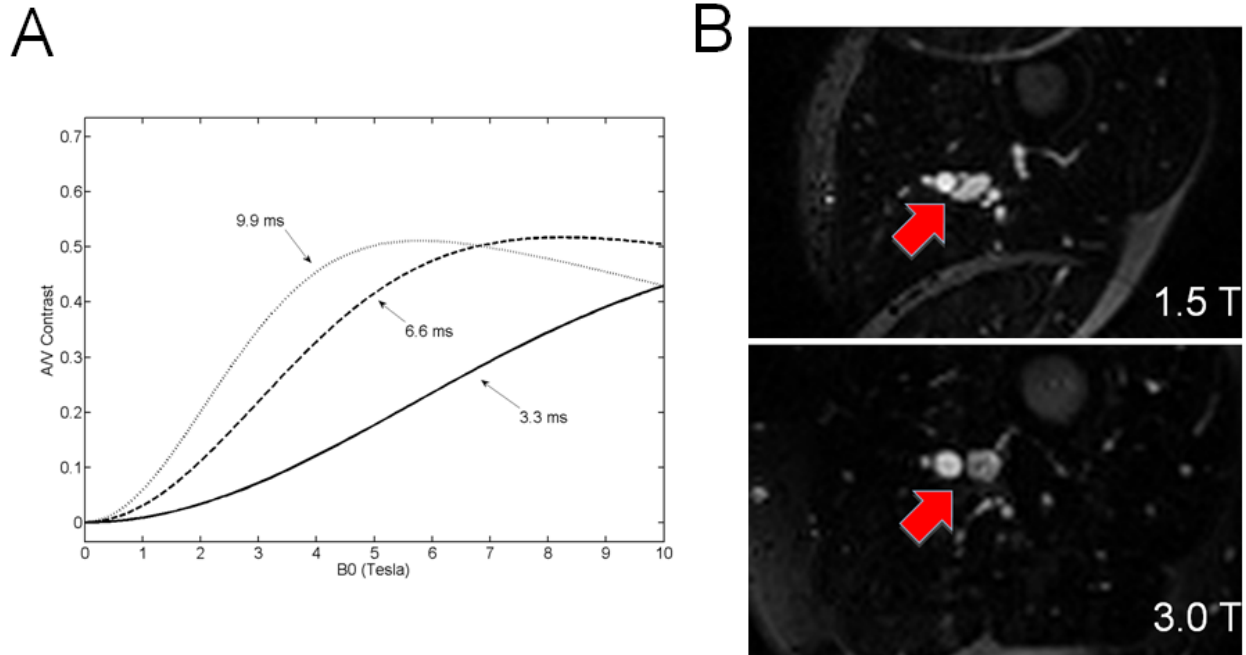
Figure 3.3: Artery/Vein contrast versus field strength. A) Bloch equation simulations of artery/vein contrast versus field strength for the 3 echo spacings presented in Fig. 3.2 with a TE of 150 ms. B) A contrast resolution improvement of $\approx 30\%$ is achieved by performing this work at 3.0 T, as demonstrated by these Cartesian rTSE images.

sequence. For this experiment, a volunteer was scanned with a spiral rTSE sequence (i.e. all gradient moment areas were zero between refocusing pulses) and with a sequence in which crusher gradients were applied in the anterior-posterior direction. A fat saturation pre-pulse was applied in both cases.

3.3   Sequence Design and Features

The sequence described in the following sections was built from and takes advantage of the product variable-flip-angle 3D TSE (SPACE) sequence from Siemens Medical Solutions. By integrating the spiral modifications directly into product code, many Siemens functions and utilities are immediately available. Furthermore, future transition from a research-only sequence to a product sequence is facilitated by this approach. Here, we differentiate between

Spiral rTSE (non-crushed)   Spiral TSE (crushed)
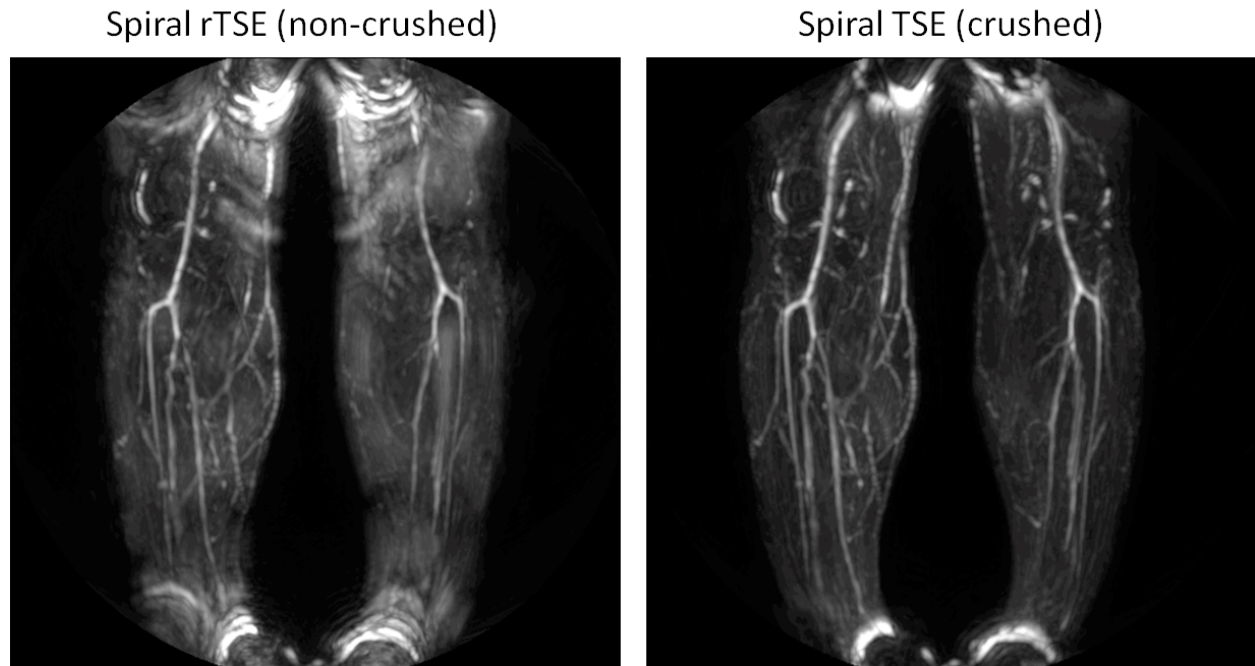
Figure 3.4: Despite the presence of fat saturation pre-pulses, fat appears in spiral rTSE images and degrades image quality (left). The addition of crusher gradients in the through-plane direction removes this spurious fat signal.

the "spiral TSE" sequence and the "spiral SPACE" sequence by whether or not variable flip angles are used. For MRA, and therefore in the majority of this dissertation, the spiral TSE sequence is used exclusively. However, one application of the spiral SPACE sequence is briefly discussed in Chapter 6.

Here, we will utilize a 3D stack-of-spirals trajectory. The trajectory consists of a parallel stack of 2D spiral disks, with phase encoding along the third dimension, such that the volume covered in k-space is a cylinder (Fig. 3.5). This will allow us to perform off-resonance correction by executing 2D off-resonance correction slice-by-slice in 3D [61].
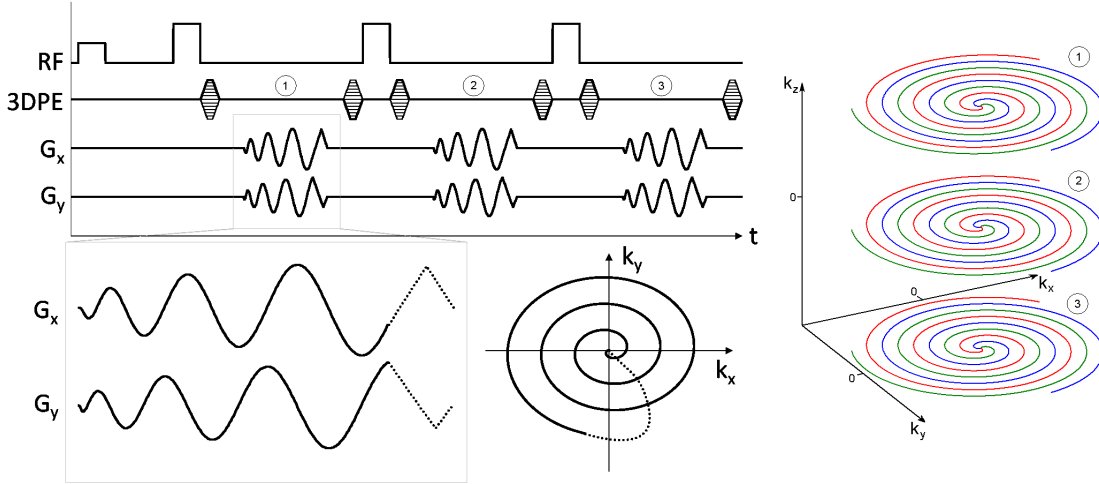
Figure 3.5: Spiral 3D TSE sequence diagram and resulting k-space trajectory. The same interleaf from each 3D phase encode is acquired in a single echo train. Partitions (3D phase encodes) are acquired linearly through the third k-space dimension and scrolled to achieve the desired TE. i.e. Echo train 1 acquires the red interleaf from partitions 1, 2, and 3, with partition 2 encoded as the center partition. After a wait time TR, Echo train 2 acquires the green interleaf, and so on. Within each echo spacing, the net area of the readout gradients is zero, but crusher gradients *are* applied on the 3DPE axis in order to dephase incidental signal (these gradients are not shown in this diagram for clarity).

3.3.1   Spiral Trajectory

In order to increase acquisition efficiency, the spiral readout is centered in the 180° inter-pulse period (see Fig. 3.5), which places the spin-echo at some radius in k-space, rather than at the center. This approach works reasonably well, but spiral-in/out trajectories, which center the gradient- and spin-echoes in k-space, were also implemented (Fig. 3.6). These trajectories immediately yielded a ≈25% improvement in image SNR; however, a potentially more useful result of using in/out trajectories is that, by averaging two in/out acquisitions whose trajectories are conjugates of one another, improved robustness to off-resonance is observed (see Chapter 4). The drawback to using this technique is that it requires twice the time to acquire the data, since averaging is required. Therefore, when averaging is already utilized (such as in the case of slab-selective excitation, which requires
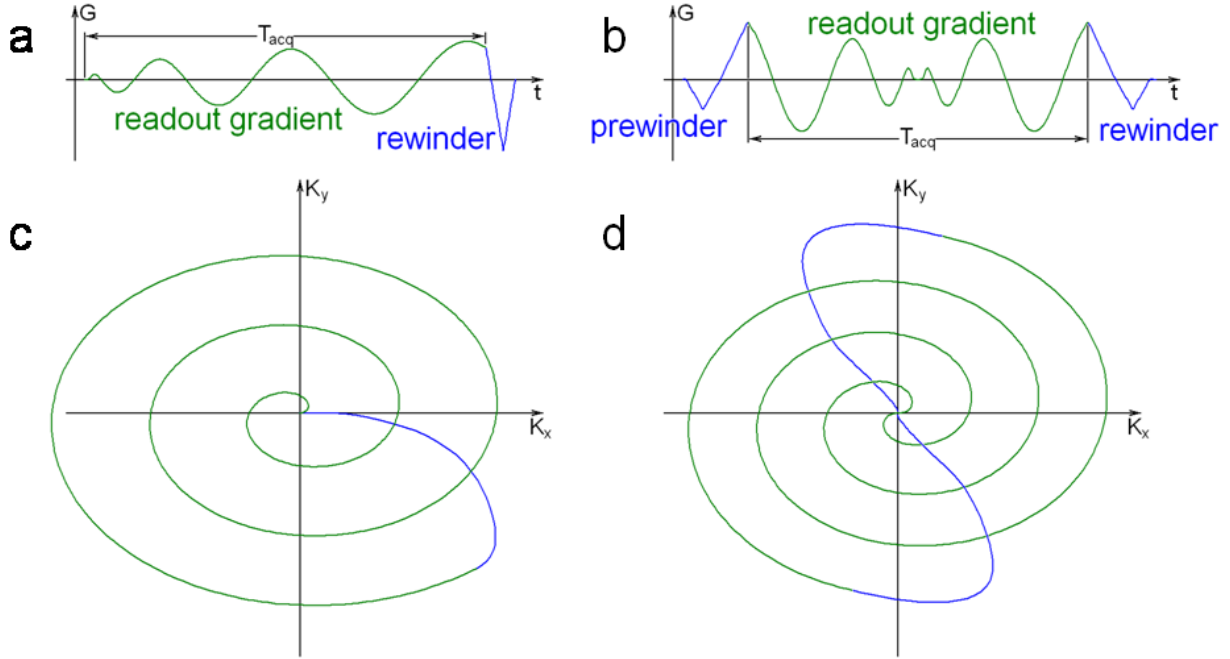
Figure 3.6: The well-known spiral-out (left) and the spiral-in/out trajectories (right). a) Spiral-out read gradient with rewinding lobe. b) Spiral-in/out read gradient with prewinding and rewinding lobes. c,d) K-space trajectories for the gradients in (a,b), respectively.

multiple averages in order to chop out extraneous FID signal), we use spiral-in/out readouts and only correct for linear off-resonance terms in reconstruction, otherwise, we use spiral-out gradients and perform semi-automatic off-resonance reconstruction using a Chebyshev polynomial approximation [62] (Fig. 3.7).

3.3.2 3D Reordering and Partial k-space

Each echo train in the sequence collects one interleaf from each partition in the acquisition volume in a linear fashion. Partial k-space coverage techniques have been used extensively in echo-train imaging [63], and they are prevalent in the TSE sequences used for flow-spoiled fresh-blood imaging. These techniques exploit the conjugate symmetry property of k-space and only acquire 50-90% of the data required to completely fill k-space. The missing data
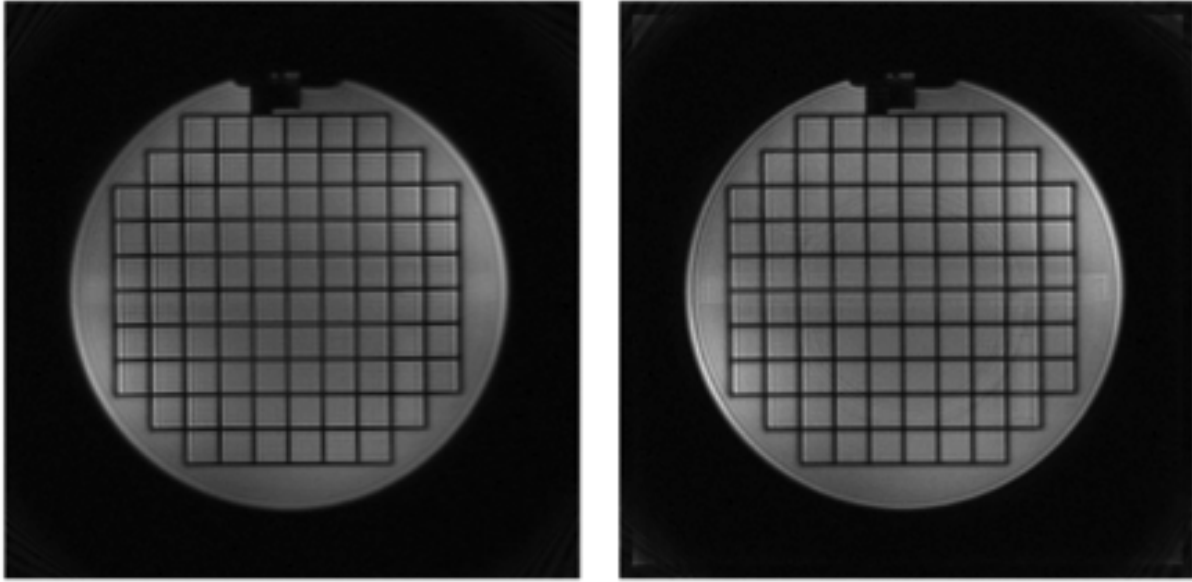
Figure 3.7: Central slice from a phantom stack-of-spirals image volume. Left: reconstructed with no correction. Right: reconstructed with a semi-automatic off-resonance correction technique applied to each 3D partition.

is then filled in before reconstruction takes place. Here, partial k-space coverage can be performed in the 3D phase-encoding direction to reduce the number of phase encodes that need to be performed, shortening echo train lengths (which are necessarily quite long). The sequence automatically performs a partial k-space acquisition depending on the effective echo time chosen by the user. For echo times typically used in this work, this results in partial k-space factors of about 0-30% (i.e. 70-100% of the data is acquired). Several partial k-space reconstructions for a dataset acquired with a large partial k-space factor of 66% are shown in Fig. 3.8. Here, missing data is filled in using naive zero-filling, and simple versions of the POCS (Projection onto Convex Sets), and homodyne algorithms [64]. Due to its simplicity and effectiveness, the homodyne partial-Fourier reconstruction algorithm (shown graphically in Fig. 3.9) was chosen for all reconstructions.
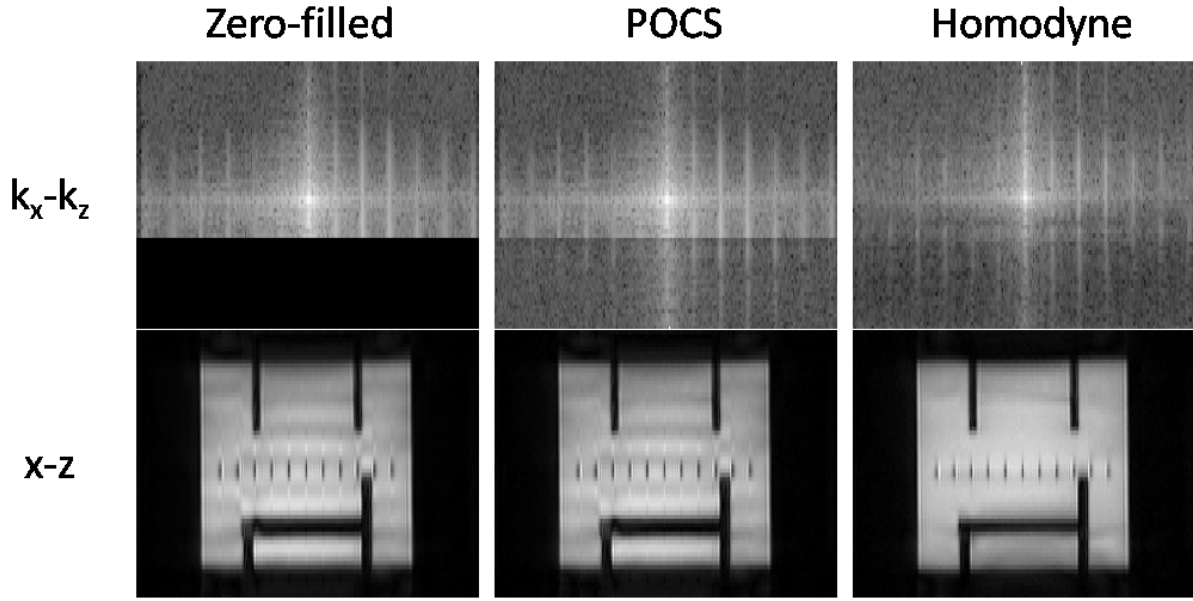
Figure 3.8: Partial k-space filling algorithms applied to 3D phantom data missing 33% of the required partitions. Missing data is filled in using either a zero-filled (i.e. nothing), POCS, or a homodyne algorithm. As the homodyne algorithm is a simple, direct method and shows the best results on this highly-undersampled dataset, it was chosen for all subsequent partial k-space reconstructions.
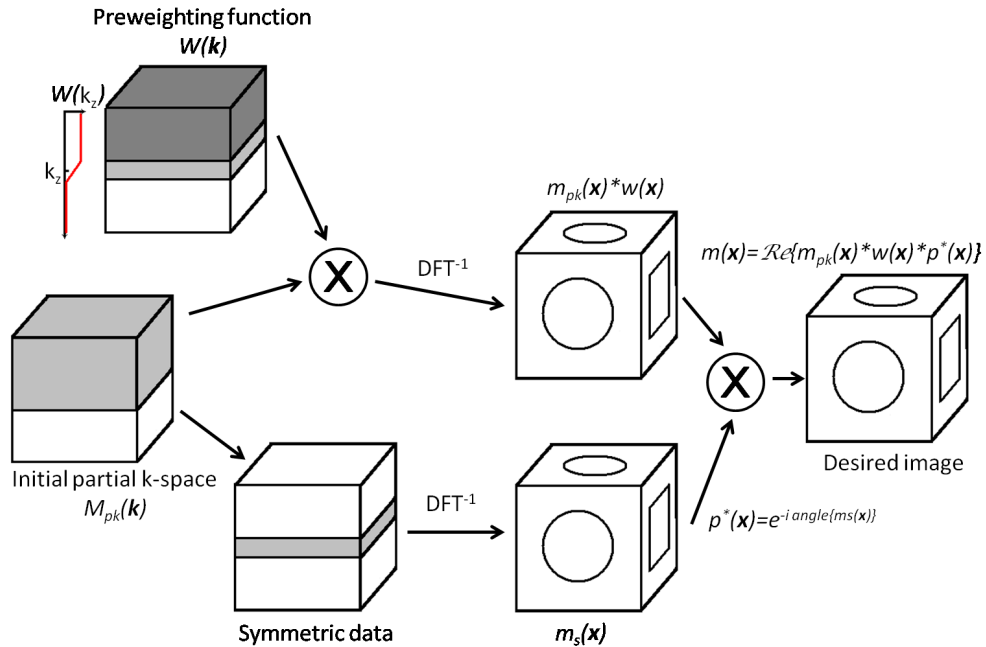
Figure 3.9: Graphical summary of the homodyne algorithm for 3D Cartesian imaging. For stack-of-spirals data, the DFT^{-1} operation is preceded by gridding and off-resonance correction, and for accelerated in-plane imaging, we replace DFT^{-1} with the SPIRiT reconstruction. Adapted from course notes by John Pauly.

3.3.3 Parallel Imaging

Parallel imaging permits larger undersampling factors, and thus a scan-time reduction and/or an increase in resolution. In the through-plane (Cartesian) direction of our stack-of-spirals trajectory, we use a simple GRAPPA-style k-space undersampling scheme and reconstruction. This allows greater through-plane resolution without k-space segmentation methods. The through-plane GRAPPA reconstruction was implemented and tested in the following manner: On a fully sampled 12-channel phantom dataset, every other line in kz was set to zero, leaving 24 fully-sampled partitions in the center of k-space, in order to simulate a 1.45X accelerated acquisition. Two reconstructions were tested: First, 1D GRAPPA was performed on an interleaf-by-interleaf basis prior to gridding. The calibration kernel was 5 x 1, and the first 400 samples of the fully-sampled partitions were used as the calibration region. The second reconstruction performed 3D GRAPPA on the data after gridding. The calibration kernel was 5 x 5 x 5, and the center 20 x 20 x 24 section of k-space was used as the calibration region. In Fig. 3.10, it is clear that the 3D GRAPPA reconstruction for 1D acceleration out-performs the 1D implementation. This is somewhat unsurprising, as more data is used to calibrate and fill in missing data. However, this comes at the expense of prolonged reconstruction times.

Variable-density spiral imaging was developed as a method to either reduce scan time or to achieve higher spatial resolution for a given scan time [65]. Variable-density trajectories adequately sample low spatial frequencies but undersample the high spatial frequencies. The sequence supports constant density and both linear- and dual-density spiral designs. A small amount of outer k-space undersampling using the linear variable density design is acceptable
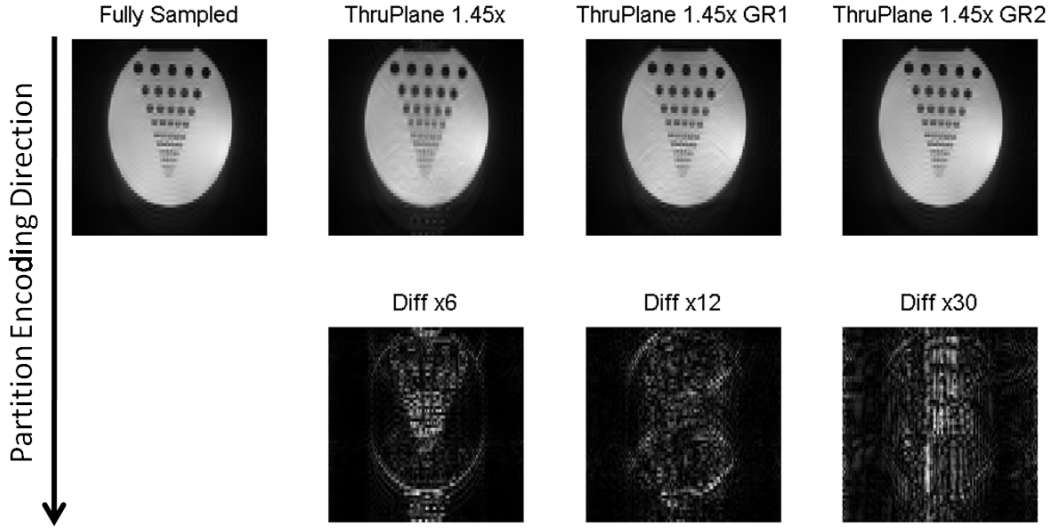
Figure 3.10: GRAPPA reconstructions. For stack-of-spirals acquisitions, two options are available to reconstruct missing partitions: First, missing spiral data may be estimated prior to gridding for each interleaf, using early data points to estimate the GRAPPA kernel (GR1). Second, the spiral data may first be gridded for each acquired partition, and 3D GRAPPA can then be performed (GR2). Here, an acceleration rate of 1.45 was simulated on fully-sampled phantom data and reconstructed with GR1 and GR2. The resulting errors when the GR2 reconstruction is used are much lower than those obtained with GR1.

without degrading image quality.

We have implemented in-plane (non-Cartesian) parallel imaging via the SPIRiT recon-struction algorithm available from Dr. Michael Lustig (`http://www.eecs.berkeley.edu/~mlustig/Software.html`) [66], which uses the fully-sampled center of k-space from a dual-density spiral k-space trajectory to calibrate the reconstruction. The SPIRiT reconstruction takes place slice-by-slice after a 1D Fourier transform in the through-plane direction (and followed by the semi-automatic off-resonance correction step, if specified). As mentioned previously, there are usually some missing partitions due to partial k-space acquisition. To address this, the SPIRiT reconstruction is applied within the homodyne algorithm (Fig. 3.9) by replacing the two $gridding - and - DFT^{-1}$ operations with SPIRiT reconstructions. In

Fig. 3.11, the combination of SPIRiT for the reconstruction of accelerated in-plane imaging along with the homodyne algorithm for partial k-space reconstructions is shown. For this experiment, dual-density spirals were prescribed with an acceleration factor of two, and the through-plane partial k-space factor was 0.75. A simple gridding and Fourier-transform reconstruction of the data is compared to a SPIRiT reconstruction with missing partitions filled in via zerofilling, and to a reconstruction in which SPIRiT was incorporated within the homodyne algorithm.

In general for MRA, we set our TE based on maximal artery-vein contrast and the sequence calculates the partial Fourier factor necessary for proper k_z reordering (as mentioned previously, the partial Fourier factor is usually between 70-100%, depending on echo spacing and TE). In the abdominal and thigh stations, relatively large resolutions of around 1.2 mm^2 require no acceleration. In the calf station, the resolution requirement is a bit higher, and here modest in-plane undersampling factors of 2-4 are used to keep scan times reasonably short.

3.3.4   Extravascular Fluid Suppression

An inversion pulse can be applied before excitation to null long-T_2 extracellular fluid (synovial fluid and edema) signal based on its unique T_1. This should be evaluated on a case-by-case basis, however, since the application of an inversion pulse will have a deleterious effect on other signals as well.
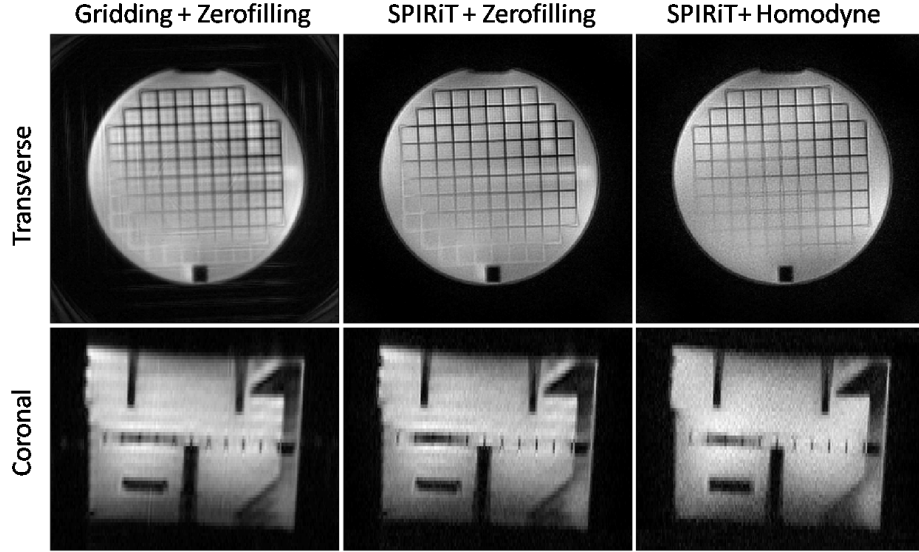
Figure 3.11: Parallel imaging to improve in-plane imaging with the stack-of-spirals trajectory. On the left, moderate in-plane undersampling improves resolution by 30% (compared to a constant-density acquisition), but causes spiral undersampling artifacts. Zerofilling of missing partitions results in through-plane artifacts. In the middle, SPIRiT removes spiral artifacts, but the through-plane artifacts remain. On the right, the incorporation of SPIRiT within the homodyne algorithm corrects both in-plane and through-plane artifacts.

3.4 *In-vivo* experiments

All scans were performed on a Siemens 3.0 T Trio scanner (Siemens Medical Solutions) with peripheral MRA coils placed anteriorly and laterally and a spine coil placed posteriorly. Subjects were scanned in the supine position, with the stack-of-spirals volume oriented coronally (i.e., the through-plane direction was anterior-posterior). The protocol was approved by the Human Investigation Committee at the University of Virginia Health System and all participants signed informed consent.

Two male volunteers were scanned with variations of the spiral TSE sequence in order to demonstrate its artery-vein contrast properties. First, a constant echo spacing of 10 ms was used with the TE varying between 55 and 325 ms. Number of spiral-out interleaves =

25 to achieve an in-plane resolution of 1.2 mm^2 over a 400 mm^2 FOV, TR = 3 s, refocusing flip angle = 180°, with all excitation and refocusing pulses non-selective. Through-plane resolution was 2 mm with 64 3D phase encodes. Both chemical fat saturation as well as a STIR pulse were used for fat suppression. No parallel-imaging acceleration was used for these scans. The total echo train duration varied depending on TE, but typically fell in a range between 300 - 600 ms. Total scan time was 1.4 minutes per image volume.

Next, echo spacing was varied between 6.2 and 11.8 ms with a constant TE of 165 ms. For this experiment, increasing echo spacing in the sequence automatically results in longer readout events, so the total number of spiral interleaves was adjusted in order to maintain a constant 1.2 mm^2 in-plane resolution.

Additionally, one volunteer was scanned with a Cartesian version of the sequence with echo spacing = 3.8 ms for comparison. The optimal TE predicted for this echo spacing is around 230 ms. Due to sequence constraints, the Cartesian sequence was acquired with 1.5 mm^3 isotropic resolution and TR = 4720 ms due to SAR limits. The resulting scan time was 7.5 minutes.

For each image set, 3 points of interest in the femoral artery and vein were recorded in order to determine artery-vein contrast in the same manner as described in Section 2.3.1.

Two additional scans were performed. First, the utility of a FLAIR pulse to remove synovial fluid was demonstrated by adding a non-selective IR pulse with TI 2500 ms (TR was increased to 10 s). Second, a high-resolution scan of the calf of one volunteer was performed by increasing the in-plane parallel-imaging acceleration factor to a modest value of 2, resulting in an in-plane resolution of 1.0 mm^2.

3.5   Results

Figure 3.12 shows that, for a 10 ms echo spacing in normal volunteers, artery-vein contrast peaks around 100 ms. Furthermore, any TE over approximately 80 ms is very effective at suppressing background muscle. Early TEs are advantageous in that they result in more signal being deposited near the center of k-space before T_2 decay removes available magnetization. The reduction in SNR due to a late TE is especially apparent in the TE $=$ 325 ms image.

As predicted by the Luz-Meiboom model, larger echo spacings within the echo train result in better venous suppression (Fig. 3.13). By moving from an echo spacing of 3.8 ms in a Cartesian sequence to 10 ms using a spiral sequence, the CNR between arteries and veins is improved by 235% (Fig. 3.14). Furthermore, despite the drastically reduced scan time, it is clear in Figure 3.14 that the increased efficiency of spiral readout gradients results in better in-plane resolution over its Cartesian counterpart (1.2 mm^2 vs 1.5 mm^2).

Figure 3.15 demonstrates that synovial fluid in the knee can be effectively removed with the application of an inversion pulse with TI 2500 ms (TR must be increased accordingly). However, this dramatically increases scan time and has a deleterious effect on other signals.

As a final example, Figure 3.16 shows a MIP of the calf station of a volunteer, displaying excellent artery-muscle and artery-vein contrast.
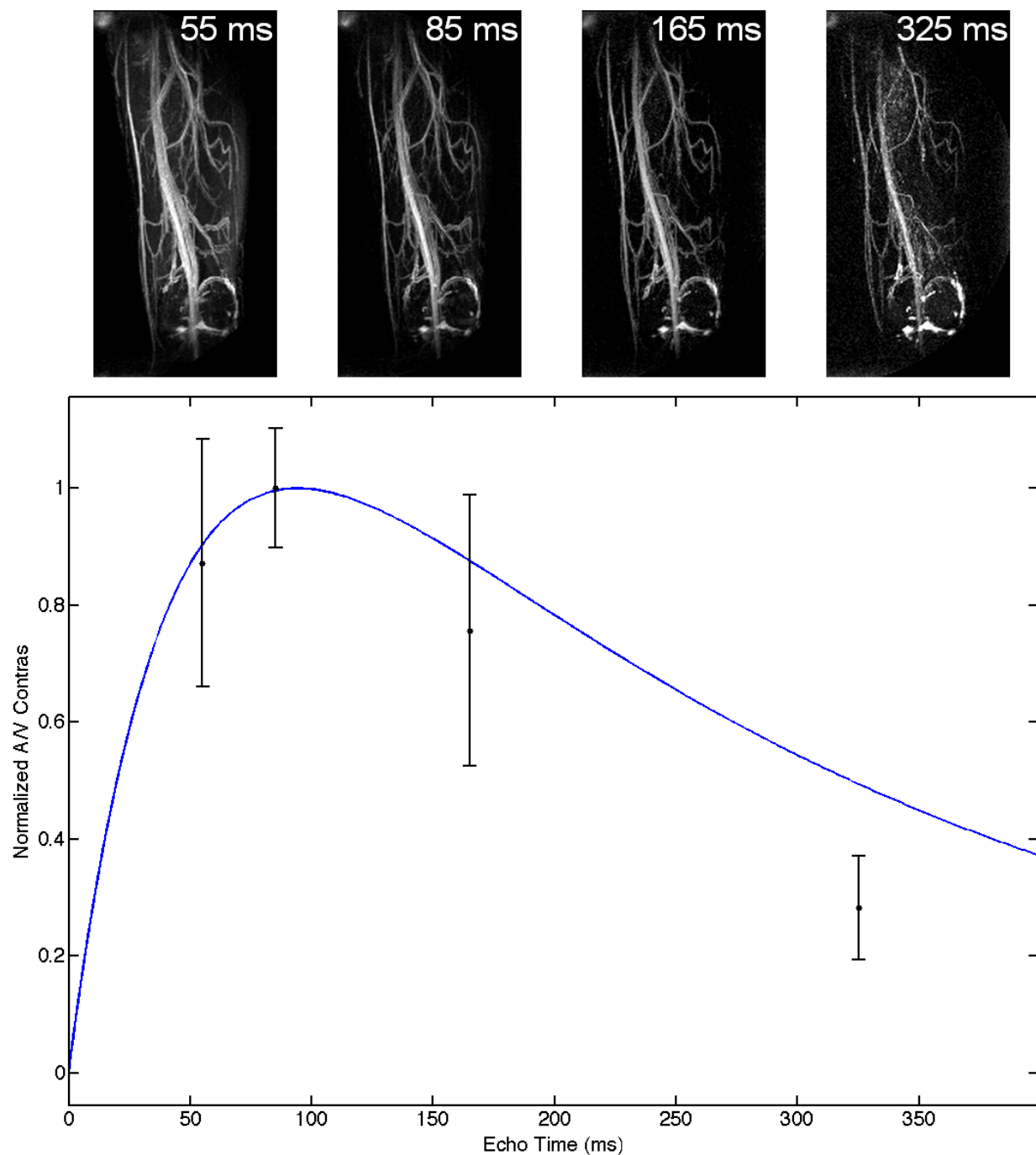
Figure 3.12: Top: MIP images of a normal volunteer's thigh at various TEs. Bottom: Plot of measured and predicted artery-vein contrast. Artery-vein contrast is maximized at TE ≈ 100 ms and follows the general shape predicted by Bloch equation simulations (see Fig. 3.2) of artery-vein contrast evolution (blue line). Muscle signal is removed with any choice of TE > 80 ms.
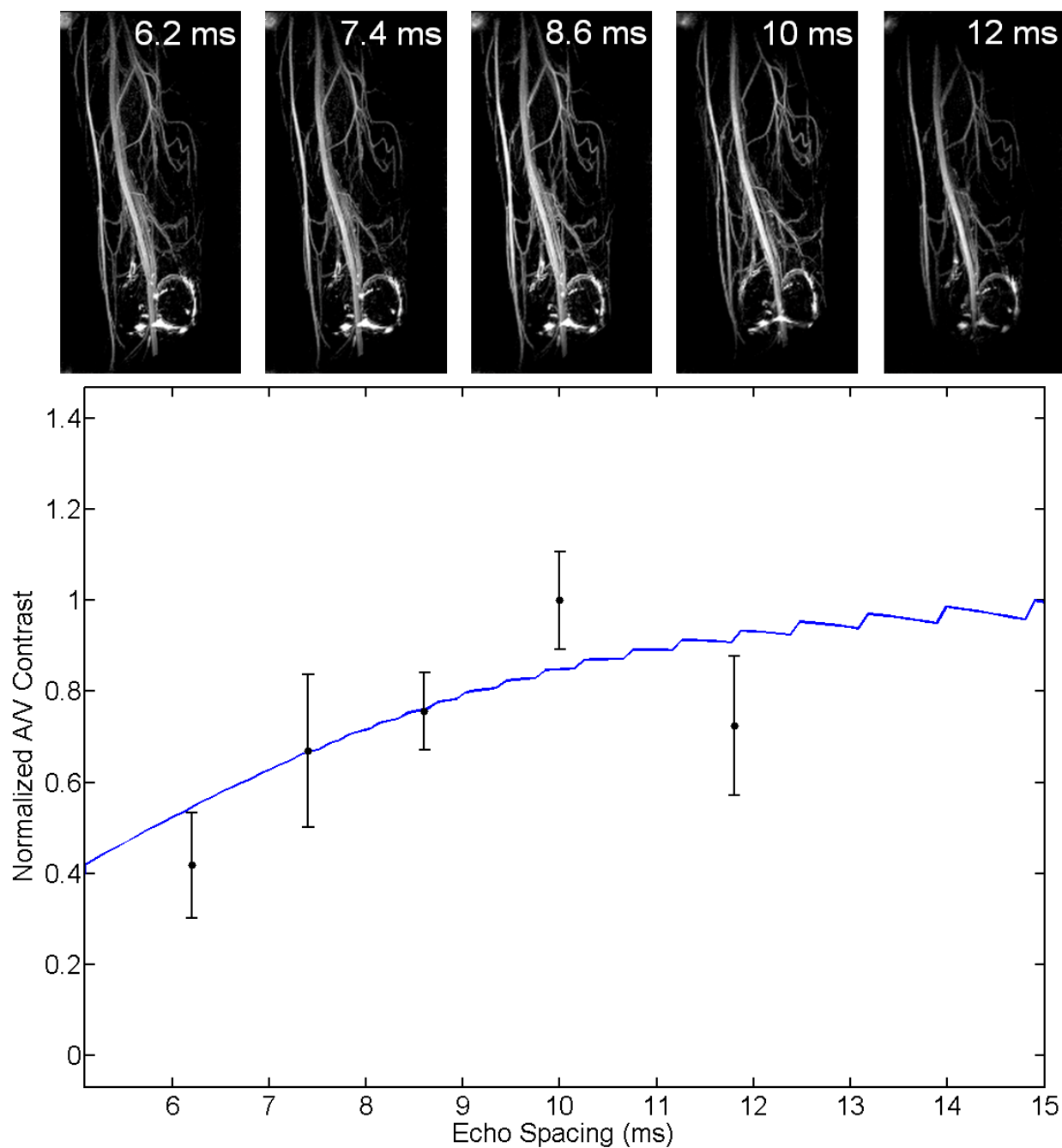
Figure 3.13: Top: MIP images of a normal volunteer's thigh with various echo spacings. Bottom: Plot of measured and predicted artery-vein contrast. Artery-vein contrast improves as echo spacings are lengthened; however, in this implementation, very large spacings result in image blurring due to off-resonance accrual since the readout duration is fixed to fill the available time. The blue line represents Bloch equation simulations of artery-vein contrast at various echo spacings.
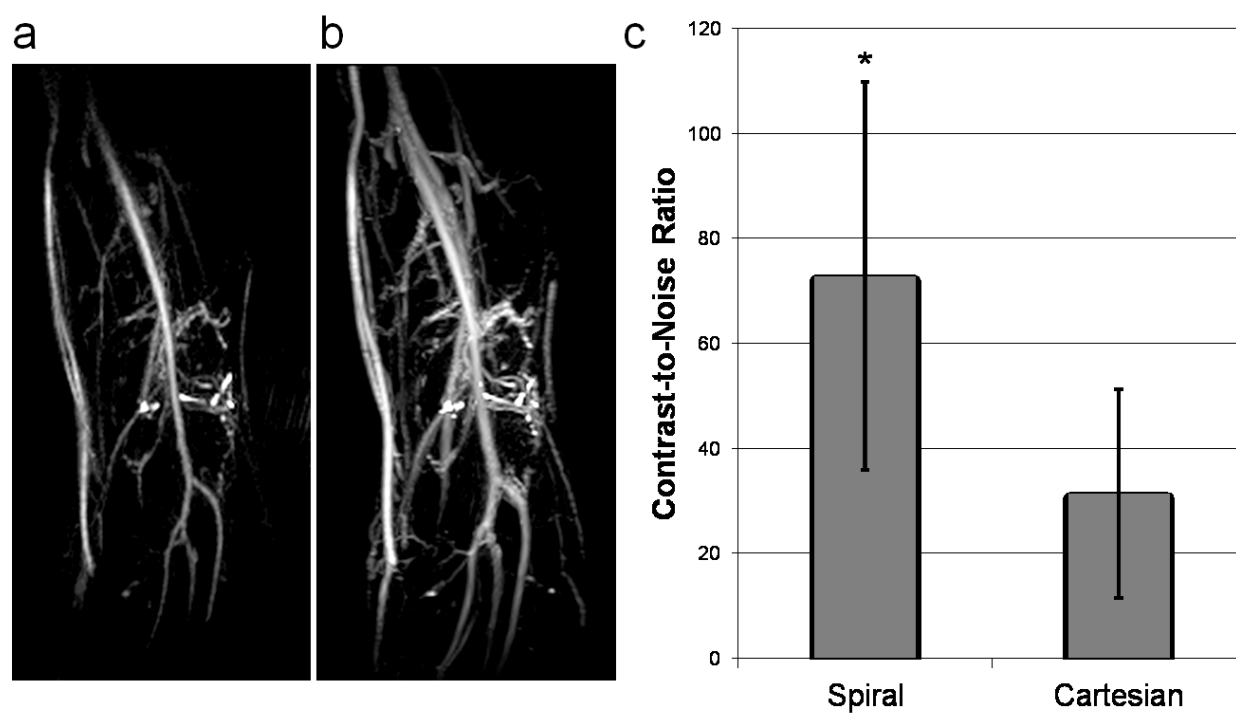
Figure 3.14: Spiral verus Cartesian TSE. a) Spiral TSE; echo spacing = 10 ms. b) Cartesian TSE; echo spacing = 3.8 ms. Confounding venous signal is observed in the Cartesian image and is nearly removed in the spiral image. Additionally, use of the spiral sequence results in better in-plane resolution. c) Quantification of artery/vein CNR based on three ROIs placed in each of the femoral artery and vein. * $p < 0.05$.
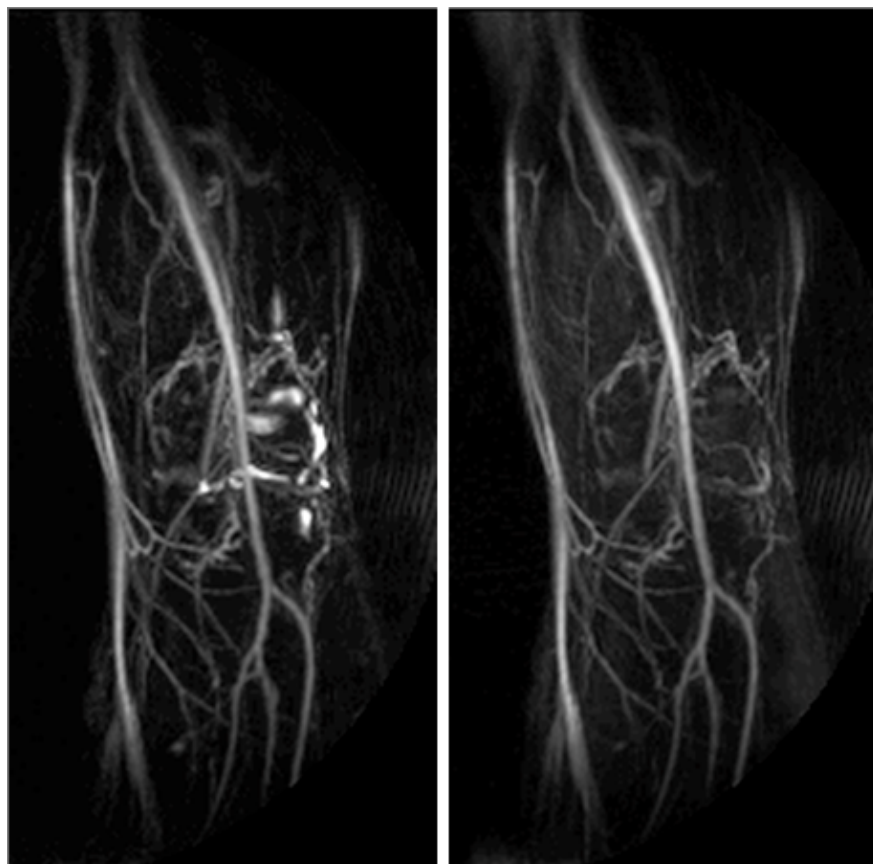
Figure 3.15: Fluid suppression in spiral MRA. Left: No IR prep. Right: IR prep (FLAIR). Synovial fluid in the knee may be suppressed with the addition of an appropriately-timed IR pulse, at the expense of signal and contrast.

3.6   Discussion

In the spiral TSE sequence, signal from flow is maintained by ensuring the net area of the in-plane spiral gradients is zero within each echo spacing. In contrast to flow-spoiled methods which also use the TSE sequence and must be tailored to each patient and each station, contrast between arteries and surrounding tissues is generated here by T_2 differences, and in particular, artery-vein contrast is obtained without the use of gated, subtracted acquisitions but rather by manipulating the effective T_2 of venous blood through extended echo spacings. This is a novel contrast generation method for peripheral angiography in the context of TSE sequences.

Because FIA is sensitive to changes in blood oxygenation, it is expected that the optimal
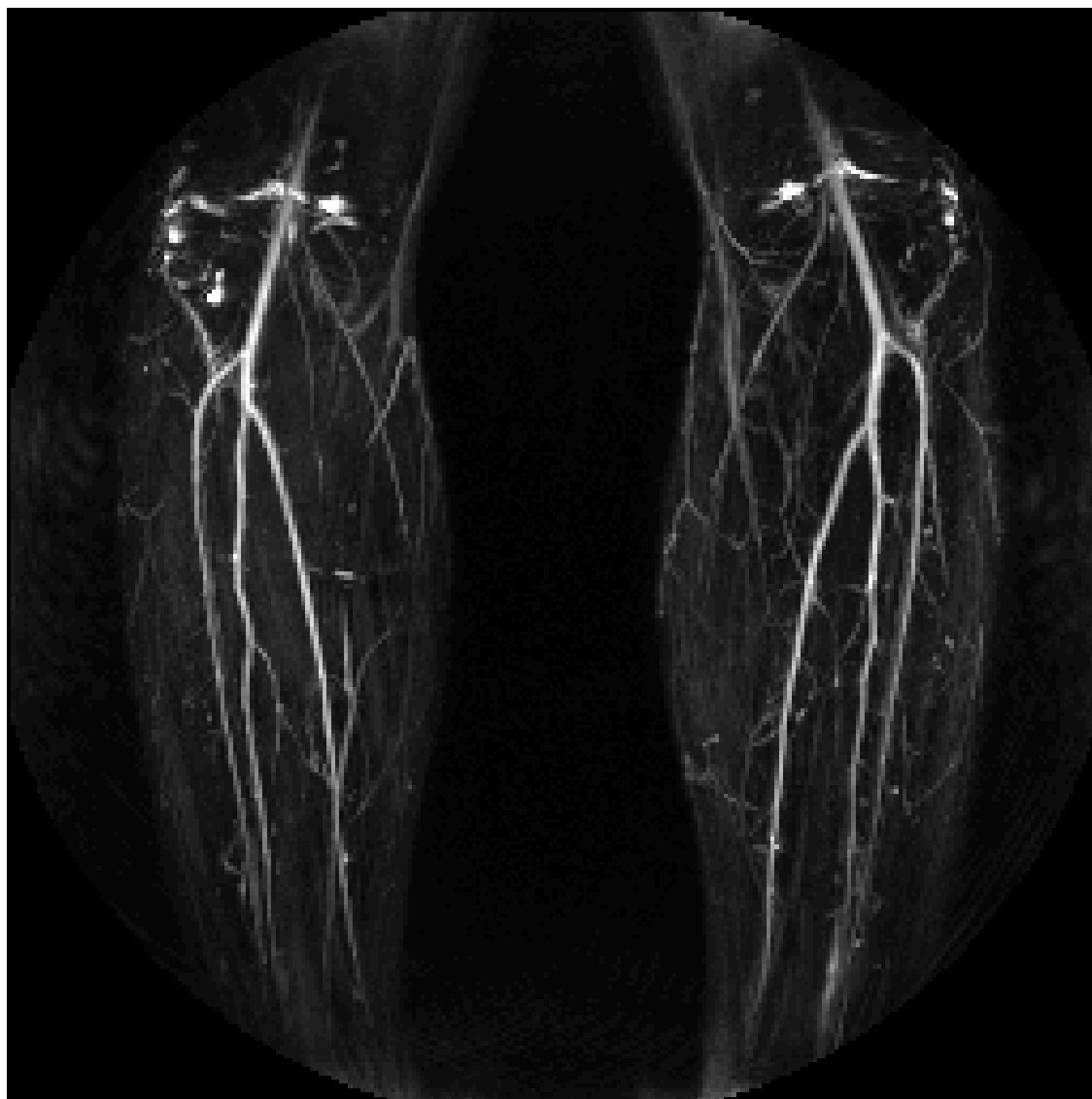
Figure 3.16: Calf station in a normal volunteer. Synovial fluid is observed in the knee where a FLAIR pulse was not applied.
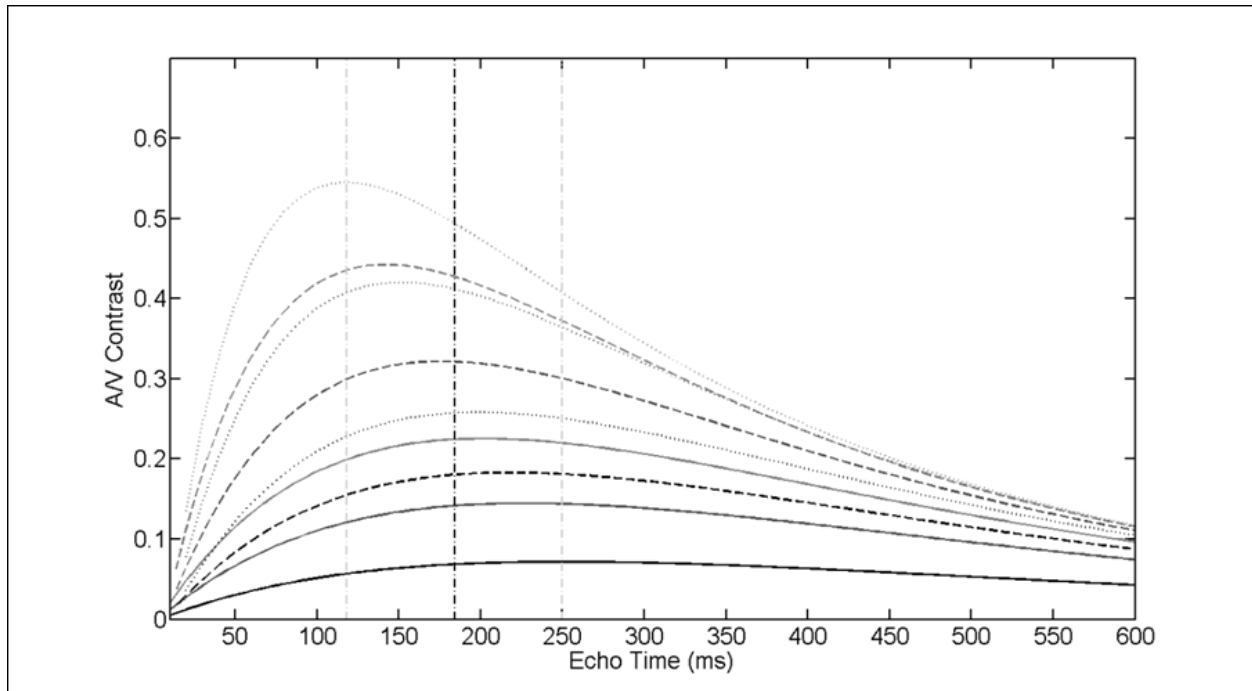
Figure 3.17: Artery-vein contrast plotted with a wide range of possible venous T_2 values and echo spacings. A wide range of optimal TEs occurs for the various combinations, ranging from 120 ms to 250 ms.

TE for artery-vein contrast will need to be adjusted to an earlier time in the echo train for clinical imaging. In light of this and by studying Figure 3.17, a potential disadvantage of long echo spacings is apparent: longer echo spacings result in more "peaky" contrast curves. For patients, who present with a wide range of venous oxygenation states, missing the optimal TE becomes easier and more costly in terms of contrast generation. In this case, pre-scans may be necessary to determine optimal sequence parameters based on blood oxygenation levels.

Spiral readouts are an appropriate choice for this application because they are naturally resistant to artifacts due to flow and motion; making them excellent candidates for a sequence wherein blood motion must not impact image formation. Simply increasing the echo spacing in a Cartesian TSE sequence would push echo train lengths to untenable dura-

tions, necessitating the use of segmented acquisitions, and would therefore have a negative impact on scan time. The efficiency of spirals means that extended echo spacings can be achieved while maintaining reasonable scan times. In fact, scan times using the 3D spiral TSE sequence are substantially shorter for a given resolution than when using its Cartesian counterpart.

A second advantage related to the efficiency of spiral readouts for this sequence is reduced power deposition to the subject. In a Cartesian sequence, the design of the k-space reordering method along with the short echo spacings dictates several hundred 180° refocusing pulses be played out in a single echo train, or else k-space segmentation methods must be employed. It is very common to either have to reduce the refocusing flip angle or extend TR in order to satisfy SAR limits when using long echo train duration TSE sequences. Because the spiral sequence traverses k-space differently – and with much larger echo spacings – the number of RF pulses played out during a single echo train is much lower, and SAR limits are rarely encountered.

A few words must be said regarding k-space ordering when using this sequence. First, remembering that the through-plane direction is traversed *within* an echo train as the 3D phase encoding direction, aberrant signal evolutions caused by improper k-space reordering will have the greatest impact in this direction. For angiography, where we desire strong T_2 weighting, long TEs allow the use of a linear reordering scheme, which is conceptually and physically the simplest option available. For other applications, however, where an early TE is desired for SNR or contrast properties, a centric reordering scheme may be used. In this case, it is important to bypass the transition region at the beginning of the echo train by skipping several echoes before data acquisition begins. In-plane, we have also

explored different interleaf reordering schemes. For unsegmented acquisitions such as those presented in this Chapter, the method presented here, in which the same interleaf is acquired repeatedly for each partition within an echo train, works well. However, we have observed that for segmented approaches, linearly increasing the interleaf number throughout the echo train yields better results than simply acquiring the same interleaf from each partition. The mechanism behind this observation remains unknown and requires further study.

In conclusion, the spiral TSE sequence is capable of utilizing FIA to generate 3D angiograms of the periphery quickly and without the use of contrast agents. The sequence is faster, has less SAR, and results in better contrast than its Cartesian counterpart.

Chapter 4

Spiral In/Out

The most commonly encountered spiral trajectories are "spiral-out". That is, the trajectory begins at the origin of k-space and moves outward along a spiral. These trajectories may be time-reversed ("spiral-in") in order to provide a measure of T_2^*-sensitivity to the sequence [67]. If a traditional spiral-out readout is added after the spiral-in readout, a "spiral-in/out" trajectory is formed. Although this trajectory was first proposed for efficient sampling of spin-echoes for abdominal imaging [68], a version of it has gained popularity in fMRI [69], where its SNR, speed, and resistance to flow artifacts make it an attractive alternative to rectilinear EPI methods.

4.1   Introduction

Spiral k-space trajectories have many advantages over traditional rectilinear acquisitions, including better acquisition efficiencies and a natural resistance to artifacts in the presence of flow and motion [70]. The major hurdle to wide-spread adoption of spiral trajectories has been their poor off-resonance performance [22]. The blurring and distortion in spiral

images in the presence of system non-idealities led to the two-pronged strategy of mitigation and correction in spiral imaging. Artifacts are minimized by splitting the acquisition into multiple short interleaves, such that an undue amount of undesirable phase does not accrue in a single interleaf. Secondly, much effort has been expended to correct for off-resonance effects in image reconstruction algorithms. These techniques vary in complexity and computational cost, from a relatively simple center frequency correction and first-order trajectory warping method based on a least-squares fit to an acquired field-map [71], to time- [72] and frequency-segmented approaches [73], to automatic [74, 75] and semi-automatic [62] methods which demodulate the image at multiple frequencies in order to build a composite image free of blurring. Many of these algorithms have become large, requiring several seconds to reconstruct a single image.

Additionally, off-resonance may be caused by other system imperfections besides B_0 inhomogeneity. Particularly at lower field strengths and for off-center slices, concomitant fields generated by normal gradient operation can cause noticeable blur in spiral images [76]. With some exceptions [76–78], the blur due to concomitant fields is largely ignored in the spiral literature, as it requires a more complex model to appropriately address deblurring.

For spiral imaging, the amount of undesired phase accrued between when the center of k-space is sampled and when the edge of k-space is sampled determines the severity of the well-known spiral blur. Given a desired resolution, spiral-out and spiral-in/out trajectories require readout lengths of nearly the same duration (within a few percent due to differing amounts of time spent near the center of k-space where the k-space velocity is small). For a given readout length then, a spiral-in/out trajectory requires about half as long to move from the edge of k-space to the center compared to a spiral-out trajectory. It follows that for a

fixed readout length and identical TE, spiral-in/out trajectories will have better off-resonance performance than their traditional spiral-out counterparts.

In this chapter, we take a closer look at spiral-in/out trajectories and address one method by which blurring due to off-resonance can be avoided through their use. The specific origin of off-resonance (B_0 or concomitant fields) is unimportant, and we will show that using a redundant spiral-in/out sampling scheme naturally removes the most severe off-resonance image artifacts during image acquisition, allowing for fast and simple correction methods in the image reconstruction step.

4.2 Theory

Conceptually, spiral-in/out trajectories can be implemented in one of two ways. In the first method, termed here the "non-redundant" scheme, each spiral-out arm fills in the conjugate k-space location of the spiral-in arm. This trajectory does result in less blur due to off-resonance; however, severe artifacts occur in multi-shot imaging when there is either an amplitude or phase mismatch in the data acquired with the spiral-in and spiral-out portions of the spiral-in/out trajectory. The second method, which we will call the "redundant" scheme, acquires each interleaf twice; once in each direction through k-space and subsequently averages the data.

Figure 3.6b shows the readout gradient for a spiral-in/out trajectory. In Fig. 4.1, the non-redundant and redundant in/out trajectories are shown. The redundant trajectory essentially consists of two non-redundant trajectories with the second acquisition rotated 180° in k-space. Thus, for a given resolution and field-of-view, the redundant scheme requires twice the
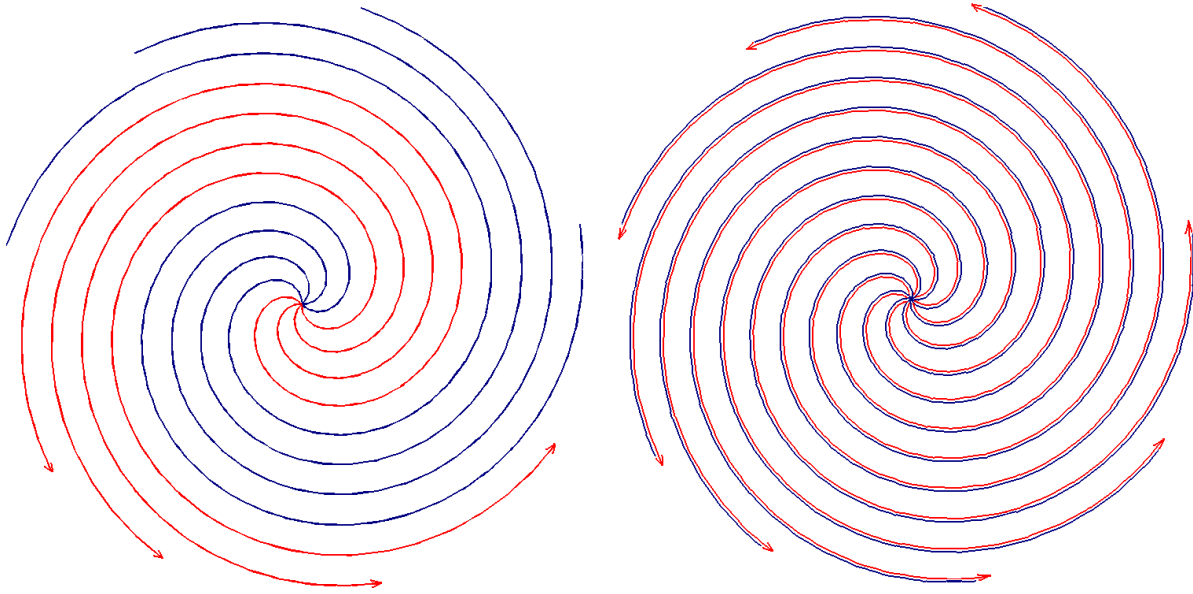
Figure 4.1: Non-redundant spiral-in/out (left) and redundant spiral-in/out (right). Each of these trajectories is spiral-in/out, but for ease of visualization, blue lines represent spiral-in arms of the trajectories; red represents spiral-out.

number of excitations as its non-redundant counterpart. However, despite this prolongation

of scan time, we will show in the next subsections that the redundant trajectory possesses

key properties to make it a very attractive trajectory for spiral imaging.

4.2.1   Redundant trajectory response to system non-idealities

4.2.1.1 B_0 off-resonance

We begin with simulated point-spread-functions (PSFs) for a spiral-out, non-redundant

in/out, and redundant in/out trajectories with and without off-resonance (Fig. 4.2). PSFs

were simulated by performing a gridding-and-FFT reconstruction on a matrix of ones. Off-

resonance was added by linearly increasing the phase of the simulated data. For all simula-

tions in this section, number of interleaves = 14 (28 for redundant in/out trajectory), field

of view = 300 mm, total readout duration 10 ms. Moderate off-resonance with spiral-out

trajectories causes a well-known broadening of the main PSF lobe due to undesired phase accrual during the spiral readout, while in non-redundant spiral-in/out, little broadening of the PSF main lobe is observed. However, strong rings are caused by the phase mismatch (due to off-resonance) between the spiral-in and spiral-out arms. These rings' locations are dependent on the number of interleaves being used, and they occur further away from the main lobe with fewer interleaves. Redundant scanning removes these rings through phase cancellation and leaves the narrow main lobe, resulting in an excellent PSF for spiral imaging.

To understand the origin of this effect, we will examine the signal equation of a spiral-in/out trajectory in the presence of B_0 inhomogeneity . Ignoring relaxation, the classic demodulated signal equation in MRI is:

$$s(t) = \int m(\mathbf{r})e^{-j2\pi k(t)\mathbf{r}}e^{-j\omega(\mathbf{r})\tau(t)}d\mathbf{r} \tag{4.1}$$

where $m(\mathbf{r})$ is the signal, $k(t)$ the k-space trajectory, and $\omega(\mathbf{r})$ the off-resonance. For the time being, we will set the off-resonance phase-accrual time parameter $\tau(t) = t$ since phase accrues proportionally to time for B_0 off-resonance. For phase accrual due to concomitant fields, $\tau(t)$ is more complex, and we will address the concomitant field case in the next subsection.

It can be shown (Section 4.6) that the signal resulting from the averaging of the data from a redundant spiral-in/out trajectory is:

$$s(t) = \int m(\mathbf{r})e^{-j2\pi k(t)\mathbf{r}}[\cos \omega(\mathbf{r})t]d\mathbf{r} \tag{4.2}$$
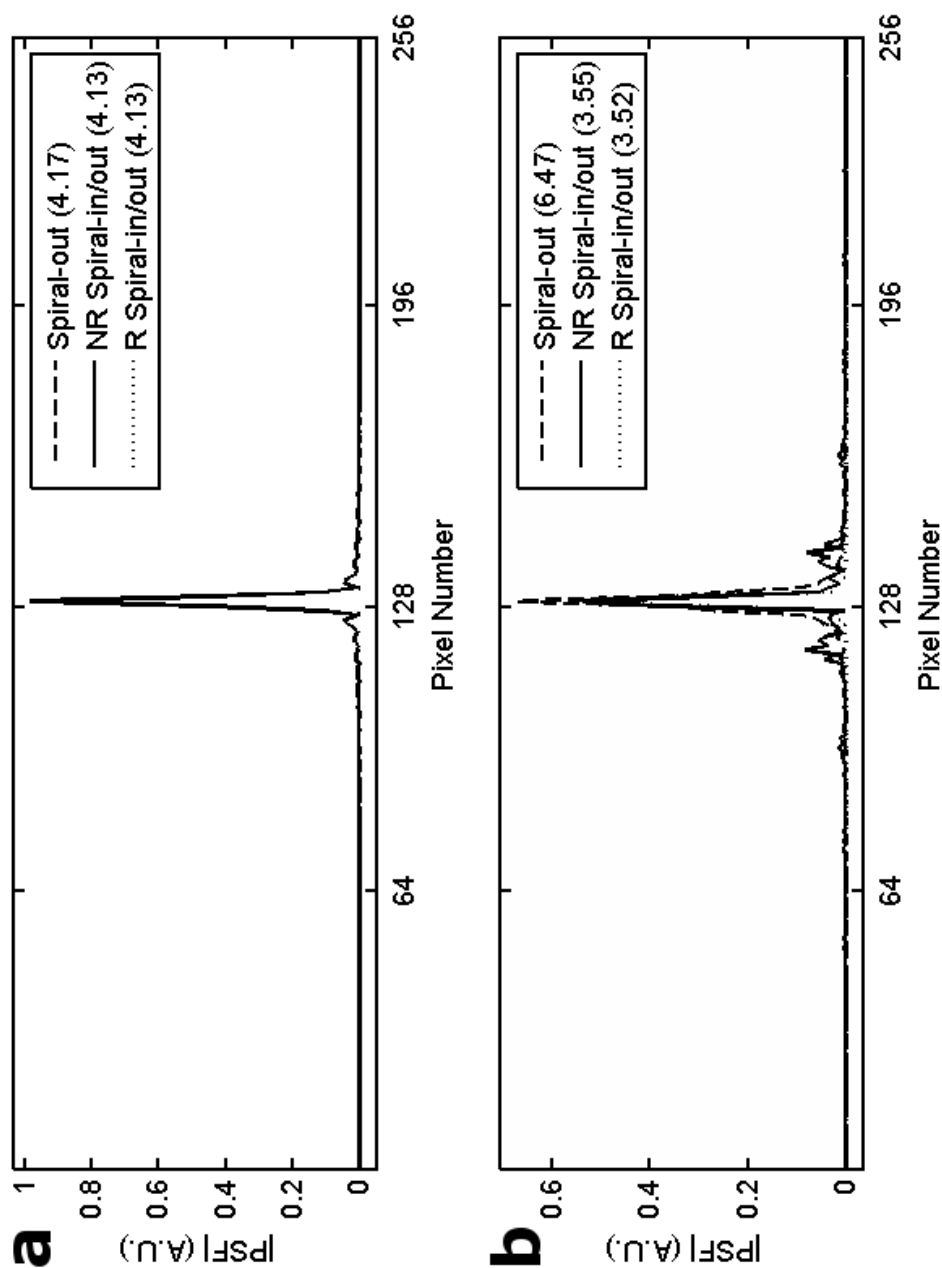
Figure 4.2: PSFs of spiral trajectories. Center line of 2D PSF shown for each trajectory variation. Numbers in parentheses are FWTM values for each trajectory. a) On-resonance; PSFs are indistinguishable. b) 50 Hz off-resonance (0.5 cycles of phase accrued by the end of the readout); Spiral-out trajectory shows expected broadening. Non-redundant spiral-in/out displays narrow main lobe along with very pronounced side lobe "rings". Redundant spiral-in/out removes these rings, leaving the narrow main lobe.

For small-to-moderate off-resonance values, Eq. 4.2 shows that the signal experiences a relatively benign cosine amplitude modulation of the signal rather than the more serious phase modulation that arises with spiral-out trajectories in the presence of off-resonance. Figure 4.3a shows simulated normalized modulation transfer functions (MTFs) for various amounts phase accumulated by the end of the readout (corresponding to the off-resonance-time product in Eq. 4.2) for the redundant spiral-in/out trajectory. There are two regimes under which the shape of the MTF may fall. In the first regime, the number of accumulated cycles is small, either because there is not much off-resonance present, or because the readout length is short. In this regime, the cosine modulation never reaches its first zero point during the readout, so the signal experiences a windowing function which only slightly attenuates high-frequency components, which results in a slight blurring. This residual blurring is much less than the blurring associated with a comparable spiral-out scan. In the second regime, when the value of the off-resonance-time product is high, the cosine modulation will begin nulling important frequencies as a function of k-space radius, resulting in image artifacts. This figure indicates the redundant spiral-in/out method will work well as long as the number of cycles of phase remains less than 0.5. For a 10 ms readout, this is 50 Hz. This amount of off-resonance is easily achieved during normal operation of clinical-strength scanners, so we anticipate first-order correction should be performed on the data/trajectories prior to gridding in order to quickly correct gross off-resonance.

4.2.1.2   Concomitant gradient effects

Returning to the case where phase accrual is due to concomitant field effects, it can be shown that $\omega_c(\mathbf{r})$ is a complex function of the imaging gradients and spatial coordinates of the slice,
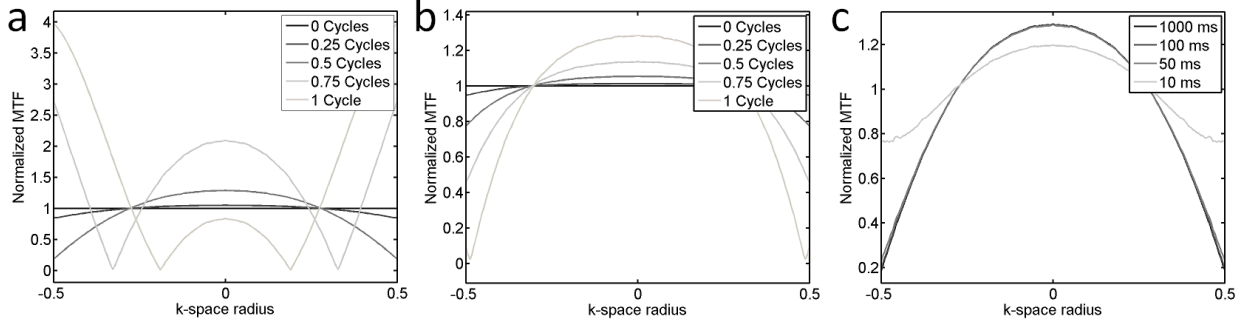
Figure 4.3: Normalized MTFs of spiral in/out trajectories. MTFs are normalized to on-resonance (0 cycles) case. a) Center-frequency offset. Until 0.5 cycles of phase are accrued, the cosine function never reaches its first zero, resulting in a relatively benign amplitude modulation in k-space; however, important frequencies are lost as the amount of off-resonance increases. b) Off-resonance due to concomitant fields. MTFs for off-resonance due to concomitant fields shows good performance can be expected up to about 1 cycle of accrued phase. c) The effect of decay during the readout. Differing amounts of T_2 decay are simulated with 0.5 cycles of off-resonance phase accrual. Severe shaping of the MTF is only seen when the T_2 time constant approaches the readout length (10 ms).

the actual form of which is unimportant for this case. As mentioned previously, in this case the phase-accrual time function takes a more complex form. Specifically,

$$\tau(t) = \frac{1}{g_m^2} \int_0^t [G_x(t')^2 + G_y(t')^2] dt \tag{4.3}$$

where g_m^2 is the maximum gradient strength reached during the scan, and $G_x(t')$ and $G_y(t')$ are the spiral gradients on the two in-plane axes [76]. Because this time function depends on the gradients-squared and because the spiral-in/out gradients are symmetric, it is easy to see that $\tau(-t) = -\tau(t)$ and the same steps of the derivation outlined in Section 4.6 can be followed to find that the signal in the presence of concomitant gradient effects is:

$$s(t) = \int m(\mathbf{r}) e^{-j2\pi k(t)\mathbf{r}} \cos[\omega_c(\mathbf{r})\tau(t)] d\mathbf{r} \tag{4.4}$$

The typical phase-accrual time function for spiral gradients is, overall, less steep than the linear function that governs B_0 off-resonance [78]. Thus, the redundant in/out scheme is more robust to phase errors caused by concomitant fields, and will perform well up to about 1 cycle of accrued phase (Fig.4.3b).

4.2.1.3 Relaxation

So far we have ignored relaxation effects during the readout period. In non-redundant multi-shot spiral-in/out scanning, T_2 relaxation during the readout results in stronger signal at one side of the periphery of k-space than the other due to an amplitude mismatch between the beginning of the readout and the end, the result of which is artifacts that look strikingly similar to those caused by off-resonance. If we add a T_2 decay term to Equation 4.1 and assume that the readout time is short compared to T_2 , we can arrive at the following expression for the signal in the presence of both off-resonance and T_2 decay (see Section 4.7 for this derivation)

$$s(t) = \int m(\mathbf{r})e^{-j2\pi k(t)\mathbf{r}} \cos[\omega(\mathbf{r})t]d\mathbf{r}$$
$$+ j \int m(\mathbf{r})e^{-j2\pi k(t)\mathbf{r}} \frac{t}{T_2(\mathbf{r})} \sin[\omega(\mathbf{r})t]d\mathbf{r} \quad (4.5)$$

This signal is complex, with a real part corresponding to our familiar cosine-modulated signal equation and an imaginary part that varies in amplitude with time. This is potentially worrisome, since we rely on phase cancellation to remove off-resonance effects. Two facts save us: First, we remember that time runs from -T/2 to T/2 and note that at $t = 0$, the imaginary component drops out. It follows that, at the center of k-space where the majority

of the image energy resides, there is little impact from the imaginary component of Eq. 4.5. Second, the ratio of $t/T_2(\mathbf{r})$ that controls the amplitude of the imaginary component will always be small as long as T_2 is larger than t_{max}, which should nearly always be the case for physiologic relaxation values and readout lengths. However, problems may arise in the case of gradient-echo imaging of short T_2^* species.

If we assume no off-resonance (or that off-resonance is corrected somehow) and set $\omega(\mathbf{r}) = 0$, we see that the averaging operation in redundant sampling works to remove T_2-induced artifacts in redundant sampling. In truth, even if we relax the linear approximation utilized in the derivation (as would be necessary for a gradient-echo scan to account for T_2^* decay), it is easy to visualize that in redundant sampling there will be a symmetric emphasis on the outer regions of k-space, the result of which is more benign than the asymmetric T_2 weighting that occurs for non-redundant spiral-in/out trajectories.

In simulations, the combination of T_2 and off-resonance is not too different from either case alone. Figure 4.3c shows the performance of the redundant method in the presence of both inhomogeneity and T_2 relaxation in terms of the MTF. As expected, strong shaping of the MTF only occurs for T_2 on the order of readout length (10 ms). However, even at this extremely short T_2 , there is little degradation of the PSF (not shown). The imaginary term in Eq. 4.5, and thus potentially damaging phase due to T_2 relaxation, is negligible.

To demonstrate these ideas and wrap up this subsection, Figure 4.4 shows the excellent performance of the redundant in/out trajectory versus spiral-out and non-redundant spiral in/out trajectories in a numerical phantom which was first inverse-gridded, then had either simulated T_2 decay, moderate off-resonance, or both applied, then reconstructed normally. For all parameters, the redundant in/out trajectory out-performs the spiral-out and non-
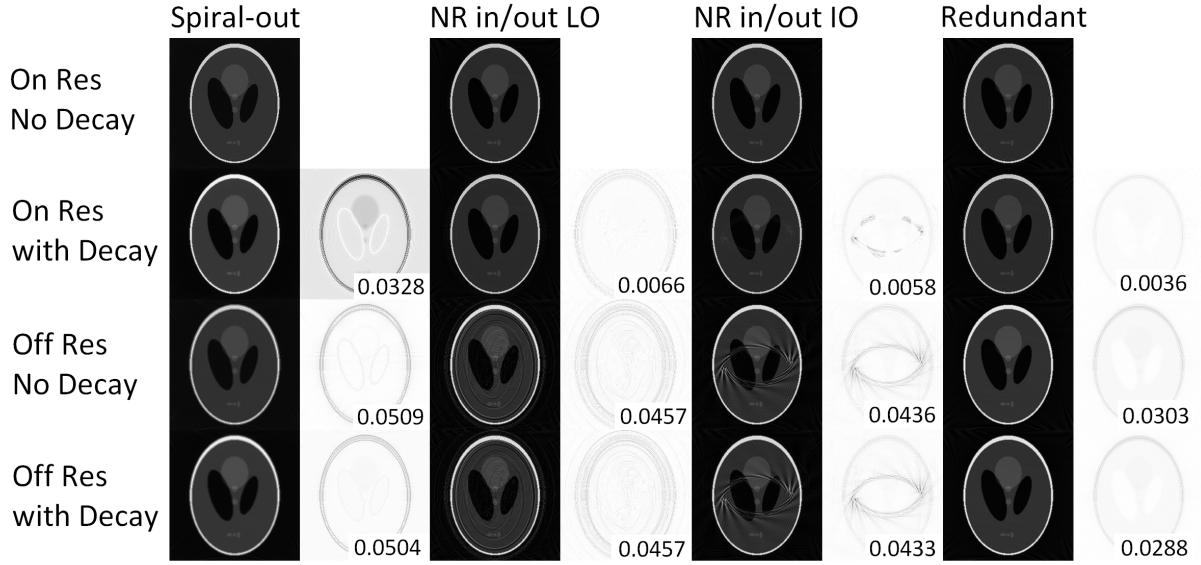
Figure 4.4: Reconstructions of numerical phantom inverse-gridded with spiral-out, non-redundant, and redundant trajectories. Two non-redundant (NR) trajectories are included in this simulation. For linear ordering (LO), all spiral-in arms are clustered (see Fig. 4.1a). In interleaved ordering (IO), each spiral-in arm is surrounded by a spiral-out arm. Difference images are versus ideal (On Resonance, No Decay) image and color-inverted for ease of visualization. Row 2 difference is x5; all others are x1. Number of interleaves = 15 for spiral-out and both non-redundant trajectories, 30 for redundant. Numbers in bottom right of difference images indicate RMSE versus ideal image.

redundant in/out trajectories in terms of RMSE.

4.2.2 Variations, extensions, and applications

In this subsection, we will briefly discuss a method by which the spiral-in/out trajectory can be used to measure the center frequency of the slice, as well as how the performance of the trajectory is affected when only a portion of the data is redundant, and finally an application for the trajectory in the context of spiral TSE imaging.

4.2.2.1 Center frequency measurement

If we consider only the linear terms of $\omega(\mathbf{r})$ in Eq. 4.1,

$$\omega(\mathbf{r}) = \omega_0 + \omega_r\mathbf{r} \tag{4.6}$$

then we can soon arrive at a modified signal equation for non-Cartesian imaging,

$$s(t) = \int m(\mathbf{r})e^{-j2\pi k'(t)\mathbf{r}}e^{-j\omega_0 t}d\mathbf{r} \tag{4.7}$$

where $k'(t)$ is the k-space trajectory warped by the linear components of the off-resonance field. The center frequency term is not a function of space and can therefore be removed from the integral. Then, from the difference $\Delta\phi$ between the accrued phases of the two redundant signals,

$$\Delta\phi(t) = 2\omega_0 t \tag{4.8}$$

This center frequency information is therefore inherently available in redundant in/out data with minimal processing. If the field is homogeneous enough across the imaging plane, this measurement may be enough to correct for the worst residual off-resonance artifacts that remain from redundant spiral-in/out imaging. Alternatively, the difference measurement may be performed at any time prior to gridding, so it may be used after the data/trajectories have been corrected based on other inhomogeneity correction methods (i.e., a linear correction based on an acquired field map) to further fine-tune the off-resonance performance of the reconstruction.

4.2.2.2   Partial Echoes and Partial k-space

One disadvantage of spiral-in/out trajectories is that the minimum TE achievable is relatively high (to account for the spiral-in arm). Partial echo methods may be of use to either shorten minimum TEs, or to improve resolution by lengthening the spiral-out portion of the acquisition relative to the spiral-in. For example, if we double the duration of the spiral-out arm relative to the spiral-in (equivalently, halve the spiral-in duration), we asymmetrically collect the echo. Then the central portion of k-space will be fully redundantly sampled, but the outer 1/3 of k-space will only be sampled with one spiral arm. This is slightly different from the normal practice in partial echo sampling where a portion of k-space is not sampled at all, and the missing data is filled in with some algorithm *du jour*. Here, we do collect full-resolution data, but non-redundantly.

Partial echoes may have use when achieving a minimal TE is of interest, but they do nothing to reduce overall scan time. In order to reduce exam times, we must reduce the number of interleaves required. One way to do this would be through parallel acceleration techniques, which will not be addressed here. Another option is to perform "partial" Fourier imaging by skipping certain interleaves. Similarly to the partial echo case, we will not actually skip data from any part of k-space. Instead, we will acquire some interleaves that are redundant, and some that are not. Thus, the redundantly sampled data will be interspersed radially among the non-redundant data. The artifacts that arise from such an acquisition strategy will not be as benign as the partial echo case (in that case, the central region was redundantly sampled, so the artifacts were relatively high-frequency and low amplitude).

In both the partial echo and partial Fourier cases, *a posteriori* knowledge may be used

to correct non-redundant data. For example, a simple center-frequency correction applied to data copied from the complimentary scan to match the global system center frequency offset removes a surprisingly large amount of artifacts arising from partial acquisition methods.

4.2.2.3   Spin Echo Imaging

Though the redundant spiral-in/out trajectory works for both gradient-echo and spin-echo imaging, spin-echoes provide a natural setting in which to apply them. Since the TE of spin-echo scans is generally longer, the spiral-in portion of the trajectory can be inserted with little or no increase in minimum TE. Second, the in/out trajectory aligns the gradient echo generated by the spiral gradients with the spin echo formed by the RF pulses at the center of the gradient waveform, resulting in higher signal when the center of k-space is sampled.

Simple spin-echo sequences are rarely used today, as their faster TSE-type cousins are capable of generating similar contrast in a fraction of the time. One attractive application for the redundant spiral-in/out trajectory is in a slab-selective version of the 3D spiral TSE sequence of Chapter 3. In this variant, multiple averages with RF chopping are used to remove spurious echo artifacts that arise from imperfect refocussing pulses in the echo train. Since the origins of the spurious echo artifacts and the spiral-in/out artifacts are different, we can combine the second, redundant acquisition with the RF-chopped acquisition to acquire a fully redundant trajectory with no increase in scan time.

4.3 Methods

A resolution phantom was scanned on a 1.5 T Siemens Avanto scanner with a gradient-echo spiral sequence with a spiral-out trajectory and a redundant spiral-in/out trajectory. Acquisition parameters were: number of interleaves 14 (28 for spiral-in/out), spiral duration 10 ms, in-plane FoV 300 mm, slice thickness 5.0 mm. To examine off-resonance performance, the sequences were run once with a good shim applied, and again with the receive frequency manually tuned 20, 40, 80, and 160 Hz off-resonance (corresponding to 0, 0.2, 0.4, 0.8, and 1.6 cycles of off-resonance accumulated at the end of the readout). All images were acquired in the transverse plane, and were gridded and Fourier-transform-reconstructed with no off-resonance correction applied in reconstruction. The gridding operation automatically sums the data at the proper k-space locations, given the redundant trajectories.

The center frequency for each spiral-in/out acquisition listed above was measured by fitting a line to the difference between the phase of the redundant raw data for each interleaf (Equation 4.8). To maximize SNR for these measurements, only the center 1/5 of the data was used. The average off-resonance value was taken as the mean of the interleaf measurements after removing the highest and lowest two values.

A partial echo acquisition was simulated by truncating the last 3/8 of the 40 Hz off-resonance data. The data was first reconstructed normally, with care to only average data that was acquired redundantly (i.e., the center 1/4 of k-space). Secondly, the missing portions of the spiral-out arms were phase-corrected based on the known center frequency offset (the offset value is obtained either from an acquired field map or from the center frequency measurement described previously).

Next, a partial Fourier acquisition was simulated with the 40 Hz off resonance data by setting the data from every third interleaf to zero. In this manner, one redundant interleaf results for every two non-redundant interleaves and the total acquisition time is reduced by 36% in simulation. The data was reconstructed as before, once with no correction applied, then with simple center-frequency adjustment of non-redundant data.

To investigate concomitant field performance, the resolution phantom was imaged again with both spiral-out and spiral-in/out trajectories with 14 interleaves (28 for spiral-in/out), spiral duration 6.4 ms, in-plane FOV 300 mm, and slice thickness 3 mm in a double-oblique orientation (($C \rightarrow S$ -41.8°)$\rightarrow$ -27.8°) near the magnet isocenter (X -9.8 mm, Y -39.6 mm, Z -21.7 mm), then moved 50 mm along the z-axis (X -9.8 mm, Y -39.6 mm, Z -71.7 mm) and imaged again to ensure significant concomitant fields.

To test whether the redundant trajectory can be acquired concurrent with the second, RF-chopped average of a spin echo sequence, a resolution phantom was scanned on a 3.0 T Siemens Trio scanner with a slab-selective 3D stack-of-spirals TSE sequence with a spiral-out trajectory (2 averages required), a spiral-in/out trajectory in which the redundant interleaves are acquired in separate chopped scans (4 averages required), and a spiral-in/out trajectory which combines the redundant interleaf scan with the chopped scan (2 averages required). Acquisition parameters were: spiral duration 6.4 ms, in-plane FoV 300 mm, number of slices = 32, slice thickness 1.0 mm. Averages were combined after linear off-resonance correction was applied to the k-space trajectories and after gridding the data separately.

To test the redundant in/out trajectory *in vivo*, a slab-selective version of the variable-flip-angle 3D spiral TSE (spiral SPACE) sequence was used on a normal volunteer for T_2-weighted brain imaging [79]. Scan parameters were: TR/TE 3000/200, spiral duration 6.4 ms, in-plane

FoV 250 mm, number of slices = 64, slice thickness 1.0 mm. Forty-nine interleaves were used for both spiral-out and spiral-in/out acquisitions. For spiral-in/out, the second, redundant interleaf scan was combined with the chopped scan so that the total acquisition time for both sequence variations was identical. No off-resonance correction algorithm was applied in reconstruction in order to better exhibit the improved off-resonance performance of the redundant in/out sequence.

Additionally, the redundant in/out trajectory was applied to non-contrast MRA of the leg, as described in Chapter 3. Again, the redundant in/out trajectory was compared to a spiral-out trajectory.

4.4 Results

The redundant spiral-in/out trajectory shows excellent robustness for off-resonance values ranging up to 0.5 cycles (Fig. 4.5). Above this value, blurring appears and is comparable to a spiral-out scan performed with half the amount of off-resonance applied, which is consistent with the time elapsed between when the center and edges of k-space are acquired being half that for a spiral-in/out trajectory. Furthermore, the increase in SNR is apparent in Figure 4.5 for the in/out scan due to averaging of the redundant data.

Center frequency measurements by the phase difference method are highly correlated with the actual, manually tuned frequencies and with the values measured with a separately acquired field map (Fig. 4.6). A slight bias of ≈ 8 Hz was observed when using the phase difference method.

Partially redundant sampling schemes remain resistant to blurring (Fig. 4.7). Both asym-
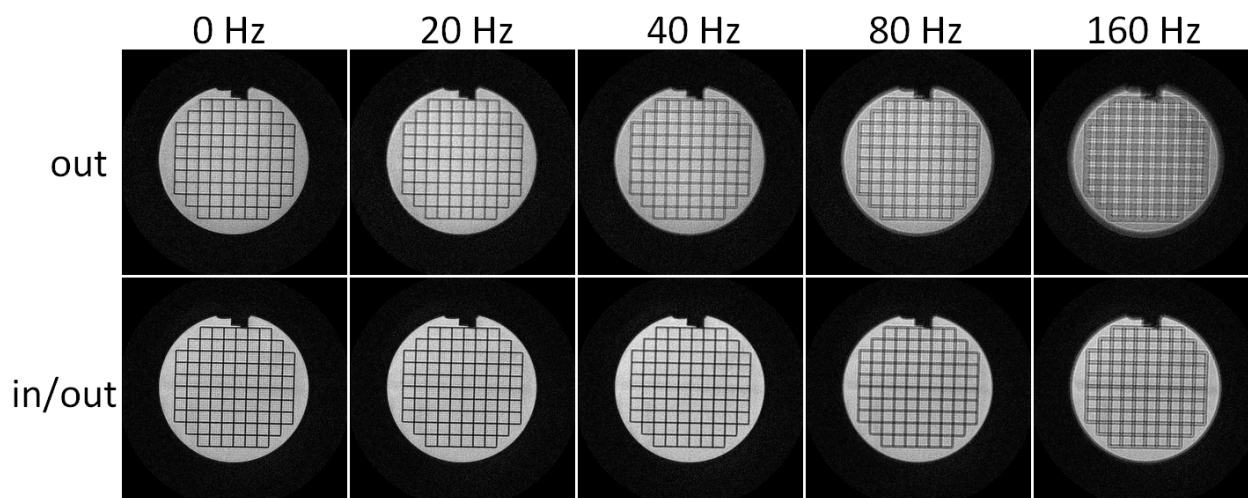
Figure 4.5: Phantom images at various amounts of off-resonance. Top row: Spiral-out. Bottom row: Spiral-in/out. No off-resonance correction was applied. Images were acquired with a 10 ms readout, resulting in cycles of phase accumulated at the end of the readout: 0 Hz = 0 cycles, 20 Hz = 0.2 cycles, 40 Hz = 0.4 cycles, 80 Hz = 0.8 cycles, 160 Hz = 1.6 cycles.
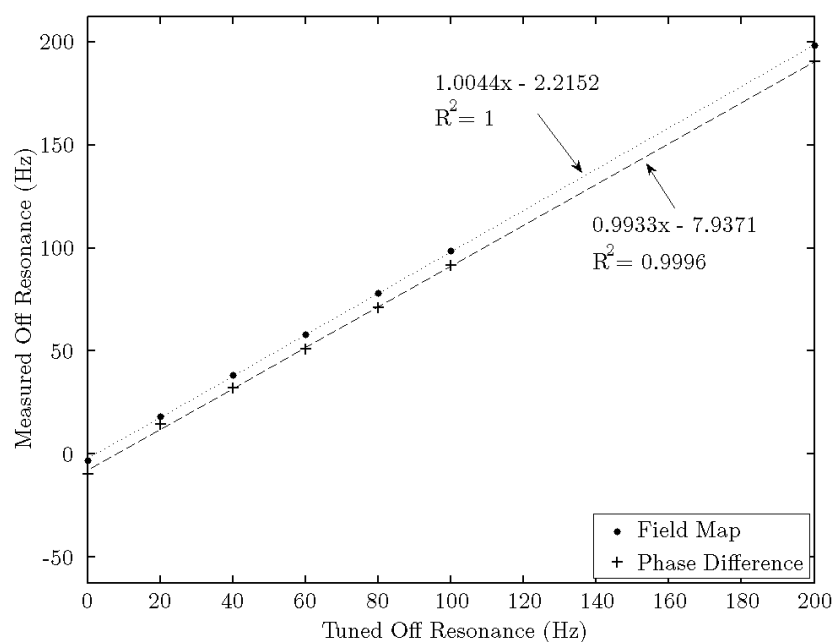
Figure 4.6: Center frequency measured by an extra field map acquisition and by the phase difference between redundant scans.
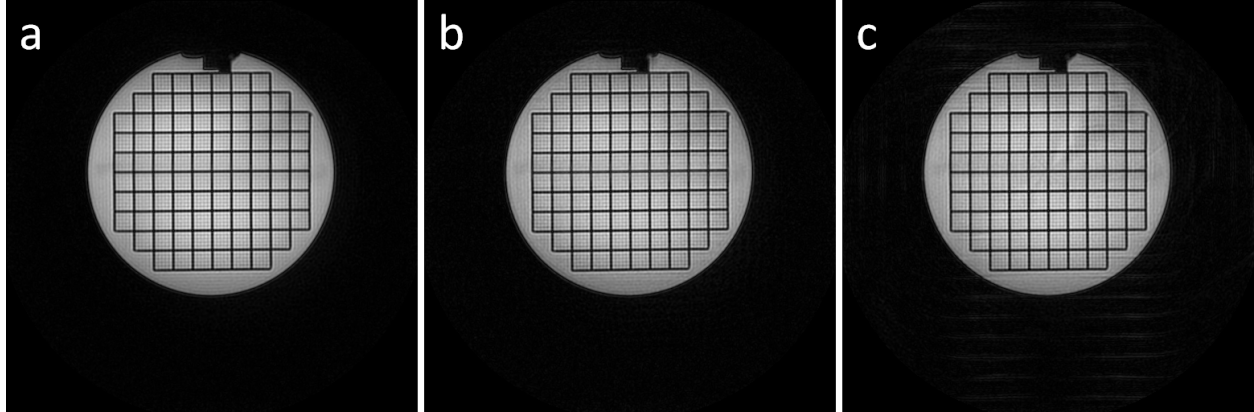
Figure 4.7: Partially redundant methods. a) Fully redundant data acquired 40 Hz off-resonance and center-frequency corrected prior to gridding. b) Partial echo data. The last 3/8 (1875 data samples) of the fully redundant data was set to zero prior reconstruction, resulting in an outer ring of non-redundant high-frequency data in k-space. c) Partial k-space data. Two thirds of the data was simulated as non-redundant by setting every third interleaf of the fully redundant data to zero prior to reconstruction (i.e. for each redundant interleaf there are two non-redundant interleaves). Artifacts are more apparent than in (b) due to the less-benign k-space pattern of non-redundancy.

metric sampling (partial echo) and partial k-space sampling methods benefit from simple center-frequency correction of the non-redundant data (non-corrected images not shown), resulting in images of comparable quality to those reconstructed from fully-redundantly sampled data. Artifacts are present in Figure 4.7c due to the reduced fraction of fully-redundantly sampled data (only 1/3 of the interleaves are redundant) and the interspersed nature of the non-redundant data amongst the redundant.

Figure 4.8 compares the spiral-out and spiral-in/out trajectories for double-oblique imaging planes near the magnet isocenter and off-center. The spiral-in/out trajectory results in images largely free from blurring due to concomitant fields.

Figure 4.9 shows that the redundant trajectory acquisition can be combined with an RF-chopped second average in slab-selective imaging to gain the benefits of the redundant trajectory with no increase in scan time. One slice is shown from a 3D volume.
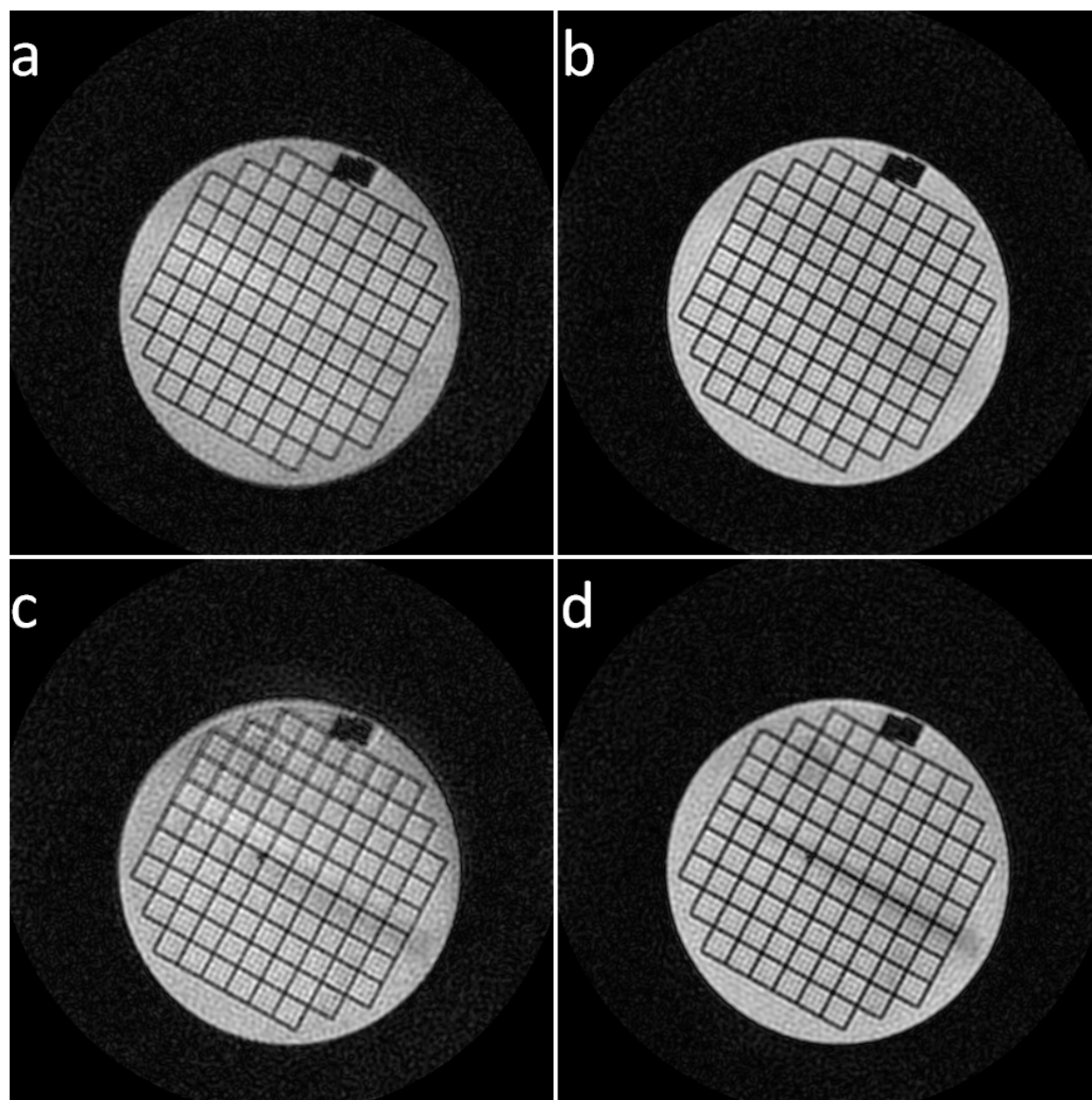
Figure 4.8: Trajectory performance in the presence of concomitant fields. a) Spiral-out at isocenter. b) Spiral-in/out at isocenter. c) Spiral-out off-center. Note blurring near the top of the phantom due to concomitant fields. d) Spiral-in/out off-center. Blurring due to concomitant fields is removed.
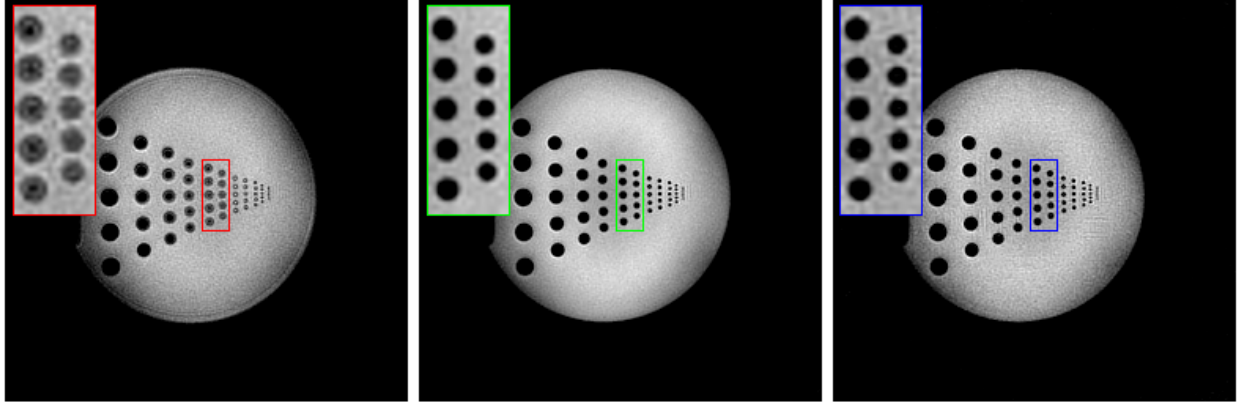
Figure 4.9: One slice from a 3D stack-of-spirals sequence. (Left) Spiral-out, (Middle) Redundant spiral-in/out acquired in 4 averages, (Right) Redundant spiral-in/out acquired in 2 averages by combining the RF-chopped average with the redundant trajectory acquisition.

One slice from a 3D stack-of-spirals TSE *in vivo* dataset acquired with both spiral trajectories is shown in Figure 4.10. Contrast is slightly different between the sequences because the spiral-out version begins spiraling out from the k-space origin before the spin-echo has formed, whereas the spiral-in/out centers the acquisition of the center of k-space on the spin echo. Overall, the images acquired with the spiral-in/out trajectory are sharper, and in regions of high B_0 inhomogeneity, show much improved off-resonance performance.

Figure 4.11 shows vessel sharpness improvement when the redundant in/out trajectory is used for non-contrast MRA. As before, when combined with slab selection with chopping, this improvement is gained with no increase in scan time.

4.5   Discussion & Conclusion

The redundant spiral-in/out trajectory is an attractive acquisition-based method to naturally mitigate blur due to off-resonance in spiral scanning, albeit with a significant time disadvantage for many applications. The technique produces excellent image quality with the
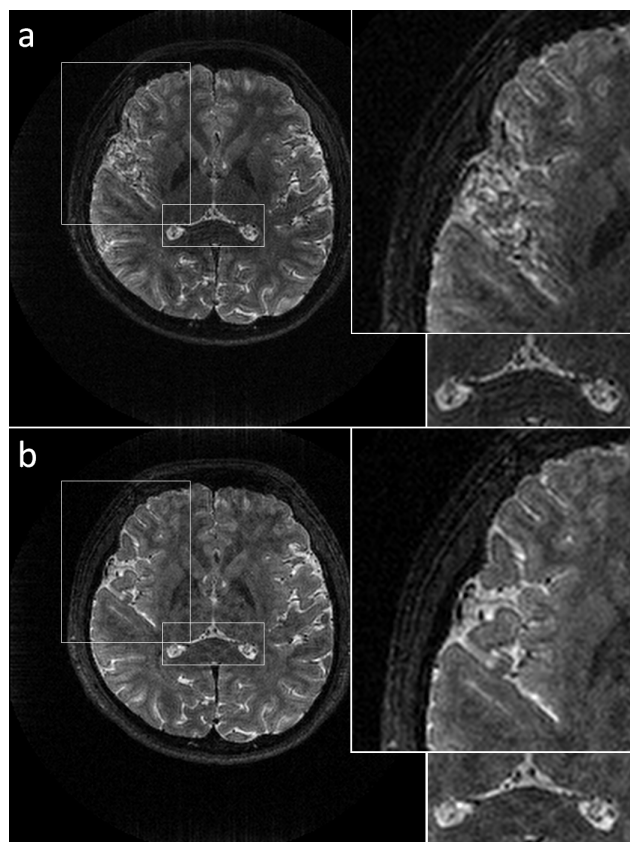
Figure 4.10: Comparison of spiral-out and redundant spiral-in/out in a volunteer with no off-resonance correction applied to either dataset. One slice is shown from a slab-selective 3D stack-of-spirals trajectory. a) Spiral-out. Significant blurring is observed in areas with poor B_0 homogeneity (insets). b) Spiral-in/out. Excellent off-resonance performance is obtained with no increase in scan time.
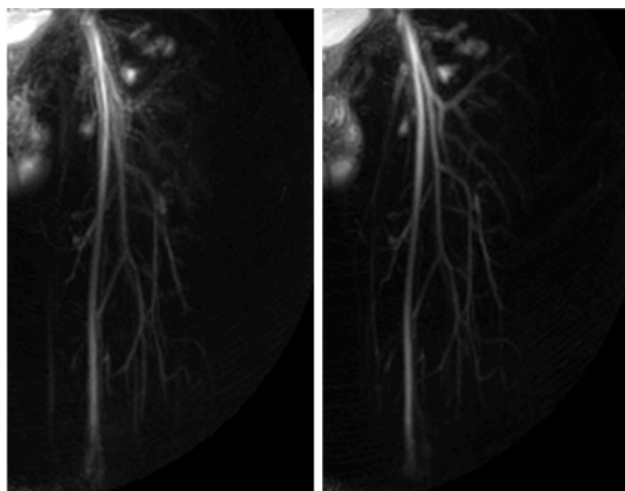
Figure 4.11: Comparison of spiral-out and redundant spiral-in/out in a volunteer with no off-resonance correction applied to either dataset. A MIP image from the left leg is shown. On the left is an image from the spiral-out scan. Blurring is observed near the femoral bifurcation as well as more distally. The right image, from the spiral-in/out scan shows much improved sharpness of the femoral artery.

simplest of post-acquisition correction methods, allowing simple, fast reconstructions to take place. Although all of the data presented here was performed with a single receive channel, we anticipate this technique will perform well in parallel imaging implementations, allowing fast reconstructions to take place at scan time. The complexity and reconstruction time for non-Cartesian parallel reconstructions (which, in addition to removing non-Cartesian aliasing artifacts, have had to address the off-resonance issue) has been a major hurdle in their development.

For small values of off-resonance, the k-space signal in redundant sampling experiences a cosine amplitude window, which is a different (and more benign) mechanism for resolution loss compared to the PSF broadening observed in spiral-out scanning. However, as in regular spiral imaging, this slight blurring will be space-variant depending on local off-resonance values. For larger off-resonance values (or for long readout lengths), the cosine modulation will begin nulling important frequencies in k-space as a function of k-space radius, resulting in more severe image artifacts. Here, we propose to get close to the true off-resonance field through an acquired field map and subsequent linear estimation of the field. As long as the maximum deviation from this estimate is relatively small, the redundant spiral-in/out method will remove the majority of blur due to residual off-resonance. As is the case for traditional spiral-out imaging, highly inhomogeneous fields will limit redundant spiral-in/out scanning to short readout durations.

The fact that the redundant spiral-in/out trajectory necessarily requires twice the number of interleaves as a spiral-out trajectory to achieve a similar resolution cannot be overlooked. Partial k-space and, to an extent, partial echo sampling provide simple ways to reduce scan time. As we have shown that even the most simple frequency correction applied to the

non-redundant data in simulated partial k-space and partial echo acquisitions can result in excellent image quality, we anticipate future reconstruction algorithms which can take full advantage of the presence of both redundant and non-redundant data generated by these sampling schemes. Furthermore, for slab-selective 3D spiral TSE imaging, at least, we have combined the redundant acquisition with the RF-chopped second average with no penalty in scan time. The spiral-in/out trajectory is a natural method for spin-echo and TSE sequences since it aligns the gradient echo with the spin echo. For other cases where spiral trajectories are regularly used with multiple averages (e.g. fMRI, ASL), redundant in/out trajectories can be used with no overall increase in scan time.

The redundant spiral-in/out trajectory is similar to the prevailing spiral-in/out trajectory used in fMRI, wherein the trajectory spirals out along the same path as the spiral-in portion [80, 81]. Typically, fMRI scans are performed with few interleaves (often single-shot), and the spiral-in and spiral-out data is reconstructed separately, then adaptively combined on a pixel-by-pixel basis [80, 82]. The trajectories used in fMRI then, are redundant, although they do not adhere to the mirror-symmetry requirement of Equation 4.11. Thus, the signal equations derived in this paper do not necessarily apply in the same manner to this class of spiral-in/out trajectory.

4.6 Derivation of Equation 4.2

For redundant spiral-in/out trajectories, we must define a few properties of the k-space trajectory.

$$t \in [-T/2, T/2] \tag{4.9}$$

$$k_1(-t) = -k_1(t) \tag{4.10}$$

$$k_2(t) = k_1(-t) = -k_1(t) \tag{4.11}$$

That is, the two trajectories are symmetric about the origin and they are mirror images of one another. Inserting into Equation 4.1, the corresponding signal equations are

$$s_1(t) = \int_{-T/2}^{T/2} m(\mathbf{r})e^{-j2\pi k_1(t)\mathbf{r}}e^{-j\omega(\mathbf{r})t}d\mathbf{r} \tag{4.12}$$

$$s_2(t') = \int_{-T/2}^{T/2} m(\mathbf{r})e^{-j2\pi k_2(t')\mathbf{r}}e^{-j\omega(\mathbf{r})t'}d\mathbf{r}$$
$$= \int_{-T/2}^{T/2} m(\mathbf{r})e^{+j2\pi k_1(t')\mathbf{r}}e^{-j\omega(\mathbf{r})t'}d\mathbf{r} \tag{4.13}$$

However, the second acquisition is run in the opposite direction through k-space, so we should time-reverse $s_2(t)$. Let $t = -t'$.

$$s_2(t) = \int_{-T/2}^{T/2} m(\mathbf{r})e^{+j2\pi k_2(-t)\mathbf{r}}e^{-j\omega(\mathbf{r})(-t)}d\mathbf{r}$$
$$= \int_{-T/2}^{T/2} m(\mathbf{r})e^{-j2\pi k_1(t)\mathbf{r}}e^{+j\omega(\mathbf{r})t}d\mathbf{r} \tag{4.14}$$

Finally, we combine the signals via simple averaging.

$$s(t) = \frac{1}{2}[s_1(t) + s_2(t)]$$

$$= \frac{1}{2} \int_{-T/2}^{T/2} m(\mathbf{r})e^{-j2\pi k_1(t)\mathbf{r}}[e^{-j\omega(\mathbf{r})t} + e^{+j\omega(\mathbf{r})t}]d\mathbf{r}$$

$$= \int_{-T/2}^{T/2} m(\mathbf{r})e^{-j2\pi k_1(t')\mathbf{r}}[\cos\omega(\mathbf{r})t]d\mathbf{r} \tag{4.15}$$

In all other sections of this manuscript, the integral limits (-T/2,T/2) are taken to be understood.

4.7 Derivation of Equation 4.5

If we start again with Eqs. 4.12 and 4.14 and insert a T_2 decay term,

$$s_1(t) = \int m(\mathbf{r})e^{-j2\pi k_1(t)\mathbf{r}}e^{-j\omega(\mathbf{r})t}e^{-t/T_2(\mathbf{r})}d\mathbf{r} \tag{4.16}$$

$$s_2(t) = \int m(\mathbf{r})e^{-j2\pi k_1(t)\mathbf{r}}e^{+j\omega(\mathbf{r})t}e^{+t/T_2(\mathbf{r})}d\mathbf{r} \tag{4.17}$$

The combined signal is therefore

$$s(t) = \frac{1}{2} \int m(\mathbf{r})e^{-j2\pi k_1(t)\mathbf{r}}[e^{-t/T_2(\mathbf{r})}e^{-j\omega(\mathbf{r})t}$$

$$+ e^{+t/T_2(\mathbf{r})}e^{+j\omega(\mathbf{r})t}]d\mathbf{r} \tag{4.18}$$

For physiologic relaxation values and the time scales that readouts are performed at, T_2 decay is approximately linear (for example, even a severe T_2 value of 10 ms will only result in a 13% deviation from linearity over a 10 ms readout). We can therefore estimate

$e^{t/T_2(\mathbf{r})} \approx 1 + t/T_2(\mathbf{r})$ and $e^{-t/T_2(\mathbf{r})} \approx 1 - t/T_2(\mathbf{r})$ to arrive at Equation 4.5:

$$
\begin{aligned}
s(t) &= \frac{1}{2}\int m(\mathbf{r})e^{-j2\pi k_1(t)\mathbf{r}}[(1 - t/T_2(\mathbf{r}))e^{-j\omega(\mathbf{r})t} \\
&\quad + (1 + t/T_2(\mathbf{r}))e^{+j\omega(\mathbf{r})t}]d\mathbf{r} \\
&= \frac{1}{2}\int m(\mathbf{r})e^{-j2\pi k_1(t)\mathbf{r}}[(e^{-j\omega(\mathbf{r})t} + e^{+j\omega(\mathbf{r})t}) \\
&\quad - \frac{t}{T_2(\mathbf{r})}(e^{-j\omega(\mathbf{r})t} - e^{+j\omega(\mathbf{r})t})]d\mathbf{r} \\
&= \int m(\mathbf{r})e^{-j2\pi k(t)\mathbf{r}}\{\cos[\omega(\mathbf{r})t] \\
&\quad + j\frac{t}{T_2(\mathbf{r})}\sin[\omega(\mathbf{r})t]\}d\mathbf{r} \\
&= \int m(\mathbf{r})e^{-j2\pi k(t)\mathbf{r}}\cos[\omega(\mathbf{r})t]d\mathbf{r} \\
&\quad + j\int m(\mathbf{r})e^{-j2\pi k(t)\mathbf{r}}\frac{t}{T_2(\mathbf{r})}\sin[\omega(\mathbf{r})t]d\mathbf{r}
\end{aligned}
\tag{4.19}
$$

Chapter 5

Fluorine Imaging

The major focus of MRI technical research has been on improving resolution; increasing contrast and developing new contrasts; and shortening acquisition times of anatomical and functional images; however, patient outcomes may also be improved by acquiring spatially localized information regarding the molecular and cellular state of the patient. MRI offers the possibility to combine anatomical and molecular or cellular scans using the same equipment, lowering scan times, cost, and complexity of data interpretation. However, molecular and cellular MRI is still in early stages, and much work needs to be done before it is ready to enter the clinic.

5.1   Introduction

Despite several examples of successful ^{19}F *in vivo* imaging [39–47], the MR experiment is inherently limited by low signal sensitivity, and fluorine MRI is often hindered by low SNR due to the limited number of fluorine nuclei that can be delivered to an area of interest. In order to obtain reasonable voxel sizes during an *in vivo* imaging session, dozens or hundreds

of averaging scans are often used, resulting in lengthy examination times.

For all cellular and molecular contrast agents, the concentration of agent that actually accumulates at the region of interest is limited by dose volume, particle size, receptor and ligand concentrations, and ligand specificity to desired receptors. Fluorine is advantageous since it has no tissue background signal and thus, subtraction techniques are not required for signal detection. However, the received signal is still extremely small due to the inherently low concentrations of agent delivered to the tissue, and often resides at or near the noise in a typical experiment. For this reason, ^{19}F MRI has been primarily used for cell tracking, either using pre-loaded cells, or through *in situ* labeling via macrophage phagocytosis of PFC-containing-particles in cancer, inflammation, infection, and ischemia models.

Thus, there is a clear need for acquisition and reconstruction methods to be developed to efficiently generate and utilize signal arising from small volumes of contrast agent. To date, the problem of low SNR in ^{19}F imaging has been predominantly addressed by (1) optimizing the relaxation properties of the fluorine-containing molecule, (2) delivering more chemically equivalent fluorine nuclei to the region of interest, either by optimizing the delivery mechanism (nanoparticle formulation, ligand affinities, etc.), or (3) optimization of acquisition (pulse sequence) techniques for a particular PFC particle construction. For example, Giraudeau et al. [49] demonstrated that a reduced bandwidth refocusing pulse is useful to prolong the signal arising from PFOB during a TSE echo-train.

The ^{19}F-^{1}H imaging experiment can be thought of analogously to a SPECT- or PET-CT experiment. High specificity, often low-resolution ^{19}F images with little or no anatomical information are overlaid onto high-resolution ^{1}H anatomic images. Thus, the presence of an anatomic scan provides a large amount of side information that can be used to guide

advanced reconstruction techniques to improve fluorine image reconstruction. This idea has a long history in SPECT/PET-CT, and several techniques have been developed in order to constrain the low resolution, high sensitivity functional image reconstruction with the anatomical data provided by CT [51, 83–85]. Furthermore, there are MRI analogies to the class of super-resolution-through-image-denoising methods [50] and to techniques that have been used to jointly estimate images obtained with differing contrasts [86]. Since there should be a high correlation between where we observe fluorine signal and organ and tissue boundaries in the body, many of these ideas are directly applicable to the secondary nucleus situation.

To our knowledge, advanced reconstruction techniques have not been investigated for improving secondary-nucleus MR images. An advantage of performing ^{19}F imaging is that proton images are routinely obtained along with the fluorine scan in order to localize the fluorine signal to organs and tissues in the body. Since there should be a high correlation between where we observe fluorine signal and organ and tissue boundaries in the body, we should be able to incorporate side information from the proton localizer images into the fluorine reconstruction.

The structure of this chapter is as follows: The nanoparticles used for all ^{19}F experiments are described in Section 5.2. In Section 5.3, an experiment designed to test the SNR and SNR efficiency of several common pulse sequence sequences for ^{19}F imaging is reported. Next, in Section 5.4, an introduction to side-information-constrained model-based reconstructions is presented. Two *in vivo* experiments testing our acquisition and reconstruction methods are described in Section 5.5. Finally, in Section 5.6, we conclude with a description of more advanced constraints for the incorporation of side-information in ^{19}F imaging and apply

these methods to the *in vivo* data acquired previously.

5.2   Nanoparticle Design and Synthesis

For all studies, fluorine nanoparticles were manufactured in-house with the general design of a lipid monolayer shell surrounding a liquid perfluorocarbon core composed of perfluoro-15-crown-5-ether (CE). Crown ether supplies a single resonance peak, maximizing MR signal detection. The first iteration of nanoparticle shell design was a 100% distearoylphosphatidyl-choline (DSPC) lipid shell with a mean diameter of 280 nm. (Particle diameter was determined via dynamic light scattering.) The nanoparticle manufacturing process consisted of guiding a 4% wt/wt solution of shell compounds along with the CE (10% wt/wt) through a Nuclepore filter (of whatever size desired) 41 times. This emulsion is stable (the melting point of DSPC is well above body-temperature, meaning it forms a "hard" shell) and can be stored at 4°C for several months until needed (Fig. 5.1). When injected into mice that had undergone myocardial infarct (MI) surgery (see Section 5.5.3 for a description of MI and imaging protocols), these nanoparticles were observed to accumulate in the liver, spleen, and bone marrow (Fig. 5.2), but were *not* observed in the infarcted region of the heart. Thus, it was determined that while this formulation is phagocytosed by cells of the mononuclear phagocyte system (MPS), it is not taken up by mobile monocytes.

A second formulation was manufactured that consisted of a shell comprised of a 1:1 mixture of DSPC and dioleoylphosphatidylcholine (DOPC). The melting point of DOPC is much lower than that of DSPC, resulting in a more fluid lipid membrane. We hypothesized that this membrane would be more similar to live cells, and furthermore reduced the particle
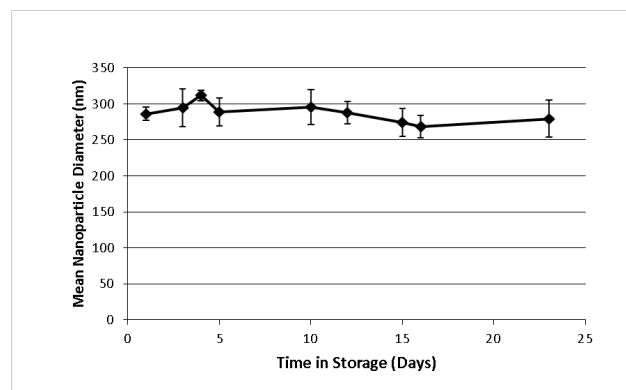
Figure 5.1: Nanoparticles with a mean diameter of 280 nm are stable for up to a month stored at 4°C.
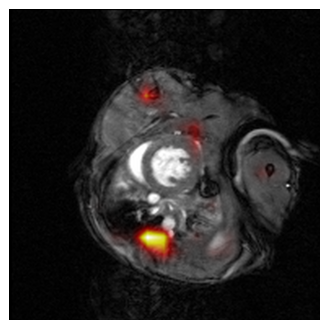
Figure 5.2: Nanoparticles with a 100% DSPC shell accumulate in the liver, spleen, and bone marrow, but are not trafficked into the infarcted region of the myocardium. In this image, ^{19}F signal in red/orange is overlaid onto the gray scale ^{1}H localizer. In this slice, ^{19}F is seen in the bone marrow of the long bones of the arms and spine and in the inflamed area around the heart due to surgery.

size to 143 nm to better match the nanoparticles described in [44], which use egg lecithin as the lipid component and have a mean diameter of 130 nm. A small amount of fluorescent lipid dye DiI can be added to supply a means for histological validation. Figure 5.3 illustrates the non-targeted nanoparticle composition. All further experiments described in this chapter used these nanoparticles.
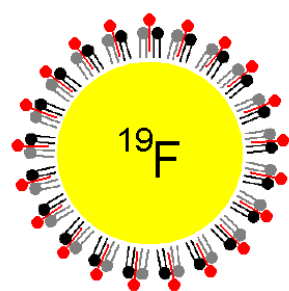
Figure 5.3: Nanoparticle composition. Non-targeted nanoparticles consist of a core of liquid PFC surrounded by a lipid monolayer consisting of a 50:50 mixture of DSPC and DOPC. A fluorescent dye, DiI, is incorporated into the lipid shell.

5.3 Optimization of Acquisition Methods

To date, no systematic pulse sequence optimization for ^{19}F MRI has been reported in the literature. We performed a comparison of the SNR efficiency of six different pulse sequences. The criteria we used was: the sequence must have "whole-mouse" coverage, since we cannot know beforehand where ^{19}F nanoparticles will accumulate, and the sequence must be cardiac and respiratory gated, to minimize artifacts due to motion.

5.3.1 Methods

A phantom was constructed with the nanoparticles outlined in previous section at various concentrations (Fig. 5.4), then imaged with 2D and 3D versions of a range of common MR pulse sequences (GRE, bSSFP, and TSE) to determine the best imaging sequence to use for whole mouse imaging. All sequences acquired data with the same acquisition bandwidth (780 Hz/pixel), field of view (35 x 35 mm^2; 5 mm slice thickness, accomplished either through slice selection or 3D phase encoding), matrix size (64 x 64), and number of acquisitions (25) to enable fair comparison. Other imaging parameters are given in Table 5.1. SNR efficiency was calculated assuming 40% acquisition gating efficiency for GRE and bSSFP sequences. Note that in Figures 5.5 and 5.6, the bSSFP sequence is referred to as "TrueFISP," the Siemens' vendor-specific name for this sequence.

5.3.2 Results and Conclusions

In Figure 5.5, it is clear that the 3D bSSFP and 3D TSE sequences result in the most signal from small concentrations of ^{19}F. These results are summarized in Fig. 5.6. Because of

Figure 5.4: Phantom used in sequence comparison studies. The concentration of ^{19}F in each tube is as follows: 1 = 2.00 M, 2 = 0.80 M, 3 = 0.32 M, 4 = 0.13 M, 5 = 0.05 M, 6 = 0.02 M, 0.00 M (control).

Imaging Parameters			
Pulse Sequence	TR (ms)	TE (ms)	Flip Angle (deg)
2D GRE	100	1.2	25
3D GRE	100	1.8	25
2D bSSFP	4.4	2.2	70
3D bSSFP	4.0	2.0	70
2D TSE	3000	4.9	180
3D TSE	3000	10	180

Table 5.1: Imaging parameters used for each pulse sequence for phantom imaging.

the long T_2 of CE (T_2 for CE is on the order of 500 ms), bSSFP and TSE pulse sequences have higher SNR efficiency than gradient echo (GRE). bSSFP exhibited field inhomogeneity artifacts, but TSE was robust in the presence of field inhomogeneity artifacts. Another advantage of TSE relative to bSSFP is that data is acquired for less than 100 ms out of every 3 s, leaving ample time for acquiring proton images. Based on these results, we believe that 3D TSE with cardiac and respiratory gating is a highly efficient pulse sequence for cardiovascular ^{19}F imaging.

5.4   Model-based Reconstruction Methods

In model-based reconstructions, the image is estimated by minimizing a penalized least squares cost function:

$$\hat{f} = \arg\min_{f} \|y - Af\|^2 + \beta R(f) \tag{5.1}$$
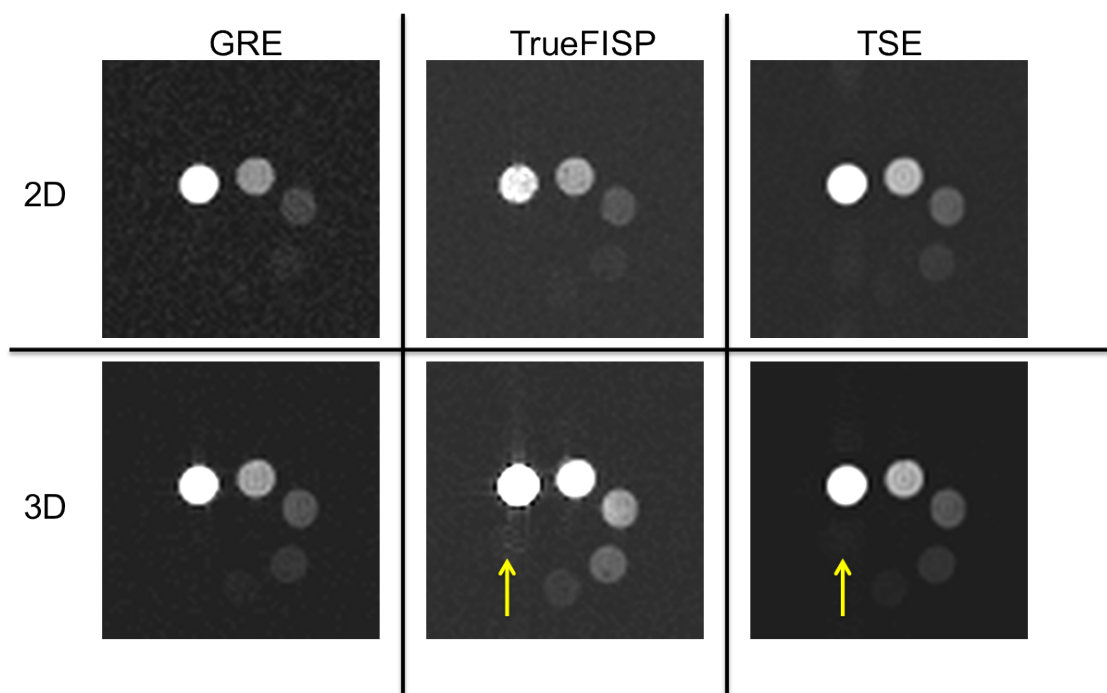
Figure 5.5: Axial ^{19}F images of the dilution phantom of Figure 5.4 from a range of pulse sequences. Tube 6 (0.02 M ^{19}F concentration) is visible (though with very low signal) in the 3D bSSFP and 3D TSE images.
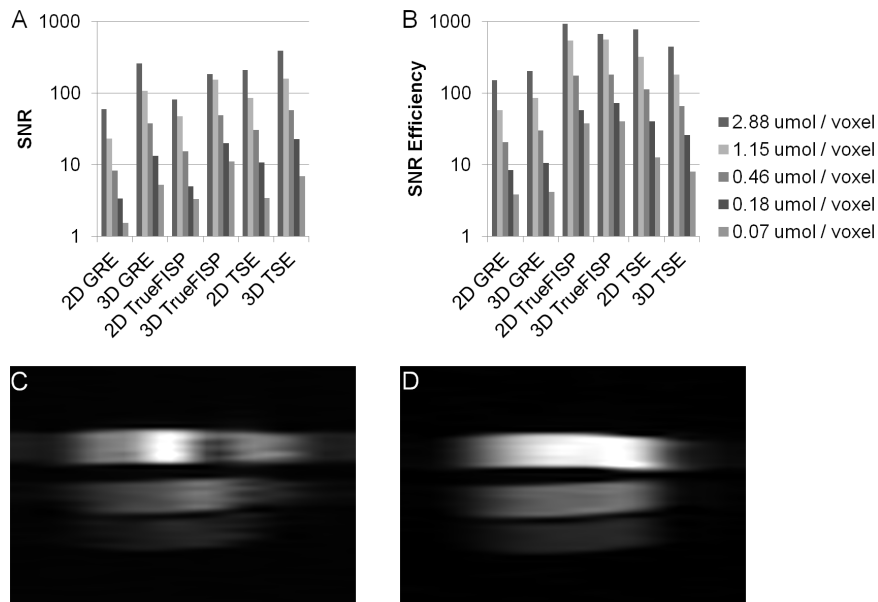
Figure 5.6: Measured SNR (A) and calculated SNR efficiency (B) for a series of ^{19}F phantom dilutions. SNR efficiency was calculated as the measured SNR divided by the square root of total scan time. The bSSFP (TrueFISP) sequence is a good choice for ^{19}F imaging of the CE perfluorocarbon due to its T_2/T_1 ratio. However, over large volumes, main magnetic field inhomogeneity causes artifacts when using this sequence (C). The TSE sequence also demonstrates large ^{19}F signal, and is largely free from inhomogeneity artifacts (D).

where y is the data, A is the system matrix, and f is the image we wish to reconstruct. The first part of Equation 5.1 is a data fidelity term which penalizes inconsistency between the image estimate and the observed data. The second part of the equation, $R(f)$, is a regularization term, which can take many forms. The β parameter controls the influence that the regularization term has on the resulting image estimate.

Side information can be incorporated into the reconstruction through the regularization term, $R(f)$, in Equation 5.1. A simple regularizer to implement is a quadratic roughness penalty with the form:

$$R(f) = \|Cf\|_w^2 \tag{5.2}$$

where C is a differencing matrix and w are weights that control the amount of smoothing and are used to identify boundaries in the image over which smoothing should not be performed. When the weights, w, are uniform, this regularizer penalizes all roughness (edges) in the reconstructed image estimate and improves SNR by local signal averaging at the expense of resolution. However, we expect fluorine signal to remain confined to well-defined regions (organs and tissues), and not be diffusely spread with equal intensity across known image boundaries, and so can make different choices for w based on the expected distribution of signal. There are many possible approaches to choosing the weighting coefficients based on known anatomy. Here, we will investigate two:

1. Binary weights can be formulated by manual segmentation of regions of interest (ROIs) in proton images, and setting the edges of these ROIs as the boundary locations for ^{19}F reconstruction. The weight takes a 0 or 1 value depending on whether or not an edge is present in the mask (0 equals edge). Conceptually, the weights prevent

smoothing across boundaries, but allow smoothing elsewhere [51].

2. A more general approach we have investigated is to define the weights as:

$$w_j = 1 - \mathcal{N}(|Cf|) \tag{5.3}$$

with $N()$ normalizing to a 0-1 scale. This is an approach similar to Haldar et al. [50].

The weights then have a value close to 1 in homogenous regions of the image, improving

SNR there. At image boundaries, however, the value of the weights is reduced towards

zero, with a larger difference between pixels resulting in a smaller weighting parameter.

In effect, stronger contrast between tissues in the proton image results in stronger

enforcement of edge constraints in the fluorine reconstructions. This approach has the

advantage that it requires no operator intervention to manually segment image features

of interest and that it can apply different amounts of smoothness in different areas of

the image; however, it will be dependent on strong contrast between tissues of interest

and surrounding tissue.

The quadratic regularizer is convenient for minimization and there are have been many

publications over the years documenting its use and properties; however, its essential draw-

back is that it smooths the resulting image, with higher β values leading to more smoothing.

Figure 5.7 wraps up this section by demonstrating the principle outlined above through a

simple numerical phantom experiment.
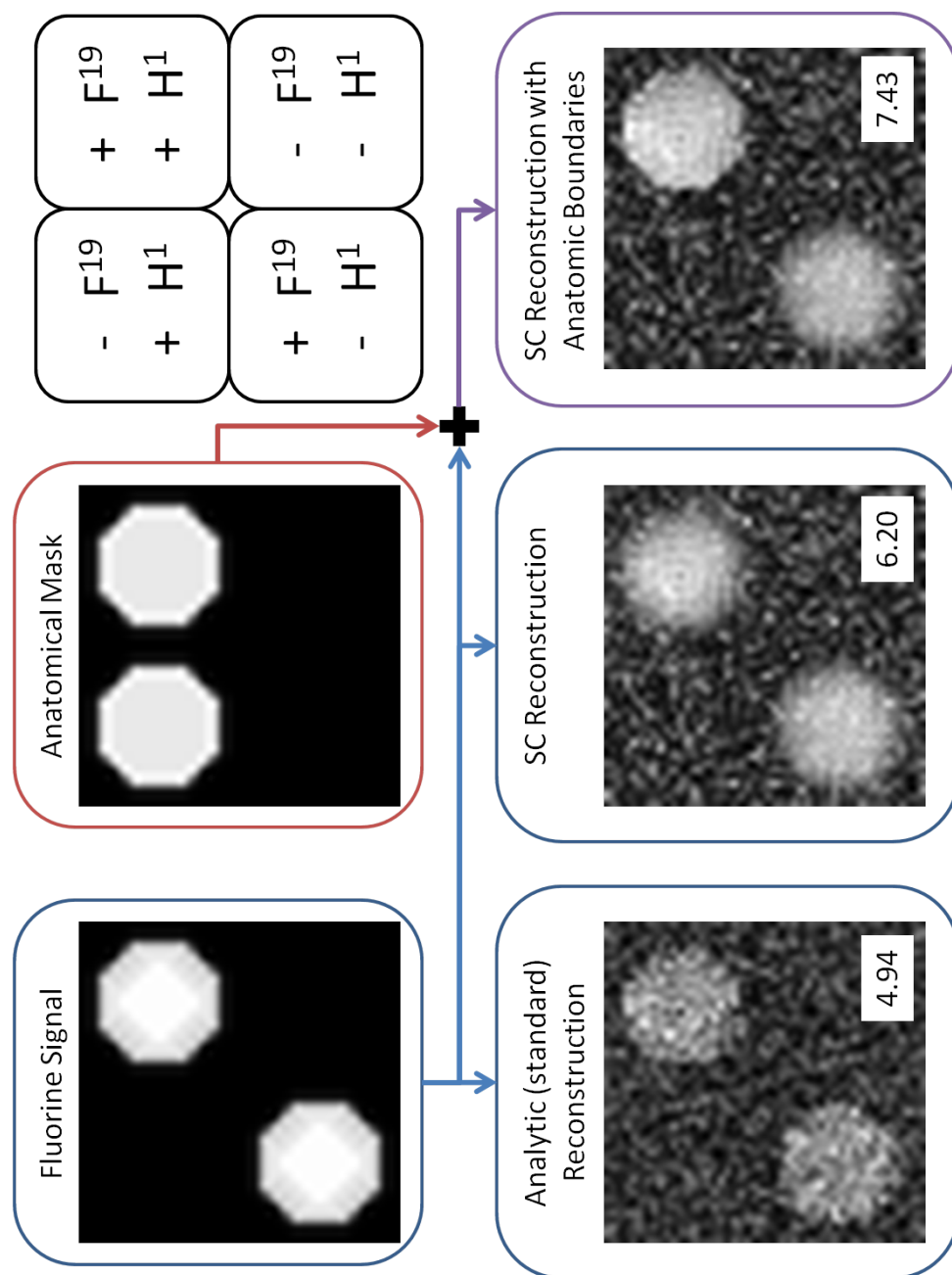
Figure 5.7: Demonstration of the principle of utilizing side information from anatomical proton scans in a heteronucleus numerical phantom reconstruction. Numbers in the bottom right of the reconstructed images are the SNR of the top-right (true-positive) region. In the case of low SNR, the standard analytic reconstruction can be improved upon by applying smoothness constraints to an iterative reconstruction, with a concurrent loss of resolution. Boundary information from a second, proton scan can be used to control smoothing across boundaries to better maintain resolution. Note that in the top-left (false-positive) region, edge constraints do not introduce artifacts where signal is not present.

5.5 *In vivo* experiments

Two *in vivo* experiments were performed to assess the utility of cardiovascular ^{19}F imaging and the advanced reconstruction methods discussed in the previous sections. First, in an experiment involving *in vivo* macrophage labeling and tracking to myocardial infarct. Imaging after MI involves a high level of acute inflammation, and thus a significant monocyte migration into the infarct in the days immediately after the MI. A second experiment was performed to attempt imaging of macrophage encroachment into atherosclerotic plaques. Atherosclerosis is a chronic inflammatory disease, rather than an acute disease. Thus, the monocyte influx into atherosclerotic plaque is significantly less per unit time than that in MI.

5.5.1 MRI equipment

All MR studies were be performed on a Siemens/Bruker Clinscan MR system. The system is equipped with a 7.0 T Bruker 30 cm bore magnet, Bruker actively shielded gradients (maximum strength of 400 mT/m, rise time of 80 μs, inner diameter = 12 cm), and a dual-tuned, transmit/receive, ^{1}H/^{19}F, volume coil insert, manufactured by Bruker, was used for fluorine imaging.

5.5.2 Animal handling procedures

Standard animal preparation techniques and NIH guidelines were adhered to for all animal studies. The mice were maintained under anesthesia using 1-2% inhaled isofluorane during all imaging sessions. The animals received constant monitoring of ECG and respiratory state

(SA Instruments), and warm water was circulated to maintain body temperature. For each imaging session, the mouse was positioned prone inside the ^{1}H/^{19}F volume coil. Using conventional proton MRI, "scout" images were obtained for positioning of the ^{19}F acquisitions, which followed.

5.5.3   Infarct Imaging

Myocardial infarction was surgically induced in C57Bl/6 mice by a one-hour occlusion followed by reperfusion. A 300 µl volume of CE nanoparticle emulsion was injected intravenously 24 hours post-surgery. Imaging was performed 4 and 8 days post-surgery to allow time for macrophage phagocytosis of nanoparticles and recruitment into damaged myocardium. For ^{19}F, a 2D TSE sequence was prescribed as closely to that described by Flögel et al. [44] as possible for comparative purposes. Scan parameters were: resolution 0.5 mm^2, slice thickness 2 mm, 3 slices, TR/TE=4500/5 ms, 256 averages, scan time 19:12 minutes, and no cardiac gating. Next, a gated 3D TSE sequence was applied with scan parameters: Resolution 0.5 mm^3, TR/TE=3000/2.5 ms, 5 averages, scan time 11:44 minutes, and the sequence was run on the subsequent cardiac trigger following wait time TR.

5.5.3.1   Image Reconstruction

Fluorine images (both 2D and resliced 3D) were reconstructed via conventional inverse Fast Fourier Transform (iFFT) reconstruction, a smoothness-constrained reconstruction (i.e. unitary edge weights, w), a constrained reconstruction with binary edge weights calculated from manually-segmented image boundaries from the proton localizer, and a constrained reconstruction with automatic calculation of edge weights from the proton localizer by the method
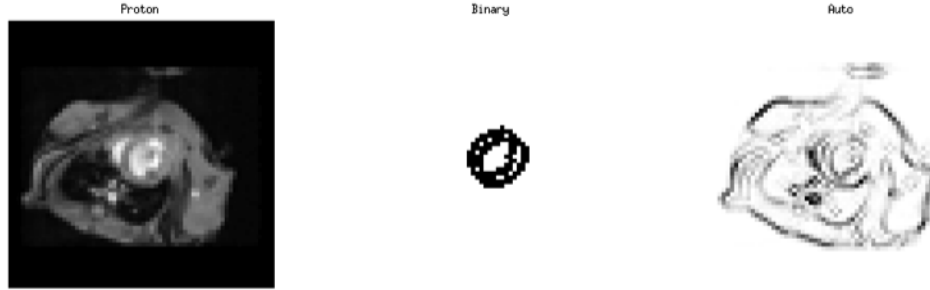
Figure 5.8: Proton localizer, binary edge weights, and automatic edge weights.

described in Section 5.4. Figure 5.8 shows the proton scout image, and the binary as well as automatically-calculated edge weights. All reconstructions were performed in Matlab and minimization of the image estimate cost function was carried out using either the iterative reconstruction toolbox from the lab of Dr. Jeff Fessler (`http://web.eecs.umich.edu/~fessler/code/`) or a modified version of the nonlinear conjugate gradient descent algorithm with backtracking line search available as part of the SparseMRI package available from Dr. Michael Lustig (`http://www.eecs.berkeley.edu/~mlustig/Software.html`). For quadratic roughness penalties, there is a well-developed theory for choosing beta in terms of the desired resolution properties of the image. Here, a slight resolution loss is desired in order to boost SNR, and we will rely on edge constraints to return resolution to a reasonable level. Here, we chose beta so that the FWHM of the PSF was equivalent to 1.3 mm (the normal mouse myocardial wall thickness is on the order of 1-2 mm), as this provided a good balance between SNR improvement while maintaining overall image quality.

In practice, binary edge weights may be blurred to account for uncertainty between anatomic and functional image registration, or due to a difference in resolution between the anatomic and functional scans [51]. Here, we downsampled the high-resolution anatomic information down to the resolution of the fluorine images prior to segmentation in order

to remove these ambiguities and use true binary edge weights. Automatic edge weight calculation was also performed on the downsampled proton images. Pixel differences were calculated in the vertical and horizontal directions.

SNR was calculated as the mean signal in the myocardium (determined from the same myocardial mask used in the masked reconstruction) divided by the standard deviation of a region outside the mouse body.

5.5.3.2 Results

In vivo results comparing the standard iFFT with the various constrained reconstructions are shown in Figure 5.9. The SNR of the myocardial region is improved in each of the smoothness-constrained reconstructions, however, boundary sharpness is better maintained through the use of edge weights. The use of binary edge weights results in slightly better performance compared to the automatic method; however, their use risks mask "bleed-through" if too-high a β value is chosen (see Fig. 5.16 for an example of this).

Figure 5.10a-d simply overlays selections from Figure 5.9 onto the proton localizer for ease of visualization. The model-based reconstruction improved myocardial SNR by 52% for the 2D image and 77% for the 3D image. Taking the 2D image as the "gold standard" in this case, we can see that the addition of edge constraints in a regularized least squares reconstruction extends the visible area of fluorine signal in the lower-SNR 3D images. Figure 5.10e is included to imphasize that the 3D technique is a "whole-mouse" technique with a much greater imaging volume than its 2D counterpart.
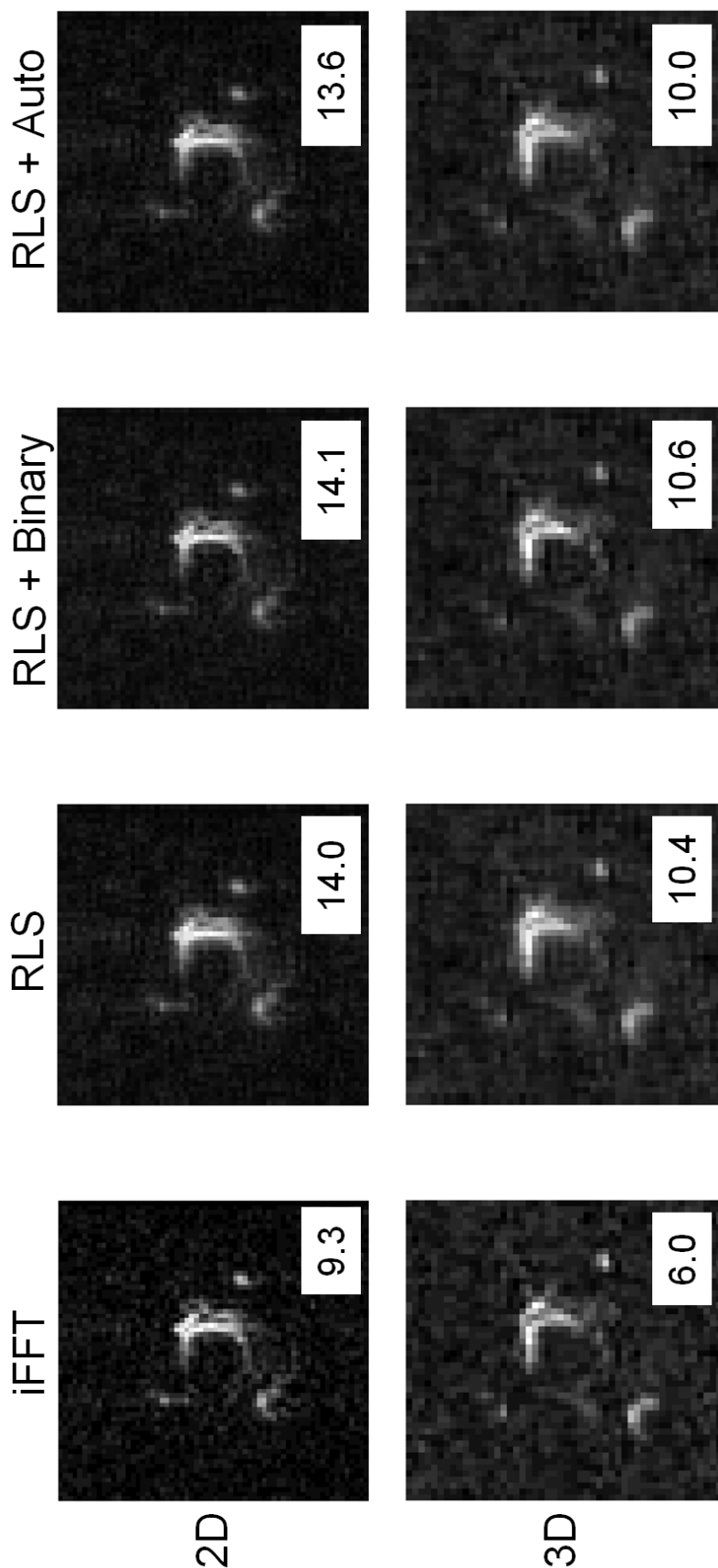
Figure 5.9: Reconstructions of ^{19}F signal *in vivo*. Fluorine signal was observed in the anterolateral myocardial wall, as expected from LAD occlusion. The 3D images have a finer resolution and required less time to acquire than multi-slice 2D. Numbers in the bottom right of the reconstructed images are the SNR of the myocardium, segmented manually from a proton scout image. Additional boundary constraints upon the regularized least squares (RLS) reconstruction maintain high SNR, and mitigate the blur associated with smoothness-constrained reconstructions. Unequal voxel size and acquisition duration is the cause of differing SNR between the two datasets.
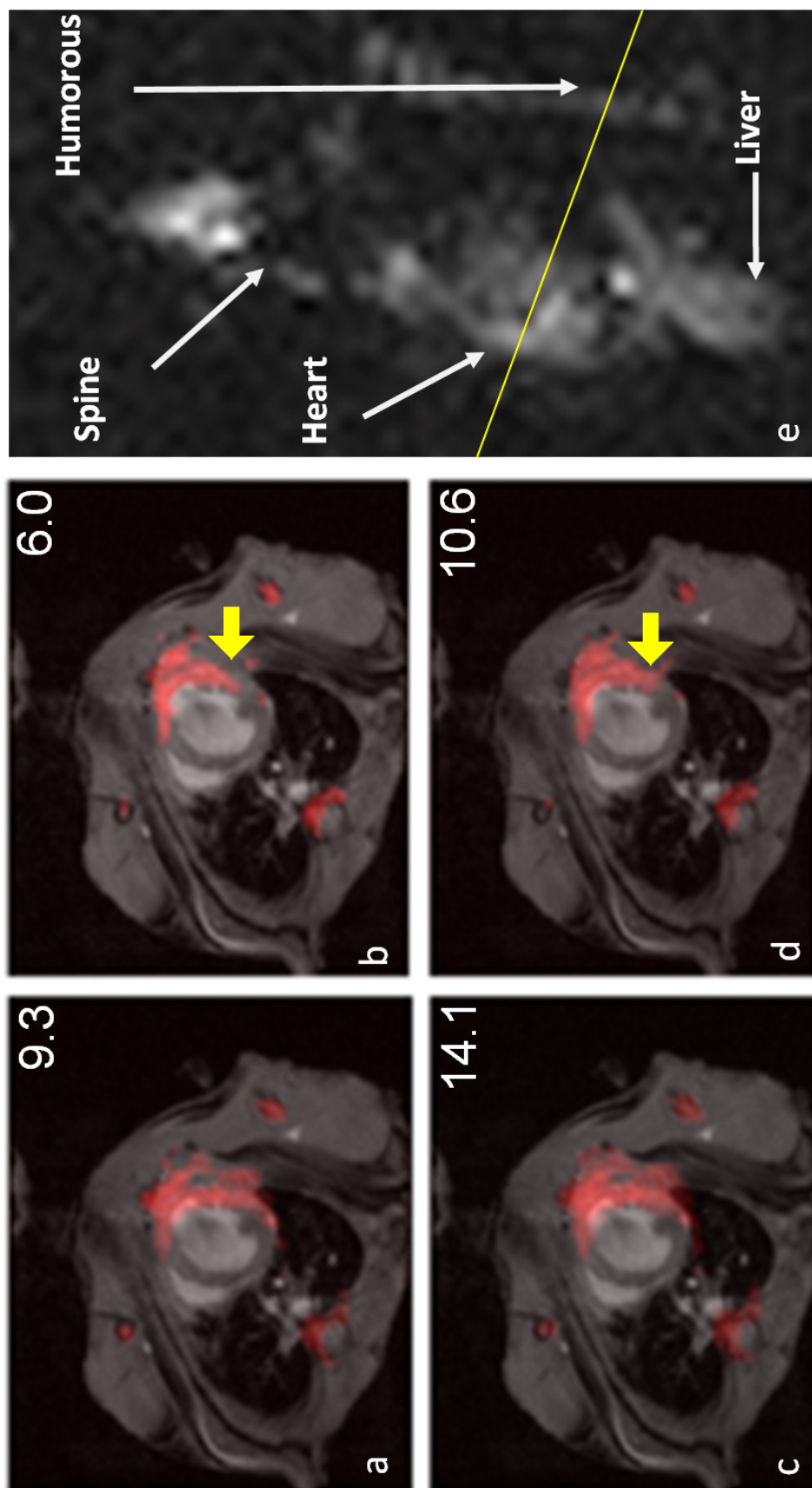
Figure 5.10: Macrophage tracking with fluorine nanoparticles in an infarct model. a) 2D TSE fluorine scan (red) overlaid on proton localizer. b) 2D reslice from 3D TSE fluorine scan. c) Regularized 2D reconstruction incorporating boundary information. d) Regularized 3D reconstruction. e) Coronal MIP of 3D TSE fluorine scan showing 2D reslice location for (b and d). Macrophage uptake of the nanoparticle formulation used in this work is also observed in the liver and bones. Note that the regularized 3D reconstruction shows a greater fluorine signal extent, which better matches 2D data.

5.5.3.3   Conclusion

To our knowledge, this is the first implementation of gated 3D whole-mouse ^{19}F imaging. The sensitivity advantage of 3D encoding allowed a greater volume to be imaged in less time than multi-slice 2D, with similar image quality. Gating is necessary to mitigate artifacts from cardiac and respiratory motion. The use of whole-mouse imaging allowed observation of contrast accumulation in the spine and long bones; this result was unanticipated and may have gone unappreciated without large volume imaging.

This is the first use of anatomic side information from proton images to assist the reconstruction of MRI of heteronuclei. Binary weights resulted in the best image quality and SNR; however, their use requires manual intervention and can cause artifacts if too much smoothing is applied between regions that both contain fluorine signal. Automatic weights perform nearly as well in recovering SNR, but rely on good contrast between tissues of interest in the proton images used for weight calculation.

5.5.4   Atherosclerosis Imaging

The 3D TSE sequence and model-based reconstruction techniques were also applied to a particularly low-SNR imaging test: macrophage imaging in atherosclerotic plaques. Six apolipoprotein-E-knockout (ApoE) mice were fed a high-fat diet for 12 weeks. At the end of week 10, two mice were imaged with the protocol described below to act as controls. In weeks 11 and 12, all mice received a 100 µl injection of PFC nanoparticles once every 3 days. At the end of the 12-weeks, the mice received a 300 µl large-dose injection of nanoparticle solution. The nanoparticle formulation was identical to that described in Section 5.2, with

the addition of a fluorescent marker, DiI, into the lipid shell.

Imaging was performed on days 1 and 8 post-large-dose-injection. Because the proximal aorta is tethered to the heart and lungs, cardiac and respiratory gating was used to freeze motion that may have otherwise interfered with fluorine signal acquisition. The 3D TSE sequence was used to acquire volumetric ^{19}F data with 0.9 mm^3 resolution extending over the entire abdomen of the mouse (the effective coil volume in z of our ^{19}F/^{1}H coil is approximately 40 mm). TR/TE was 3000/2.1 ms, and acquisitions were segmented in order to reduce echo train lengths such that they could fit into an R-R interval of a mouse's heartbeat (approximately 80 ms). Since the accumulated PFC volume was expected to be small, 36 averages were used. Total scan time was 1 hour. The same sequence was used to acquire high-resolution 3D ^{1}H data with 230 μm^3 resolution. TR/TE was 500/39 ms, and again, acquisitions were segmented in order to reduce echo train lengths appropriately. Strong crusher gradients were applied on all three gradient axes in order to spoil flow and thus form black-blood images. This is a new technique for black-blood imaging in mice with large volumetric coverage, and has many potential applications outside of this work.

Following the large-dose injection, mice were allowed to recover for 1 (3 mice) or 7 days (3 mice) before being sacrificed. Tissue from the heart, aorta, liver, lung, spleen, and bone marrow was collected. The hearts and aortas were placed in a saline solution, and two at a time, imaged with a ^{19}F 2D TSE sequence with TR/TE 2000/4.8 ms, 1.25 mm^2 resolution, 10 mm slice thickness, and 512 averages (scan time 34.2 min). Additionally, a ^{1}H TSE sequence was run with TR/TE 500/5.7 ms, 78 μm^2 resolution, 10 mm slice thickness, and 1 average (scan time 4.7 min).

^{19}F images were reconstructed by a conventional iFFT, a smoothness-constrained re-
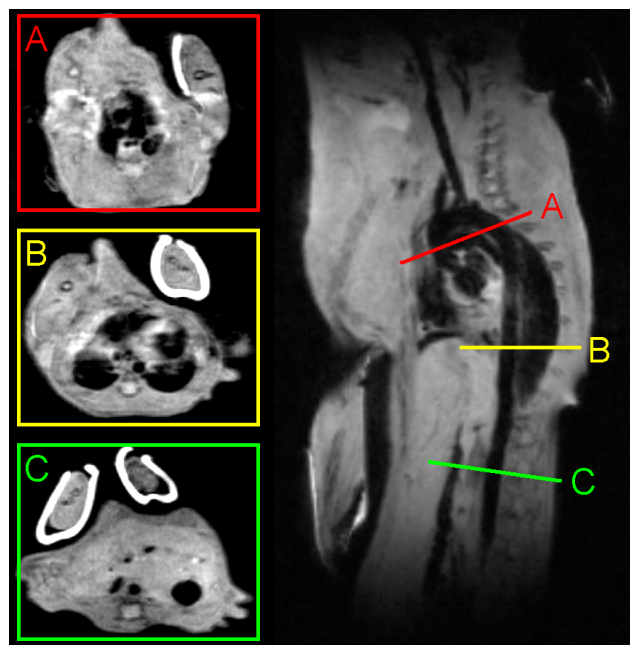
Figure 5.11: Volumetric black blood imaging using a 3D TSE sequence with large spoiling gradients to dephase blood signal. Heart- and respiratory-gating is used to minimize artifact from motion, and segmented acquisition of k-space is used in order to shorten echo trains such that a single echo train may fit into the diastolic portion of a mouse heart cycle (approximately 80 ms). Isotropic resolution of $230\,\mu m^3$ was obtained in approximately 5 minutes. A) 2D reformat of 3D data showing ascending and descending aorta, where atherosclerosis is known to occur in disease models. B) Slice from thoracic aorta. C) Slice from abdominal aorta.

construction, and a constrained reconstruction with binary edge weights calculated from manually-segmented proton images. The SNR of the resulting images was calculated as the mean signal inside of the manually-masked portions of the image (heart and aorta) divided by the standard deviation of the noise.

Each tissue harvested was then imaged using fluorescence microscopy to identify DiI fluorescence, indicative of nanoparticle accumulation. Sections with positive DiI signal were stained with anti-CD68, a marker for macrophages.

5.5.4.1 Results

Figure 5.11 shows a black-blood abdominal image from one mouse. Excellent blood suppression was achieved throughout the aorta, with no complex preparatory pulses and with no increase in scan time. Prior to nanoparticle injection, no ^{19}F signal was found in the control mice, as expected. Post-injection, ^{19}F accumulation was observed in all mice in the tissues of the MPS; however, no signal was detected in the *in vivo* aortas.
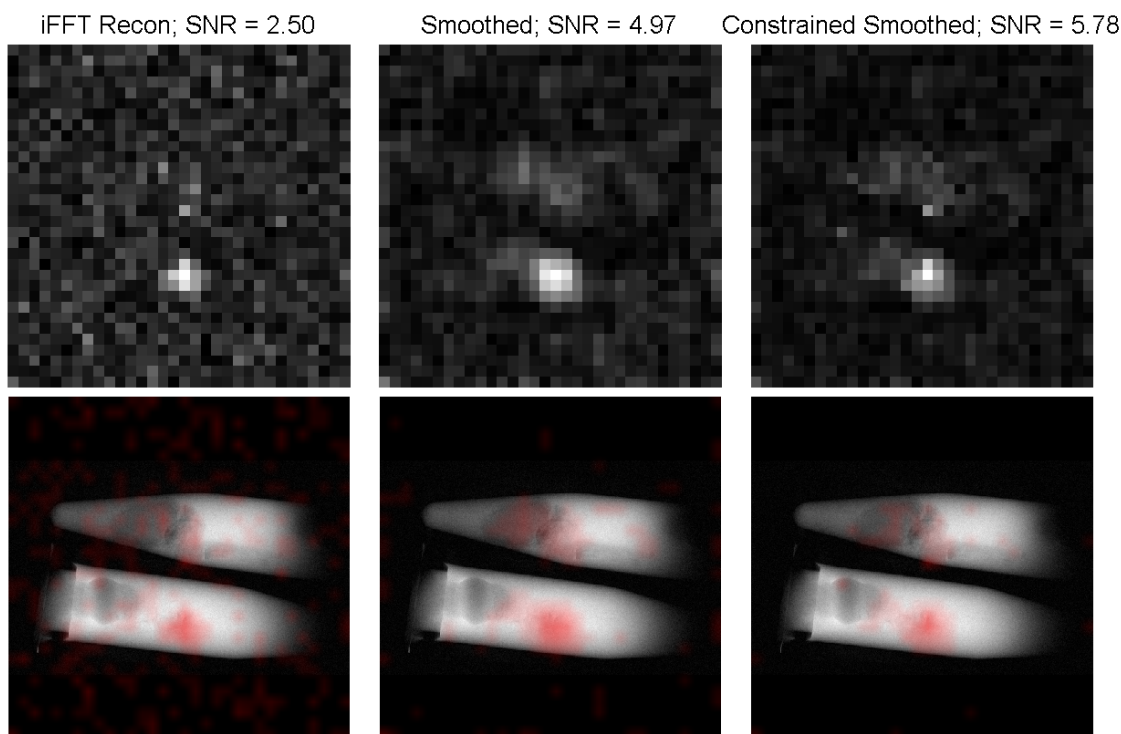
Figure 5.12: *Ex vivo* imaging of atherosclerotic hearts and aortas from 2 mice with different reconstructions. ^{19}F images are merged with ^{1}H images in the bottom row to show ^{19}F signal in heart/aorta tissue.

In Figure 5.12, however, it is clear that ^{19}F nuclei are present in the hearts and aortas of the mice, indicating at least some accumulation of contrast agent in these tissues. Model-based reconstructions improve the images as discussed previously, by locally improving SNR. The improvement is especially apparent in the upper heart in this figure, where virtually no signal is observable above the noise in the iFFT reconstruction, but is clearly present in the model-based reconstruction results. No difference was observed between mice sacrificed at 24 hours versus those sacrificed at 7 days, consistent with the long organ retention time of CE.

Co-localization of DiI and CD68-positive macrophages is shown in Figures 5.13 and 5.14. The positive co-localization shown in Figure 5.13 provides an explanation for the marrow signal seen in Figure. 5.10e; namely, that marrow monocytes participate in particle uptake
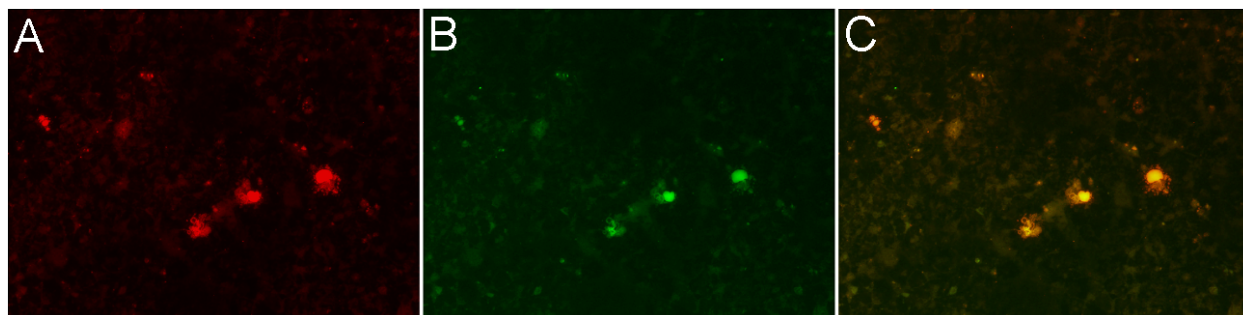
Figure 5.13: Histological images of bone marrow showing (A) fluorescent-dye-containing nanoparticles, (B) CD68-positive monocytes, and (C) co-localization of the two.
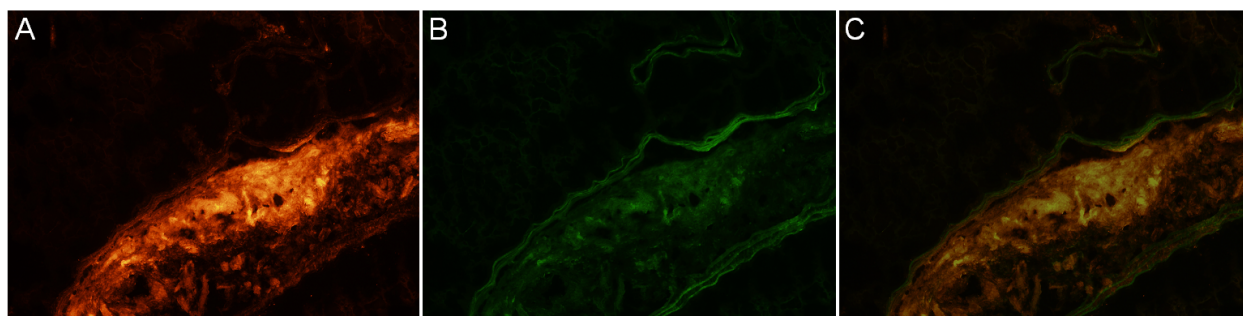
Figure 5.14: Histological images of atherosclerotic plaque showing (A) fluorescent-dye-containing nanoparticles, (B) CD68-positive monocytes, and (C) co-localization of the two.

along with other phagocytotic cells of the liver and spleen. In Figure 5.14, the presence of macrophages in the atherosclerotic plaque along with DiI nanoparticles supports the hypothesis that the ^{19}F signal observed in Figure 5.12 is actually bound to and resides within atherosclerotic plaques of the aortic wall and valve.

5.5.4.2 Conclusion

Co-localization of DiI and anti-CD68 in Figs. 5.13 and 5.14 is consistent with the hypothesis that *in vivo* labeling occurs via macrophage uptake of ^{19}F nanoparticles in the blood stream and/or MPS and the subsequent migration of these cells into tissues. While we were unable to observe ^{19}F signal *in vivo*, its presence was confirmed with *ex vivo* imaging and immunohistochemistry. Consistent with our previous findings, the alternative use of model-

based reconstructions can improve these images to the point where ^{19}F signal rises above the noise floor, improving the sensitivity of ^{19}F imaging. Furthermore, the additional constraints provided by proton images resulted in even higher SNRs while reducing the amount of blurring.

5.6   Model-based Reconstruction Methods, Revisited

We have shown that the pixel-based regularization methods described in Section 5.4 are capable of improving local SNR while maintaining image resolution and thus, improving the sensitivity, of ^{19}F imaging. However, while we have shown that the addition of edge constraints helps, these methods are fundamentally limited by the amount of smoothing that can be applied before image quality is degraded. In this section, two additional regularization approaches are described.

5.6.1   Regularization towards a reference

A very simple regularization choice (even simpler than the quadratic penalty of Eq. 5.2) is to bias the reconstruction towards some reference image, $\overline{f}$. The regularizer is defined as:

$$R(f) = \|f - \overline{f}\|^2 \tag{5.4}$$

This regularizer is a form of Tikhonov regularization. As $\overline{f}$ is often neglected altogether in practice, the resulting image estimate is biased toward zero, possibly reducing image contrast [87]. However, by carefully choosing the reference image, improved results may be obtained.

Here, we will adopt the strategy proposed by Rousseau [86], and use a denoised version

of the image as the reference image:

$$\overline{f} = d(f) \tag{5.5}$$

where $d(f)$ is the image denoised with some algorithm, of which there are many to choose from. One relatively recent denoising algorithm that lends itself easily to the possible incorporation of side information is the the non-local means filter, described below.

5.6.1.1   The Non-Local Means (NLM) Filter

Example-based denoising methods assume that a local image patch should look similar to a weighted sum of some patch dictionary entries which can fully describe image features. These dictionaries can be trained beforehand, on previously acquired images, or they can be trained using the noisy image itself. The non-local means filter belongs in the latter category, and works on the principle that any local image patch should look similar to other image patches present in the same image [88]. Each patch, x, is therefore reconstructed as a weighted summation of other patches in the search window, V:

$$NLM(x) = \sum_{i \in V} w(i,j)x_i \tag{5.6}$$

The degree of similarity, and thus the summation weight, w, between patches i and j is determined by the Euclidian distance between the gray levels of the patches:

$$w(i,j) = \frac{1}{Z(i)} e^{-\frac{\|x_i - x_j\|_2^2}{h^2}}, Z(i) = \sum_{j} w(i,j) \tag{5.7}$$

where h is a filter parameter related to the noise variance.

In order to pull side information into the algorithm and apply the filter to low-SNR ^{19}F data (which does not contain much spatial information), we can first deploy the training step of the filter on a high-SNR, high-spatial-information proton image. The calculated filter weights are saved and then used to guide the fluorine filter by describing, for any individual patch, which other patches in the (fluorine) image should be similar and how to combine them. Figure 5.15 illustrates the process using a numerical phantom example. In this way, Equation 5.6 is modified such that:

$$NLM(x, y) = \sum_{i \in V} w_y(i, j) x_i \tag{5.8}$$

that is, each patch in the fluorine image is reconstructed as a weighted summation of other patches in the image, but the weights are derived from an anatomical proton image.

The simple approach presented in Equation 5.8 and Figure 5.15 assumes local image patterns in the proton image can be directly used as examples for the fluorine reconstruction. Since there are conceivably cases where this may not hold true, and to minimize artifacts due to the NLM filter itself, we instead use the side-information-trained NLM filtered image as the reference image described in the previous subsection. Putting it all together, the cost function to be minimized is:

$$\hat{f} = \arg\min_{f} \ \|y - Af\|^2 + \beta \|f - NLM(f, p)\|^2 \tag{5.9}$$
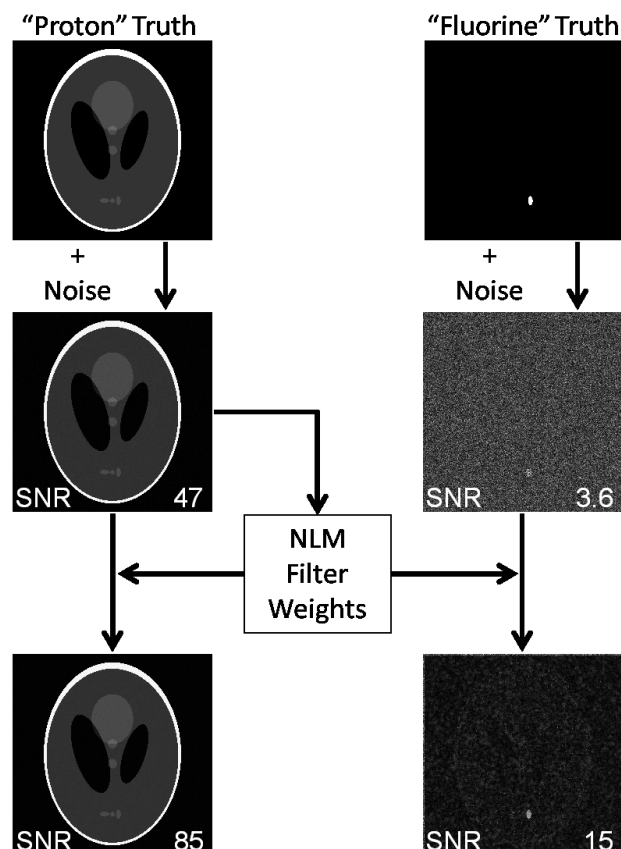
Figure 5.15: Second-nucleus denoising using primary anatomic information. Filter weights are derived from the high-SNR, high-spatial-information "proton" image and then applied to the low-SNR "fluorine" image. The SNR values are for the small positive-valued ellipse visible in the fluorine truth image.

5.6.2 Sparsifying constraints

The low SNR of ^{19}F images lends one to naturally wish to apply denoising methods in a post-processing step to the resulting images; however, denoising low SNR data can be difficult when image features (edges) compete with local intensity gradients due to noise. Compressed sensing has emerged as a method by which an image may be reconstructed from non-Nyquist-sampled data by exploiting sparsity [89]. Its major application in MRI has been to speed up acquisitions by reducing the amount of data that must be acquired to generate a useful image. However, the technique can also applied to image denoising as the sparsity constraint imposed by the reconstruction naturally suppresses noise-like signal. By virtue of there being no detectable background signal, ^{19}F images are naturally sparse,

lending themselves to image-domain constraints on sparsity. As described in Lustig et al.
[89], we can apply both an L1-norm penalty as well as a total-variation penalty to the cost
function in order to enforce sparsity:

$$\hat{f} = \arg\min_{f} \|y - Af\|^2 + \beta_1\|f\|_1 + \beta_2\|Cf\|_1 \tag{5.10}$$

where we recall that C is a differencing matrix. Enforcing sparsity may improve image quality
through denoising, but on its own, does not utilize side information to guide this denoising
process. We hypothesize that a combination of sparsifying constraints plus side-information
constraints will yield high-quality reconstructions.

5.6.3   Methods

To first test the NLM algorithm in Matlab using numerical phantoms, the full Shepp-Logan
phantom with a small amount of added noise stood in for our "proton" image, and a second
image with only a small non-zero ellipse with a large amount of added noise stood in for
a "fluorine" image. The side-information-trained NLM filter was first applied naïvely; that
is, the filter weights were trained using the proton image and then applied directly to the
fluorine data. Next, to compare all of the regularization methods discussed, the phantoms
were reconstructed using:

1. A standard iFFT reconstruction.

2. A side-information-constrained quadratic smoothness regularizer, as described in Sec-
   tion 5.4. The edge weights were determined from an edge detection function, $edge()$,
   available in Matlab from the fluorine "truth" image. This mimics manual segmentation

of the proton image.

3. A reconstruction biased towards a denoised version of the iFFT image. The denoising
   algorithm used was NLM using the proton image to train the filter weights.

4. A sparse reconstruction with an L1-norm penalty as well as a total-variation penalty
   (as described in [89]).

5. A combination of the penalties from reconstructions 3 and 4.

For reconstructions 2-4, the penalty weights were adjusted such that the SNR of the
positive region was approximately the same. The SNR, RMSE between the reconstructed
image and the true image, and the sharpness of the image, as determined by the mean
gradient across the positive ellipse, was recorded.

In order to demonstrate the ability of model-based reconstructions to recover signal from
low-SNR data, the 2D TSE myocardial data from Section 5.5.3 (which was collected with
256 averages) was iFFT reconstructed with 256, 128, and 64 averages. For the 128- and
64-averages data, images were also reconstructed using reconstruction #5, described above.
The number of pixels positive for ^{19}F was recorded as a surrogate for detection sensitivity,
with the 256-average iFFT reconstruction image used as the gold standard. A pixel was
considered positive for ^{19}F if its value exceeded 4 standard deviations of the noise.

5.6.4 Results and Conclusions

In addition to showing the process, Figure 5.15 also presents evidence that the naïve applica-
tion of the side-information-trained NLM filter can improve image quality of noisy ^{19}F images
by improving the SNR of the small, non-zero image feature nearly five-fold. It was found

that the sizes of the local search window as well as the patch size had a strong impact on the result. For standard image denoising of the proton image, a search window of 9 x 9 with a patch size of 3 x 3 resulted in good denoising without artifacts. However, when these parameters were applied to noisy fluorine data, image features from the proton image became visible as variations in noise texture. Reducing the search window to 5 x 5 and the patch size to 1 x 1 alleviated this effect.

All four constrained reconstruction methods are shown in Figure 5.16. From this figure, it is clear that all model-based reconstructions out-perform a simple iFFT reconstruction. The main disadvantage of the edge-information-constrained quadratic smoothness regularizer is visible in this figure; namely, the edge mask bleed-through artifact described previously. In Subfigure 5.16E, it is apparent that biasing the reconstruction towards a denoised version of the iFFT reconstruction is a promising method; however, close scrutiny reveals image features from the proton image visible as variations in noise texture throughout the image. The result of applying sparsity constraints to the reconstruction are shown in Subfigure 5.16F. While good results are obtained, this reconstruction utilizes no side-information from the "proton" image, and thus fails in the top-most portion of the ellipse where random noise variations have suppressed signal. Finally, combining the sparsity constraints with a bias towards a denoised image appears to give the best results. These results are quantified in Table 5.2.

The results of the constrained reconstruction on *in vivo* data is shown in Figure 5.17. Lowering the SNR by reconstructing the image with fewer averages has the expected effect of reducing the number of positive ^{19}F pixels (Table 5.3). The model-based reconstruction successfully recovers many of the "lost" pixels.

These results indicate that for low-SNR ^{19}F data, iFFT reconstructions can be improved
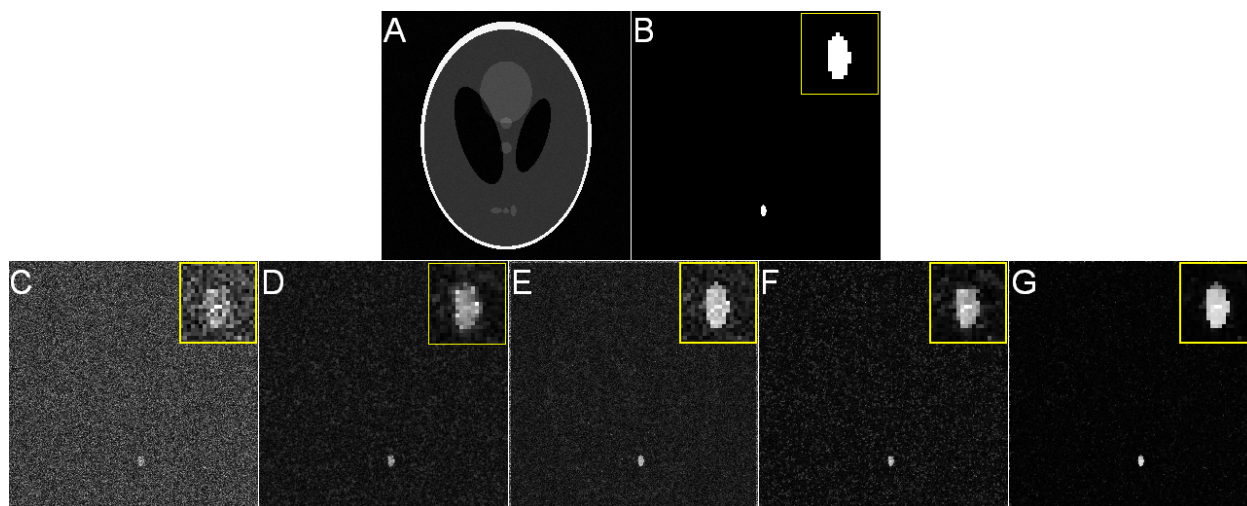
Figure 5.16: Constrained model-based reconstructions in a numerical phantom. A) "Proton" image with a slight amount of added noise. B) True "Fluorine" image. C) iFFT reconstruction after adding complex noise to Fourier-transform of (B). D-G) Model-based reconstructions with: D) edge-information-constrained quadratic smoothness regularization (as described in Section 5.4); E) Regularization bias with a non-local means denoised version of (C) used as the reference image; F) Sparsity constraint; G) Sparsity plus Bias. Insets are zoomed-in segments of positive "fluorine" signal.

Phantom Reconstructions			
Reconstruction	SNR	RMSE	Sharpness
iFFT	4.23	5.65	1.12
Smoothness	12.2	1.72	0.72
NLM	12.3	2.09	0.82
Sparsity	12.2	0.88	0.46
Sparsity + NLM	40.8	0.31	0.60

Table 5.2: Quantification of images in Fig. 5.16. RMSE is the error between the reconstructed image and the noise-free, true image. The ideal sharpness value is 1 (the iFFT reconstruction's sharpness exceeds this due to noise).

Number of Positive ^{19}F Pixels			
Reconstruction	256 Averages	128 Averages	64 Averages
iFFT	739	380	177
Model		913	369

Table 5.3: Number of positive ^{19}F pixels in the reconstructions of Fig. 5.17. A positive pixel is one with a value greater than 4 standard deviations of the noise.

upon by exploiting additional information we have about the image. Namely, we have used spatial information derived from the concurrently-acquired proton images through edge constraints on smoothing penalties and by using the anatomical information to train denoised versions of ^{19}F images, which are then biased towards in the reconstruction. We have also leveraged more esoteric information regarding image sparsity into ^{19}F reconstructions through the application of sparsity constraints.

5.7   Discussion and Conclusions

Based on the results summarized in Figure 5.5, we believe that 3D TSE with cardiac and respiratory gating is a highly efficient pulse sequence for cardiovascular ^{19}F imaging, and subsequently used it for all *in vivo* imaging experiments. The long T_2 of CE means that relatively long echo trains can be used without losing signal. We used a centric-out reordering scheme with the first echo assigned to the center of k-space because we do not wish to generate contrast in our ^{19}F images; we simply wish to maximize signal with a long TR and short TE (i.e. our ^{19}F images are fluorine-density weighted).

We have shown that SNR can be improved over a standard reconstruction through model-based reconstruction methods that incorporate prior knowledge into the reconstruction. Constrained smoothness regularizers average signal locally and use edge information to regain
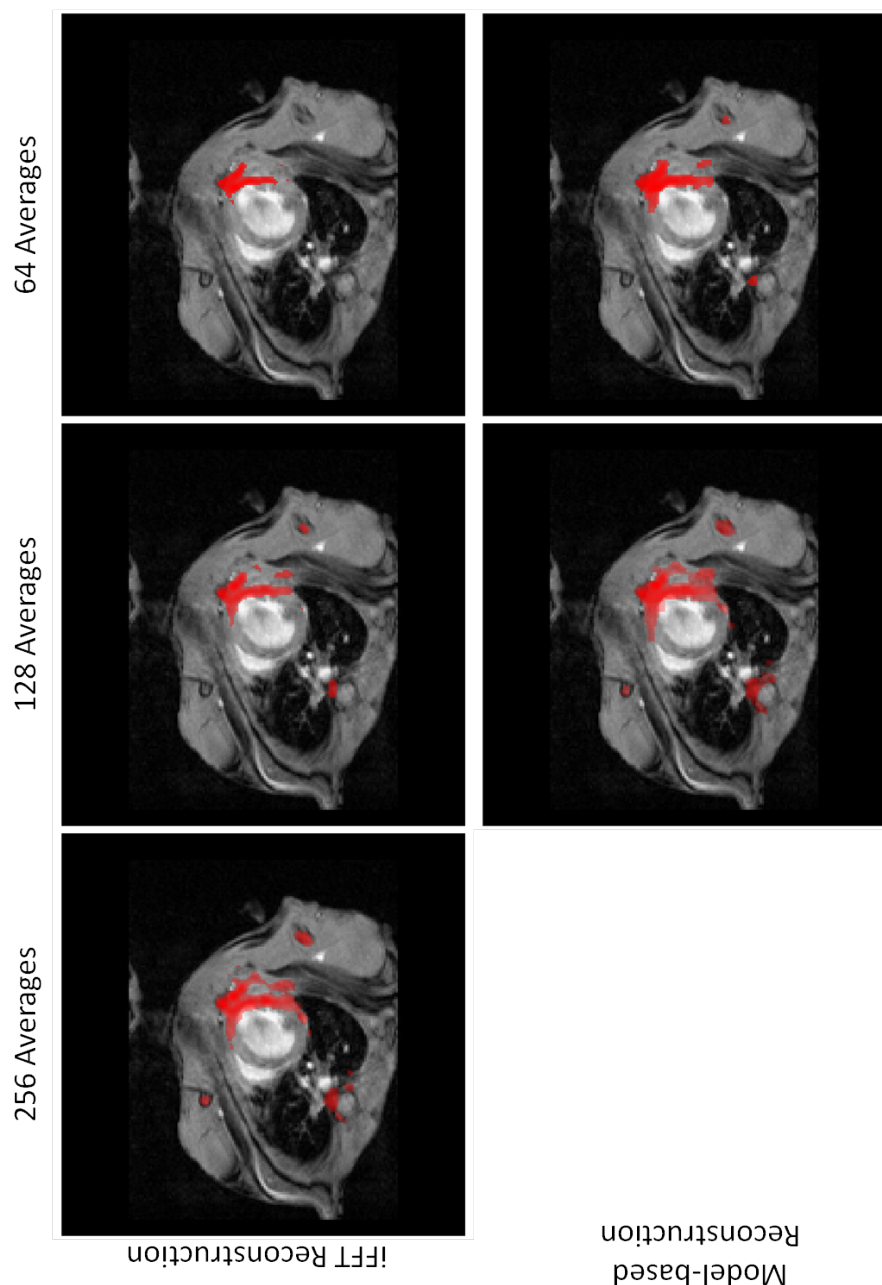
Figure 5.17: Reconstructions of *in vivo* data with varying SNR. Lower SNR results in a loss in sensitivity to ^{19}F nuclei when using the traditional iFFT reconstruction (top row). The use of a model-based reconstruction which takes anatomic side information into account is capable of recovering some of this "lost" signal.

some of the resolution loss incurred by the smoothing. Biasing the reconstruction result towards a denoised version of the image can be effective, and we have shown that incorporating side information through the denoising algorithm can be effective. Finally, the natural sparsity present in ^{19}F images can be exploited to further improve image quality. As we showed, these constraints need not be applied individually; better results can be obtained by combining multiple regularization methods.

In vivo, the use of automatic weights requires good contrast in the proton images between tissues where fluorine is expected and where it is not. By studying Figures 5.8 and 5.9, it is clear that the infarcted region of the myocardium unfortunately had the least amount of contrast with surrounding tissue, resulting in blurring of the ^{19}F signal in that area. In the future, intelligent choices of what kind of proton scan(s) to perform alongside the fluorine scan will become important for this reason. For example, a high-resolution late-gadolinium-enhanced image or T$_2$-weighted edema image of the myocardium could have been used here to further restrict the fluorine reconstruction to the infarct zone.

van Heeswijk et al. [90] showed that *in vivo* imaging of fluorine nanoparticle accumulation in atherosclerotic plaque is possible; however, we were unable to replicate their results (their experiments were performed at 9.4 T, whereas ours was performed at 7.0 T). Through Figures 5.12 and 5.14, we have strong evidence that our ^{19}F nanoparticles were successfully delivered into atherosclerotic plaques via macrophage trafficking. The failure to detect ^{19}F signal *in vivo* is therefore due to poor sensitivity and may be due to the imaging protocol chosen, nanoparticle design, or physiology. From an imaging perspective, low sensitivity may be due to partial volume effects (voxel sizes were on the order of 1 mm^3), much larger than plaque sizes. Our nanoparticles may not be as aggressively taken up by macrophages when

there isn't an acute inflammatory response, as there is in MI, or the atherosclerotic plaques weren't as large as needed for sufficient ^{19}F accumulation.

In addition to their possible use in clinical settings, robust molecular and cellular imaging methods already have great utility in preclinical work. Questions regarding when and how genes, proteins, and cells are activated in response to various physiological stimuli can be investigated directly *in vivo*. The ability to observe cellular and molecular activities *in vivo* is a powerful tool in gaining understanding of normal and abnormal functions of the body on the smallest scale and has impact in virtually every field of medicine. As discussed, second-nucleus imaging with MR, and in particular ^{19}F imaging, is a promising method that shares some properties with multi-modality imaging systems such as PET- and SPECT-CT and -MR, without the use of probes ionizing radiation or toxicity concerns .

Chapter 6

Conclusion

6.1 Overview of Findings

As stated in the introduction chapter of this dissertation, the recurring theme of this work was the TSE sequence and how it may be modified for MRI of long-T_2 species for cardiovascular imaging, specifically blood with its long (and variable) T_2 and the ^{19}F nucleus, whose T_2 when incorporated into CE is on the order of 1 s. Chapters 2, 3, and 4 specifically addressed the development of new techniques for the diagnosis of clinically relevant (i.e. late-stage) atherosclerosis in the peripheral vasculature, while Chapter 5 focused on developing new methods for imaging early-stage atherosclerosis in mouse models and is therefore relevant for pre-clinical exploration of disease progression. Prior to these chapters, we briefly described the clinical problem of PAD, along with some current methods for non-contrast-enhanced MRI, the TSE sequence, and spiral imaging. We also described the advantages ^{19}F imaging offers for cellular and molecular imaging, particularly for inflammatory diseases such as atherosclerosis. The low sensitivity of MRI in this setting provides impetus for the gated TSE sequence's use here as well as for advanced reconstruction techniques.

Chapter 2 introduced the rTSE sequence: a new, hybrid pulse sequence that shares characteristics with TSE and bSSFP sequences. The principles of FIA in the context of this new TSE sequence, including a description of tissue contrast properties, was described and illustrated using Bloch equation simulations, phantom experiments, and volunteer data. An image quality comparison based on SNR, contrast, and vessel sharpness between the rTSE sequence and a traditional TSE sequence was presented in normal volunteers, with the rTSE sequence providing better contrast and sharpness than its traditional counterpart. In patients, despite substantially reduced contrast (compared to volunteers), the rTSE sequence was able to positively identify stenoses observed with more traditional vascular imaging methods. Additionally, a method for fat/water separation based on phase detection was presented for this application.

In Chapter 3, the 3D Cartesian TSE sequence was modified to utilize spiral readouts in order to take advantage of some of the unique properties afforded by non-Cartesian imaging. In particular, the sequence developed in Chapter 2 results in images that suffer from venous contamination; the longer echo spacings afforded by spiral readouts were shown to shorten the effective T_2 of venous blood through Bloch equation simulations and volunteer data. Additionally, the rTSE sequence suffers from insufficient fat suppression due to stimulated echoes arising from non-ideal refocusing pulses. We showed that returning crusher gradients to the sequence in the anterior-posterior direction, along with standard fat suppression methods, was sufficient to remove fat signal from the resulting images while maintaining flow insensitivity in-plane.

During sequence development, a particular resistance to off-resonance blurring of so-called redundant spiral-in/out gradients was discovered. Chapter 4 described this finding in detail.

In short, for a given total readout length, spiral-in/out trajectories result in approximately half of the off-resonance phase accrual that spiral-out trajectories accrue. That is, they can tolerate twice the off-resonance of spiral-out scans before significant blurring occurs. Furthermore, by traversing k-space "redundantly," spiral-in/out artifacts related to T_2 decay and phase accrual during the readout are removed. These findings were elucidated through simulations and verified with phantom and *in vivo* imaging experiments.

Our focus shifted to the development of second-color MRI methods for imaging inflammation in myocardial infarction and early-stage atherosclerosis in Chapter 5. An SNR efficiency comparison between common ^{19}F MRI sequences was presented, and it was determined that a gated 3D TSE sequence is a good choice for ^{19}F imaging due to its high sensitivity and resistance to artifacts. Additionally, several implementations of model-based iterative reconstruction techniques designed to improve the quality of low-SNR ^{19}F images by incorporating boundary information derived from accompanying proton images was presented. Two experiments involving *in vivo* macrophage labeling with ^{19}F nanoparticles were presented. In the context of imaging inflammation in MI, we compared the 3D TSE sequence with an ungated 2D sequence reported in the literature. We were able to successfully image inflammation in MI using our methods, and our sequence achieves comparable image quality with greater coverage and in less time than the 2D sequence. In the second experiment, we successfully labeled atherosclerosis in mice using our nanoparticles, and were able to spatially resolve ^{19}F accumulation in *ex vivo* imaging. The use of strong crusher gradients in the 3D TSE sequence for dark-blood imaging in mice is new, and supports whole-mouse dark-blood imaging with applications extending outside of this work. Furthermore, we showed that using model-based reconstruction techniques improves sensitivity of ^{19}F imaging by locally

improving SNR for both experiments.

6.2 Future Directions
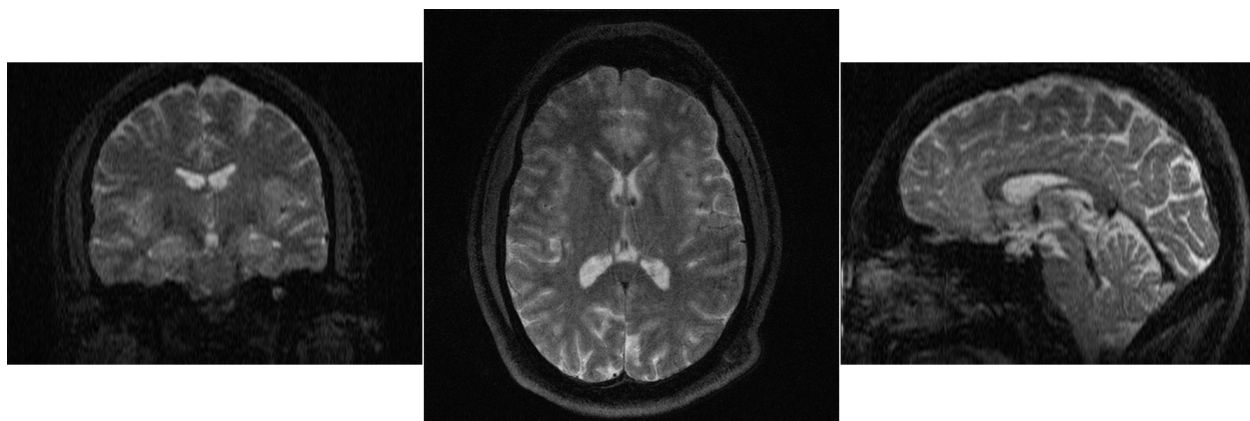
6.2.1 Spiral SPACE

Aside from angiography, the spiral SPACE variant of the 3D spiral TSE sequence has potential applications in other imaging settings, particularly in the abdomen and brain. Current methods to produce T_2-weighted abdominal images are prone to motion artifacts arising from bowel peristalsis, and the natural motion insensitivity of spiral gradients may have advantages here.

In the head, the efficiency of spiral acquisitions shows promise for fast brain imaging. Recently, a segmented version of the sequence was used to obtain T_1 weighted images of the brain with an isotropic 3D resolution of 1.7 mm^3 with an acquisition time of only 30 seconds. (Fig. 6.1). For this scan, TR/TE = 900/32ms, ETL = 32. Dual-density spiral undersampling with 2.4X acceleration was used in-plane (9 interleaves) and no undersampling was performed through-plane. Images were reconstructed using 2D SPIRiT with a semi-automatic off-resonance correction applied using field maps acquired as part of the scan to each slice. Normally, a TSE sequence would not be used to obtain such contrast. It must be noted that the acquisition time was imposed by an external agency and is not an inherent limitation of the sequence. Given a longer acquisition time and the implementation of techniques designed to improve the T_1-weighting capability of the SPACE sequence [91], better resolution and contrast may be obtained.

T_2-weighting is, of course, the more natural form of contrast to image using the SPACE
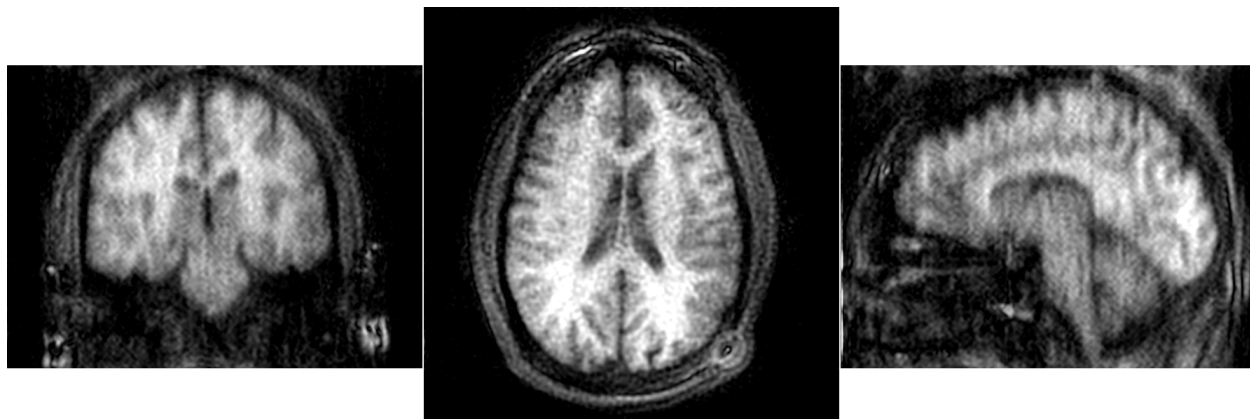
Figure 6.1: T_1-weighted isotropic 3D resolution brain image obtained with the spiral SPACE sequence acquired in 30 seconds.

Figure 6.2: T_2-weighted 3D brain image obtained with the spiral SPACE sequence acquired in 59 seconds.

sequence. Figure 6.2 shows an example spiral SPACE T_2-weighted brain image. For this scan, TR/TE = 3s/327ms, ETL = 81. Resolution = 0.65mm^2 in-plane achieved with 4X dual-density spiral undersampling (17 interleaves); 2-mm through-plane achieved with 15% partial-Fourier. Images were reconstructed using 2D SPIRiT with a semi-automatic off-resonance correction applied using field maps acquired as part of the scan to each slice. Total scan time was 59 seconds.

6.2.2 Further sequence development and optimization for ^{19}F imaging

An exciting feature of the techniques used in Chapter 5 is that the more and better side information available, the better the resulting ^{19}F images should become. To this end, and with the goal of *in vivo* ^{19}F imaging of atherosclerosis in mind, proton sequences should be developed which rapidly generate images with a variety of contrasts. For example, the gated 3D black-blood TSE sequence of Figure 5.11 should be further optimized to achieve better visualization of the myocardium and sufficient ventricular blood suppression through manipulation of the echo-train length, spatial resolution, and spoiler gradient amplitude. Additionally, a white-blood MRA sequence would be useful.

Another possibility is to develop and test an acquisition-weighted version of the pulse sequence that acquires more averages near the center of k-space to effectively incorporate a k-space apodization function in the acquisition. This idea has been used in a variety of applications where spatial resolution is limited [92].

Finally, the technical details of rapidly switching between acquiring data at the proton frequency and the ^{19}F frequency should be worked out. The small-animal scanner at UVa has Siemens electronics that are similar to whole-body scanners and all of our pulse sequences are compiled in-house, so it should be straightforward to learn how to switch between nuclei rapidly. The ^{19}F data will need to be acquired every 3 seconds or so, and the proton data can be acquired between ^{19}F readouts.

6.2.3 Exploration of advanced ^{19}F reconstruction methods

The best way to incorporate boundary information into constrained reconstructions of multi-nuclear data remains an open question. The interplay between constrained smoothing, de-noised reference images, the imposition of sparsity, and other possible techniques in the reconstruction is a complex problem. Other techniques that may be useful to incorporate side information into ^{19}F reconstructions include the use of edge detection algorithms, or – following Haldar et al. [93] – through shared line-site priors, which are explicitly used to model the edge structure in an image. Also, the quadratic penalty (Eq. 5.2) is a simple regularization method. More advanced regularization methods (total variation, hyperbolic, etc.) are available that do a better job in preserving edges [87]. Finally, improving resolution and SNR through explicit incorporation of superresolution methods is an interesting avenue for further research, as recent studies have shown that the SNR in high-resolution images reconstructed via superresolution can surpasses the SNR of high-resolution images acquired directly [94].

Bibliography

[1] Ross R. The pathogenesis of atherosclerosis: a perspective for the 1990s. *Nature*, 362 (6423):801–809, Apr 1993. 2

[2] Lusis AJ. Atherosclerosis. *Nature*, 407(6801):233–241, Sep 2000. 2

[3] Libby P, Ridker PM, Hansson GK, and Leducq Transatlantic Network on Atherothrombosis. Inflammation in atherosclerosis: from pathophysiology to practice. *J Am Coll Cardiol*, 54(23):2129–2138, Dec 2009. 2, 5, 6

[4] Libby P, Ridker PM, and Hansson GK. Progress and challenges in translating the biology of atherosclerosis. *Nature*, 473(7347):317–325, May 2011. 2, 6

[5] Bushberg JT, Seibert JA, Leidholdt EM Jr, and Boone JM. *Lippincott Williams and Wilkins*. Elsevier Academic Press, 2001. 3

[6] Creager MA, White CJ, Hiatt WR, Criqui MH, Josephs SC, Alberts MJ, Pearce WH, Gray BH, Rocha-Singh KJ, and American Heart Association. Atherosclerotic Peripheral Vascular Disease Symposium II: executive summary. *Circulation*, 118(25):2811–2825, Dec 2008. 3

[7] Al-Qaisi M, Nott DM, King DH, Kaddoura S, and Hamady M. Imaging of peripheral vascular disease. *Rep Med Imaging*, 2(1):25–34, Mar 2009. 3

[8] Lakshminarayan R, Simpson JO, and Ettles DF. Magnetic resonance angiography: current status in the planning and follow-up of endovascular treatment in lower-limb arterial disease. *Cardiovasc Intervent Radiol*, 32(3):397–405, May 2009. 3

[9] Hadizadeh DR, Gieseke J, Lohmaier SH, Wilhelm K, Boschewitz J, Verrel F, Schild HH, and Willinek WA. Peripheral MR angiography with blood pool contrast agent: prospective intraindividual comparative study of high-spatial-resolution steady-state MR angiography versus standard-resolution first-pass MR angiography and DSA. *Radiology*, 249(2):701–711, Nov 2008. 3

[10] Thomsen HS. Nephrogenic systemic fibrosis: A serious late adverse reaction to gadodiamide. *Eur Radiol*, 16(12):2619–2621, Dec 2006. 3

[11] Weinreb JC and Abu-Alfa AK. Gadolinium-based contrast agents and nephrogenic systemic fibrosis: why did it happen and what have we learned? *J Magn Reson Imaging*, 30(6):1236–1239, Dec 2009. 3

[12] Steinberg FL, Yucel EK, Dumoulin CL, and Souza SP. Peripheral vascular and abdominal applications of MR flow imaging techniques. *Magn Reson Med*, 14(2):315–320, May 1990. 4, 11

[13] Reimer P and Boos M. Phase-contrast MR angiography of peripheral arteries: technique and clinical application. *Eur Radiol*, 9(1):122–127, 1999. 4, 11

[14] Miyazaki M, Sugiura S, Tateishi F, Wada H, Kassai Y, and Abe H. Non-contrast-enhanced MR angiography using 3D ECG-synchronized half-Fourier fast spin echo. *J Magn Reson Imaging*, 12(5):776–783, Nov 2000. 4, 11

[15] Fan Z, Sheehan J, Bi X, Liu X, Carr J, and Li D. 3D noncontrast MR angiography of the distal lower extremities using flow-sensitive dephasing (FSD)-prepared balanced SSFP. *Magn Reson Med*, 62(6):1523–1532, Dec 2009. 4, 11

[16] Wright GA, Nishimura DG, and Macovski A. Flow-independent magnetic resonance projection angiography. *Magn Reson Med*, 17(1):126–140, Jan 1991. 4, 12

[17] Brittain JH, Olcott EW, Szuba A, Gold GE, Wright GA, Irarrazaval P, and Nishimura DG. Three-dimensional flow-independent peripheral angiography. *Magn Reson Med*, 38 (3):343–354, Sep 1997. 4

[18] Brittain JH, Hu BS, Wright GA, Meyer CH, Macovski A, and Nishimura DG. Coronary angiography with magnetization-prepared T2 contrast. *Magn Reson Med*, 33(5):689–696, May 1995. 4, 37

[19] Cukur T, Lee JH, Bangerter NK, Hargreaves BA, and Nishimura DG. Non-contrast-enhanced flow-independent peripheral MR angiography with balanced SSFP. *Magn Reson Med*, 61(6):1533–1539, Jun 2009. 4, 34, 37

[20] Cukur T, Shimakawa A, Yu H, Hargreaves BA, Hu BS, Nishimura DG, and Brittain JH. Magnetization-prepared IDEAL bSSFP: a flow-independent technique for noncontrast-enhanced peripheral angiography. *J Magn Reson Imaging*, 33(4):931–939, Apr 2011. 4, 12, 26

[21] Wright GA, Hu BS, and Macovski A. 1991 I.I. Rabi Award. Estimating oxygen saturation of blood in vivo with MR imaging at 1.5 T. *J Magn Reson Imaging*, 1(3):275–283, May-Jun 1991. 4, 12, 16, 26, 38

[22] Bernstein MA, King KF, and Zhou XJ. *Handbook of MRI Pulse Sequences*. Elsevier Academic Press, 2004. 4, 14, 61

[23] Haacke EM, Brown RW, Thompson MR, and Venkatesan R. *Magnetic Resonance Imaging: Physical Principles and Sequence Design*. Wiley-Liss, 1999. 5

[24] Ahn CB, Kim JH, and Cho ZH. High-speed spiral-scan echo planar NMR imaging-I. *IEEE Trans Med Imaging*, 5(1):2–7, 1986. 5

[25] Meyer CH, Hu BS, Nishimura DG, and Macovski A. Fast spiral coronary artery imaging. *Magn Reson Med*, 28(2):202–213, Dec 1992. 5, 37

[26] Grivennikov SI, Greten FR, and Karin M. Immunity, inflammation, and cancer. *Cell*, 140(6):883–899, Mar 2010. 5

[27] Wellen KE and Hotamisligil GS. Inflammation, stress, and diabetes. *J Clin Invest*, 115 (5):1111–1119, May 2005. 5

[28] Abraham C and Cho JH. Inflammatory bowel disease. *N Engl J Med*, 361(21):2066–2078, Nov 2009. 5

[29] Majithia V and Geraci SA. Rheumatoid arthritis: diagnosis and management. *Am J Med*, 120(11):936–939, Nov 2007. 5

[30] Cooper LT. Myocarditis. *N Engl J Med*, 360(15):1526–1538, Apr 2009. 5

[31] Rogers IS and Tawakol A. Imaging of coronary inflammation with FDG-PET: feasibility and clinical hurdles. *Curr Cardiol Rep*, 13(2):138–144, Apr 2011. 6

[32] Abdel-Aty H, Simonetti O, and Friedrich MG. T2-weighted cardiovascular magnetic resonance imaging. *J Magn Reson Imaging*, 26(3):452–459, Sep 2007. 6

[33] Rudd JH and Fayad ZA. Imaging atherosclerotic plaque inflammation. *Nat Clin Pract Cardiovasc Med*, 5 Suppl 2:11–17, Aug 2008. 6

[34] Strijkers GJ, Mulder WJ, van Tilborg GA, and Nicolay K. MRI contrast agents: current status and future perspectives. *Anticancer Agents Med Chem*, 7(3):291–305, May 2007. 6

[35] Ruiz-Cabello J, Barnett BP, Bottomley PA, and Bulte JW. Fluorine (19F) MRS and MRI in biomedicine. *NMR Biomed*, 24(2):114–129, Feb 2011. 7, 8

[36] Holland G, Bottomley P, and Hinshaw W. 19F magnetic resonance imaging. *J Magn Reson*, 28(1):133–136, Oct 1977. 7

[37] Clark LC, Ackerman JL, Thomas SR, Millard RW, Hoffman RE, Pratt RG, Ragle-Cole H, Kinsey RA, and Janakiraman R. Perfluorinated organic liquids and emulsions as biocompatible NMR imaging agents for 19F and dissolved oxygen. *Adv Exp Med Biol*, 180:835–845, 1984. 7

[38] Mason RP, Antich PP, Babcock EE, Gerberich JL, and Nunnally RL. Perfluorocarbon imaging in vivo: a 19F MRI study in tumor-bearing mice. *Magn Reson Imaging*, 7(5):475–485, Sep-Oct 1989. 7

[39] Ahrens ET, Flores R, Xu H, and Morel PA. In vivo imaging platform for tracking immunotherapeutic cells. *Nat Biotechnol*, 23(8):983–987, Aug 2005. 7, 88

[40] Weise G, Basse-Lüsebrink TC, Kleinschnitz C, Kampf T, Jakob PM, and Stoll G. In vivo imaging of stepwise vessel occlusion in cerebral photothrombosis of mice by 19F MRI. *PLoS One*, 6(12), 2011. 7

[41] Fan X, River JN, Muresan AS, Popescu C, Zamora M, Culp RM, and Karczmar GS. MRI of perfluorocarbon emulsion kinetics in rodent mammary tumours. *Phys Med Biol*, 51(2):211–220, Jan 2006. 7

[42] Southworth R, Kaneda M, Chen J, Zhang L, Zhang H, Yang X, Razavi R, Lanza G, and Wickline SA. Renal vascular inflammation induced by Western diet in ApoE-null mice quantified by (19)F NMR of VCAM-1 targeted nanobeacons. *Nanomedicine*, 5(3): 359–367, Sep 2009. 7

[43] Weise G, Basse-Luesebrink TC, Wessig C, Jakob PM, and Stoll G. In vivo imaging of inflammation in the peripheral nervous system by (19)F MRI. *Exp Neurol*, 229(2): 494–501, Jun 2011.

[44] Flögel U, Ding Z, Hardung H, Jander S, Reichmann G, Jacoby C, Schubert R, and Schrader J. In vivo monitoring of inflammation after cardiac and cerebral ischemia by fluorine magnetic resonance imaging. *Circulation*, 118(2):140–148, Jul 2008. 92, 100

[45] Ebner B, Behm P, Jacoby C, Burghoff S, French BA, Schrader J, and Flögel U. Early assessment of pulmonary inflammation by 19F MRI in vivo. *Circ Cardiovasc Imaging*, 3(2):202–210, Mar 2010.

[46] Hertlein T, Sturm V, Kircher S, Basse-Lüsebrink T, Haddad D, Ohlsen K, and Jakob P. Visualization of abscess formation in a murine thigh infection model of Staphylococcus aureus by 19F-magnetic resonance imaging (MRI). *PLoS One*, 6(3), 2011.

[47] Temme S, Bönner F, Schrader J, and Flögel U. 19F magnetic resonance imaging of endogenous macrophages in inflammation. *Wiley Interdiscip Rev Nanomed Nanobiotechnol*, 4(3):329–343, May-Jun 2012. 7, 88

[48] Riess JG and Krafft MP. Fluorocarbon Emulsions as *in vivo* Oxygen Delivery Systems: Background and Chemistry. In Robert M. Winslow M, editor, *Blood Substitutes*, pages 259–275. Elsevier Inc, 2006. 7

[49] Giraudeau C, Flament J, Marty B, Boumezbeur F, Mériaux S, Robic C, Port M, Tsapis N, Fattal E, Giacomini E, Lethimonnier F, Le Bihan D, and Valette J. A new paradigm for high-sensitivity 19F magnetic resonance imaging of perfluorooctylbromide. *Magn Reson Med*, 63(4):1119–1124, Apr 2010. 8, 89

[50] Haldar JP, Hernando D, Song SK, and Liang ZP. Anatomically constrained reconstruction from noisy data. *Magn Reson Med*, 59(4):810–818, Apr 2008. 9, 90, 97

[51] Dewaraja YK, Koral KF, and Fessler JA. Regularized reconstruction in quantitative SPECT using CT side information from hybrid imaging. *Phys Med Biol*, 55(9):2523–2539, May 2010. 9, 90, 97, 101

[52] Edelman RR, Sheehan JJ, Dunkle E, Schindler N, Carr J, and Koktzoglou I. Quiescent-interval single-shot unenhanced magnetic resonance angiography of peripheral vascular disease: Technical considerations and clinical feasibility. *Magn Reson Med*, 63(4):951–958, Apr 2010. 11

[53] McCormack EJ, Egnor MR, and Wagshul ME. Improved cerebrospinal fluid flow measurements using phase contrast balanced steady-state free precession. *Magn Reson Imaging*, 25(2):172–182, Feb 2007. 12

[54] Aletras AH, Kellman P, Derbyshire JA, and Arai AE. ACUT2E TSE-SSFP: a hybrid method for T2-weighted imaging of edema in the heart. *Magn Reson Med*, 59(2):229–235, Feb 2008. 12

[55] Hinks RS and Constable RT. Gradient moment nulling in fast spin echo. *Magn Reson Med*, 32(6):698–706, Dec 1994. 13

[56] Luz Z and Meiboom S. Nuclear Magnetic Resonance Study of the Protolysis of Trimethylammonium Ion in Aqueous Solution-Order of the Reaction with Respect to Solvent. *J Chem Phys*, 39(2):366–370, 1963. ISSN 00219606. 26, 38

[57] Henkelman RM, Hardy PA, Bishop JE, Poon CS, and Plewes DB. Why fat is bright in RARE and fast spin-echo imaging. *J Magn Reson Imaging*, 2(5):533–540, Sep-Oct 1992. 27

[58] Hargreaves BA, Vasanawala SS, Nayak KS, Hu BS, and Nishimura DG. Fat-suppressed steady-state free precession imaging using phase detection. *Magn Reson Med*, 50(1):210–213, Jul 2003. 28, 31

[59] Fielden SW, Mugler III JP, Hagspiel KD, Kramer CM, and Meyer CH. Refocused Turbo Spin Echo for Noncontrast MRA. In *Proc Intl Soc Mag Reson Med*, page 1877, Honolulu, HI, 2009. 36, 37

[60] Fielden SW, Mugler III JP, Norton PT, Hagspiel KD, Kramer CM, and Meyer CH. Feasibility of Refocused Turbo Spin Echo (rTSE) for Clinical Noncontrast MRA. In *Proc Intl Soc Mag Reson Med*, volume 18, page 1427, Stockholm, Sweden, 2010. 37

[61] Chen W and Meyer CH. Off-Resonance Correction for 3D Imaging Using a Stack of Spirals Trajectory. In *Proc Intl Soc Mag Reson Med*, page 2966, Seattle, WA, 2006. 42

[62] Chen W, Sica CT, and Meyer CH. Fast conjugate phase image reconstruction based on a Chebyshev approximation to correct for B0 field inhomogeneity and concomitant gradients. *Magn Reson Med*, 60(5):1104–1111, Nov 2008. 44, 62

[63] Tang Y, Yamashita Y, and Takahashi M. Ultrafast T2-weighted imaging of the abdomen and pelvis: use of single shot fast spin-echo imaging. *J Magn Reson Imaging*, 8(2):384–390, Mar-Apr 1998. 44

[64] McGibney G, Smith MR, Nichols ST, and Crawley A. Quantitative evaluation of several partial Fourier reconstruction algorithms used in MRI. *Magn Reson Med*, 30(1):51–59, Jul 1993. 45

[65] Tsai CM and Nishimura DG. Reduced aliasing artifacts using variable-density k-space sampling trajectories. *Magn Reson Med*, 43(3):452–458, Mar 2000. 47

[66] Lustig M and Pauly JM. SPIRiT: Iterative self-consistent parallel imaging reconstruction from arbitrary k-space. *Magn Reson Med*, 64(2):457–471, Aug 2010. 48

[67] Börnert P, Aldefeld B, and Eggers H. Reversed spiral MR imaging. *Magn Reson Med*, 44(3):479–484, Sep 2000. 61

[68] Meyer CH. *Rapid Magnetic Resonance Imaging*. PhD thesis, Stanford University, 2000. 61

[69] Glover GH. Spiral imaging in fMRI. *Neuroimage*, 62(2):706–712, Aug 2012. 61

[70] Delattre BM, Heidemann RM, Crowe LA, Vallée JP, and Hyacinthe JN. Spiral demystified. *Magn Reson Imaging*, 28(6):862–881, Jul 2010. 61

[71] Irarrazabal P, Meyer CH, Nishimura DG, and Macovski A. Inhomogeneity correction using an estimated linear field map. *Magn Reson Med*, 35(2):278–282, Feb 1996. 62

[72] Noll DC, Meyer CH, Pauly JM, Nishimura DG, and Macovski A. A homogeneity correction method for magnetic resonance imaging with time-varying gradients. *IEEE Trans Med Imaging*, 10(4):629–637, 1991. 62

[73] Man LC, Pauly JM, and Macovski A. Multifrequency interpolation for fast off-resonance correction. *Magn Reson Med*, 37(5):785–792, May 1997. 62

[74] Noll DC, Pauly JM, Meyer CH, Nishimura DG, and Macovski A. Deblurring for non-2D Fourier transform magnetic resonance imaging. *Magn Reson Med*, 25(2):319–333, Jun 1992. 62

[75] Man LC, Pauly JM, and Macovski A. Improved automatic off-resonance correction without a field map in spiral imaging. *Magn Reson Med*, 37(6):906–913, Jun 1997. 62

[76] King KF, Ganin A, Zhou XJ, and Bernstein MA. Concomitant gradient field effects in spiral scans. *Magn Reson Med*, 41(1):103–112, Jan 1999. 62, 68

[77] Chen W and Meyer CH. Semiautomatic off-resonance correction in spiral imaging. *Magn Reson Med*, 59(5):1212–1219, May 2008.

[78] Sica CT. *Concomitant gradient field effects in spiral scanning and balanced SSFP scanning*. PhD thesis, University of Virginia, 2008. 62, 69

[79] Fielden SW, Meyer CH, and Mugler III JP. Variable-flip-angle 3D turbo spin echo imaging utilizing spiral acquisitions. In *Proc Intl Soc Mag Reson Med*, volume 19, page 2820, Montreal, Canada, 2011. 76

[80] Glover GH and Law CS. Spiral-in/out BOLD fMRI for increased SNR and reduced susceptibility artifacts. *Magn Reson Med*, 46(3):515–522, Sep 2001. 84

[81] Preston AR, Thomason ME, Ochsner KN, Cooper JC, and Glover GH. Comparison of spiral-in/out and spiral-out BOLD fMRI at 1.5 and 3 T. *Neuroimage*, 21(1):291–301, Jan 2004. 84

[82] Glover GH and Thomason ME. Improved combination of spiral-in/out images for BOLD fMRI. *Magn Reson Med*, 51(4):863–868, Apr 2004. 84

[83] Fessler J, Clinthorne N, and Rogers W. Regularized emission image reconstruction using imperfect side information. *IEEE Trans Nuc Sci*, 39(5):1464 –1471, Oct 1992. 90

[84] Comtat C, Kinahan PE, Fessler JA, Beyer T, Townsend DW, Defrise M, and Michel C. Clinically feasible reconstruction of 3D whole-body PET/CT data using blurred anatomical labels. *Phys Med Biol*, 47(1):1–20, Jan 2002.

[85] Nuyts J, Baete K, Bequé D, and Dupont P. Comparison between MAP and postprocessed ML for image reconstruction in emission tomography when anatomical knowledge is available. *IEEE Trans Med Imaging*, 24(5):667–675, May 2005. 90

[86] Rousseau F. A non-local approach for image super-resolution using intermodality priors. *Med Image Anal*, 14(4):594–605, Aug 2010. 90, 110

[87] Fessler JA. MODEL-BASED IMAGE RECONSTRUCTION FOR MRI. *IEEE Signal Process Mag*, 27(4):81–89, Jul 2010. 110, 128

[88] Buades A, Coll B, and Morel J. A Review of Image Denoising Algorithms, with a New One. *Multiscale Modeling & Simulation*, 4(2):490–530, 2005. 111

[89] Lustig M, Donoho D, and Pauly JM. Sparse MRI: The application of compressed sensing for rapid MR imaging. *Magn Reson Med*, 58(6):1182–1195, Dec 2007. 113, 114, 115

[90] van Heeswijk RB, Pellegrin M, Mazzolai L, Flogel U, Schwitter J, and Stuber M. Fluorine-19 magnetic resonance imaging in a mouse model of atherosclerosis. In *Proc Intl Soc Mag Reson Med*, volume 20, page 3945, 2012. 120

[91] Park J, Mugler JP, Horger W, and Kiefer B. Optimized T1-weighted contrast for single-slab 3D turbo spin-echo imaging with long echo trains: application to whole-brain imaging. *Magn Reson Med*, 58(5):982–992, Nov 2007. 125

[92] Adalsteinsson E, Star-Lack J, Meyer CH, and Spielman DM. Reduced spatial side lobes in chemical-shift imaging. *Magn Reson Med*, 42(2):314–323, Aug 1999. 127

[93] Haldar JP, Wedeen VJ, Nezamzadeh M, Dai G, Weiner MW, Schuff N, and Liang ZP. Improved diffusion imaging through SNR-enhancing joint reconstruction. *Magn Reson Med*, Mar 2012. [Epub ahead of print]. 128

[94] Van Reeth E, Tham IWK, Tan CH, and Poh CL. Super-resolution in magnetic resonance imaging: A review. *Concepts in Magnetic Resonance Part A*, 40A(6):306–325, 2012. ISSN 1552-5023. 128